



DESIGN OF A FILM COOLING EXPERIMENT FOR ROCKET ENGINES

THESIS

Andrew L. Sincock, Major, USAF

AFIT/GAE/ENY/10-M23

**DEPARTMENT OF THE AIR FORCE
AIR UNIVERSITY**

AIR FORCE INSTITUTE OF TECHNOLOGY

Wright-Patterson Air Force Base, Ohio

APPROVED FOR PUBLIC RELEASE; DISTRIBUTION UNLIMITED

The views expressed in this thesis are those of the author and do not reflect the official policy or position of the United States Air Force, Department of Defense, or the U.S. Government. This material is declared a work of the U.S. Government and is not subject to copyright protection in the United States.

AFIT/GAE/ENY/10-M23

DESIGN OF A FILM COOLING EXPERIMENT FOR ROCKET ENGINES

THESIS

Presented to the Faculty

Department of Aeronautics and Astronautics

Graduate School of Engineering and Management

Air Force Institute of Technology

Air University

Air Education and Training Command

In Partial Fulfillment of the Requirements for the
Degree of Master of Science in Aeronautical Engineering

Andrew L. Sincock, B.S.

Major, USAF

March 2010

APPROVED FOR PUBLIC RELEASE; DISTRIBUTION UNLIMITED

AFIT/GAE/ENY/10-M23

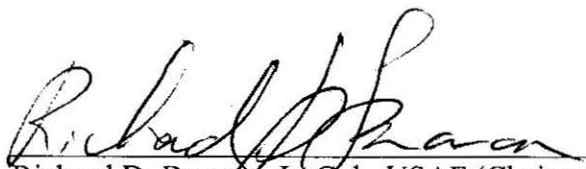
DESIGN OF A FILM COOLING EXPERIMENT FOR ROCKET ENGINES

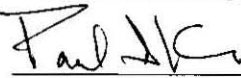
Andrew L. Sincock, B.S.

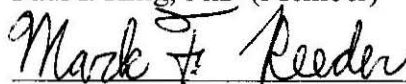
Major, USAF

March 2010

Approved:


Richard D. Branan, Lt Col., USAF (Chairman)


Paul I. King, PhD (Member)


Mark Reeder, PhD (Member)

17 Mar 10
Date

17 Mar 10
Date

17 Mar 10
Date

Abstract

The Film Cooling Rig (FCR) is a new test rig at the Air Force Institute of Technology (AFIT) to study film cooling for rocket engine applications. The original researcher designed, built, and then utilized the FCR to study radial curvature effects on film cooling for a non-combustion environment. This effort modified the FCR by adding propane-air combustion. Modular stainless steel test sections were produced to allow study of various curvatures and coolant injection angles. A pre-mixed burner was designed and built to deliver main flow mass flow rates necessary to produce blowing ratios as low as 0.5. A water cooling system was designed for the entire FCR, but only implemented for the curved test sections. Instrumentation in this system allows calculation of the average heat flux to the test section. Once the necessary FCR and lab modifications were accomplished, the operating range of the FCR was developed and tested using infrared thermography. Surface temperature measurements near the cooling hole showed no cooling effect for 13 major test configurations, and many more minor variations. The lack of cooling was caused by inadequate spreading of the burner flow to the test section wall. Without the necessary main flow momentum across the test section wall, the coolant flow did not turn and adhere to the wall. Instead, it jetted into the main flow without cooling the wall as expected. Recommendations included modifications to the existing rig to correct the main flow issue, along with a completely new FCR design incorporating the lessons learned from this research to produce a simpler, more effective rig. The new design allows the laser and infrared diagnostics of the first rig without the manufacturing complications that hindered testing in the first FCR.

Acknowledgments

First, I must thank my wife for her loving support through this entire process. There is no way to quantify her contribution, but this thesis reflects far more of her hard work than it does mine. I love you! My kids were so excited not to have me TDY every week, only to find out that weekends here just meant I did not wear a uniform to school. I am so blessed to have 3 beautiful daughters and I can't wait for the bike rides and beach trips that await us in California.

Aaron Drenth took time from writing his thesis to show me the ropes in the COAL lab; this not only made my life easier, but his documentation should be the standard for passing down lab procedures and practices. Future students are lucky to have his work to lean on. Mike Miller turned my thoughts into MATLAB® along with various tasks I was hesitant to perform, all while finishing his undergrad and finding a job. Thank you both.

Finally, I cannot say enough about my advisor, Lt Col Richard Branam. I can count on one hand the professors I have encountered with the passion for their subject that Lt Col Branam has. His enthusiasm challenged me and kept me going, even when things were not working out. I was fortunate to work with him.

Andrew L. Sincock

Table of Contents

| | Page |
|--|------|
| Abstract | iv |
| Acknowledgments..... | v |
| Table of Contents | vi |
| List of Figures | viii |
| List of Tables | xii |
| List of Symbols | xiii |
| List of Abbreviations | xvii |
| I. Introduction | 1 |
| 1.1 Motivation | 1 |
| 1.2 Film Cooling..... | 3 |
| 1.3 AFIT Film Cooling Rig | 4 |
| 1.4 Research Purpose..... | 5 |
| II. Literature Review | 7 |
| 2.1 Rocket Engines | 7 |
| 2.2 Effusion Cooling Basics | 8 |
| 2.3 History of Effusion Cooling Research for Rockets | 12 |
| 2.4 AFIT Test Capability..... | 24 |
| III. Methodology | 29 |
| 3.1 Research Objectives | 29 |
| 3.2 Laboratory Setup | 30 |
| 3.3 Film Cooling Rig Modification | 40 |
| IV. Analysis and Results..... | 79 |
| 4.1 Test Section Construction..... | 79 |
| 4.2 Final Burner Design | 83 |

| | Page |
|--|------|
| 4.3 Heat Flux Experiment Design | 89 |
| 4.4 Infrared and Heat Flux Test Results..... | 97 |
| V. Conclusions and Recommendations | 107 |
| 5.1 Conclusions of Research | 107 |
| 5.2 Recommendations | 109 |
| 5.3 Future Research | 114 |
| Appendix A. MKS Type 247 Mass Flow Controller Control Panel Settings | 118 |
| Appendix B. LabVIEW® Procedures..... | 119 |
| Appendix C. IR Camera Operation..... | 122 |
| Appendix D. MATLAB® Code | 126 |
| Bibliography | 131 |
| Vita | 134 |

List of Figures

| | Page |
|--|------|
| Figure 1: Two types of effusion cooling (2) | 3 |
| Figure 2: AFIT film coolant rig | 4 |
| Figure 3: Chen’s experimental transpiration cooling efficiency (8) | 18 |
| Figure 4: Adiabatic effectiveness for a flat plate (left) and curved plate (D_{∞}/D_j , right) ($F = 0.5$)(2)..... | 20 |
| Figure 5: Film cooling injection angles | 22 |
| Figure 6: OH concentrations inside the UCC (22)..... | 25 |
| Figure 7: PIV data in the UCC (23) | 26 |
| Figure 8: Infrared thermography signal sources (17) | 27 |
| Figure 9: Infrared picture of a Hall thruster (17) | 28 |
| Figure 10: K bottles (left), propane tanks (right), and propane vaporization system (upper right) inside the tank farm | 31 |
| Figure 11: FCR gas flow diagram..... | 32 |
| Figure 12: Test stand setup | 32 |
| Figure 13: Control panels for MFCs..... | 33 |
| Figure 14: HVOF control panel | 34 |
| Figure 15: Air supply tanks..... | 35 |
| Figure 16: Flow meter and valve for air supply..... | 36 |
| Figure 17: COAL lab master control station..... | 37 |
| Figure 18: Original COAL lab LabVIEW® VI..... | 38 |
| Figure 19: New FCR LabVIEW® VI..... | 39 |

| | Page |
|--|------|
| Figure 20: Test section CAD drawing | 41 |
| Figure 21: 90° compound injection test section cross-section (flow out of page)..... | 41 |
| Figure 22: Exploded view of a test section | 42 |
| Figure 23: Machined lip on test section | 43 |
| Figure 24: McCall's cooling plenum (2) | 45 |
| Figure 25: Coolant tube outer seal, braze on left, RTV on right | 47 |
| Figure 26: Original burner design..... | 50 |
| Figure 27: 3/8" Burner lifted flame | 51 |
| Figure 28: 2" burner and 3/8" burner | 53 |
| Figure 29: 2" coaxial burner flame | 54 |
| Figure 30: 2" Burner, increasing ϕ (left to right) | 56 |
| Figure 31: Burner insert | 57 |
| Figure 32: Final burner configuration..... | 58 |
| Figure 33: Old (left) and new (right) inlet wall | 59 |
| Figure 34: Water cooling overview | 61 |
| Figure 35: Inlet manifold | 62 |
| Figure 36: Outlet manifold..... | 63 |
| Figure 37: Inner wall with RTV applied (not yet sealed) | 64 |
| Figure 38: UCC/FCR igniter..... | 65 |
| Figure 39: Ethylene/air igniter operation | 66 |
| Figure 40: Quartz and zinc selenide (ZnSe) windows | 67 |

| | Page |
|--|------|
| Figure 41: Unsteady operation..... | 70 |
| Figure 42: McCall’s infrared test setup (2)..... | 72 |
| Figure 43: Horizontal test setup..... | 72 |
| Figure 44: ZnSe window transmissivity (17)..... | 73 |
| Figure 45: FLIR systems SC640..... | 75 |
| Figure 46: Final test section configuration | 79 |
| Figure 47: Thermocouple error (@20-50 °C). The baseline is where the measured temperature equals the actual temperature | 81 |
| Figure 48: Thermocouple extending from test section | 82 |
| Figure 49: Burner flame in open air, ϕ increasing left (0.9) to right(1.5)..... | 84 |
| Figure 50: Diffusion flame at FCR exit | 84 |
| Figure 51: Burner flame at $\phi = 0.90$ | 85 |
| Figure 52: BIOS definier 220 used for MFC calibration | 86 |
| Figure 53: Air flow overshoot and settling when changing flow rate | 87 |
| Figure 54: Air flow oscillation at 0.4067 kg/min setting..... | 88 |
| Figure 55: Air flow during test window | 88 |
| Figure 56: CAD drawing of walls for water cooling | 91 |
| Figure 57: Inner (right) and outer (left) view of red-hot exit panel | 91 |
| Figure 58: Solid (top) and hollow (bottom) small side walls for the 4’’ test section | 93 |
| Figure 59: Solid exit wall nozzle | 93 |
| Figure 60: New inlet (left) and outlet (right) water-cooling manifolds | 94 |

| | Page |
|---|------|
| Figure 61: Water temperature change for complete test | 95 |
| Figure 62: Water temperature change during IR data collection | 96 |
| Figure 63: Water flow rate during data collection | 97 |
| Figure 64: Infrared picture of cooling hole (BR = 1.5). Main flow from right to left. | 98 |
| Figure 65: 0° injection, BR = 1.5 (temperature in Kelvin). Main flow from right to left. | 99 |
| Figure 66: 0° injection, BR = 0.5 (temperature in Kelvin). Main flow from right to left. | 100 |
| Figure 67: Propane flame from coolant line | 101 |
| Figure 68: Coolant flow combustion inside the FCR (exit wall removed) | 102 |
| Figure 69: Open exit wall | 103 |
| Figure 70: 90° injection, BR 1.5, open end (temperature in Kelvin) | 104 |
| Figure 71: Wall temperature variation for a single pixel, with and without combustion | 105 |
| Figure 72: New FCR concept | 115 |
| Figure 73: End view of new FCR burner | 115 |
| Figure 74: New test section concept | 116 |
| Figure 75: New nozzle concept | 117 |
| Figure 76: LabVIEW® VI for FCR | 119 |
| Figure 77: ThermaCam Researcher interface | 122 |

List of Tables

| | Page |
|--|------|
| Table 1: Solid vs. liquid fuel advantages | 7 |
| Table 2: McCall's Experimental Coefficients (2)..... | 23 |
| Table 3: Gas system summary | 33 |
| Table 4: FCR starting conditions | 69 |
| Table 5: P640 camera properties (23)w | 75 |
| Table 6: MFC control panel settings..... | 118 |
| Table 7: ThermoCam Researcher settings | 123 |
| Table 8: Data collection settings..... | 124 |

List of Symbols

English Letter Symbols

| | |
|-----------|--|
| a | number of moles of oxidizer |
| A | area |
| A/F | air to fuel ratio |
| B | driving force (convective heat transfer) |
| c_p | specific heat (constant pressure) |
| c^* | characteristic velocity |
| D | diameter |
| DR | density ratio |
| F | thrust, blowing ratio |
| f_s | mixture fraction |
| g | surface conductance |
| g_0 | Earth gravitational constant |
| h | specific enthalpy, heat transfer coefficient |
| H | characteristic length |
| I | momentum ratio |
| I_{sp} | specific impulse |
| K | pressure gradient |
| l | length |
| \dot{m} | mass flow rate |
| M | Mach number |

| | |
|-------|---|
| p | pressure |
| Pr | Prandtl number |
| q | heat |
| Q | total heat |
| R | Rannie temperature ratio, specific gas constant |
| Re | Reynolds number |
| r | radius |
| r_c | radius of curvature |
| S | film cooling area ratio |
| SL | laminar flame speed |
| St | Stanton number |
| T | temperature |
| u | velocity |
| v | velocity |
| W | power |
| Y_F | mass fraction |

Greek Letter Symbols

| | |
|---------------|-------------------|
| ε | emissivity |
| ϕ | equivalence ratio |
| Δ | change |
| π | Pi |

| | |
|-------------|---|
| γ | ratio of specific heat (constant pressure), streamwise distance between rows of film cooling holes |
| ρ | density |
| η | efficiency |
| ς | lateral distance between film cooling holes |
| μ | viscosity |
| θ | coolant injection angle (into main flow) |
| α | compound coolant injection angle |
| τ | transmissivity |

Subscripts and Superscripts

| | |
|----------|----------------------------|
| 0 | initial, chamber, uncooled |
| ∞ | main flow, far field |
| ‘ ’ | per unit area |
| * | nozzle throat conditions |
| θ | momentum (Reynolds number) |
| a | atmosphere |
| area | area average |
| atm | atmospheric |
| aw | adiabatic wall |
| c | coolant flow |
| e | exit |
| f | film cooling |

| | |
|------|--------------------------------|
| H | height basis (Reynolds number) |
| j | coolant jet |
| mix | mixture |
| refl | reflected (IR energy) |
| s | surface |
| span | spanwise average |
| t | transpiration cooling |
| w | wall |

List of Abbreviations

| | |
|-------------------------------|--|
| 2-D | Two Dimensional |
| °C | degrees Celsius |
| °F | degrees Fahrenheit |
| °K | degrees Kelvin |
| AFIT | Air Force Institute of Technology |
| C ₂ H ₄ | Ethylene |
| C ₃ H ₈ | Propane |
| CAD | Computer Aided Design |
| CAI | California Analytical Instruments |
| CARS | Coherent Anti-Stokes Raman Spectroscopy |
| CFD | Computational Fluid Dynamics |
| COAL | Combustion Optimization and Analysis Laser |
| EDM | Electrical Discharge Machining |
| FCFC | Full Coverage Film Cooling |
| FCR | Film Cooling Rig |
| GC | Gas Chromatograph |
| g | gram |
| gph | Gallons Per Hour |
| H ₂ | Hydrogen gas |
| H ₂ O | Water |
| HVOF | High Velocity Oxy-Fuel |

| | |
|----------------|----------------------------------|
| Hz | Hertz |
| IR | Infrared |
| JPL | Jet Propulsion Laboratory |
| kg | kilogram |
| lb | pound |
| lbf | Pound-force |
| LII | Laser Induced Incandescence |
| m | meter |
| mA | milliamp |
| MPG | Miles Per Gallon |
| MSD | Mass Selective Detector |
| MFC | Mass Flow Controller |
| min | minute |
| mol | mole |
| N ₂ | Nitrogen gas |
| nm | nanometers |
| NPT | National Pipe Thread |
| O ₂ | Oxygen gas |
| OH | Hydroxyl radical |
| PIV | Particle Image Velocimetry |
| PLIF | Planar Laser Induced Florescence |
| RTV | Room Temperature Vulcanizing |

| | |
|-------|---|
| s | second |
| SLPM | Standard Liters Per Minute |
| sccm | Standard Cubic Centimeters |
| SSME | Space Shuttle Main Engines |
| TDLAS | Tunable Diode Laser Absorption Spectroscopy |
| UCC | Ultra Compact Combustor |
| μm | micrometers |
| VI | Virtual Instrument |
| Xe | Xenon |
| ZnSe | Zinc Selenide |

DESIGN OF A FILM COOLING EXPERIMENT FOR ROCKET ENGINES

I. Introduction

1.1 Motivation

The typical goal of a rocket is to launch a payload to a desired place in space (or on the earth) with a desired velocity. The payload is usually the impetus for the launch, yet it only represents a small fraction of the total launch vehicle mass. The largest fraction is the propellant (fuel and oxidizer) mass, often 85-95% of the stage mass (1). With so much mass devoted to propellant, a key indicator of rocket performance is then the efficiency in converting fuel into propelling force. This efficiency is known as the *specific impulse* (I_{sp}), but in order to define specific impulse we must first define thrust. *Thrust* (F) is the propulsive force of the rocket acting against inertia and gravity to accelerate the rocket. With more thrust, a rocket may lift larger payloads than a comparable rocket with less thrust. Equation 1 shows the thrust of a rocket containing two components: the first coming from the propellant ejection from the rocket and the second is the pressure force acting on the exit area of the nozzle:

$$F = \dot{m}v_e + (p_e - p_a)A_e \quad (1)$$

where \dot{m} is *exit mass flow rate*, p_e is *exit pressure*, p_a is *atmospheric pressure*, and A_e is *nozzle exit area*. The exit velocity reaches a maximum when the exit pressure equals the atmospheric pressure, a key factor in nozzle design. The thrust contribution from the second half of the thrust equation is usually much smaller than the first, so that $F \approx \dot{m}v_e$.

Specific impulse is the efficiency of the rocket engine and it is related to the thrust as shown in Equation 2:

$$I_{sp} = \frac{F}{\dot{m}g_0} \quad (2)$$

where g_0 is the *gravitational constant* (9.8 m/s²). I_{sp} is therefore an indicator of the thrust produced for a given propellant mass flow rate. From the thrust and I_{sp} relationships, the driving variable in improving the I_{sp} of a rocket is maximizing the exit velocity for a given mass flow. Maximizing the exit velocity highlights the reason for this research.

The exit velocity is found as shown in Equation 3:

$$v_e = \sqrt{\frac{2\gamma RT_0}{\gamma - 1} \left[1 - \left(\frac{p_e}{p_0} \right)^{\frac{\gamma - 1}{\gamma}} \right]} \quad (3)$$

where γ is the *ratio of specific heats*, R is the *specific gas constant*, T_0 is *chamber temperature*, and p_0 is *chamber pressure*. The exit velocity increases with an increase in the chamber temperature. The chamber temperature is a function of the propellant choice and is limited by the material properties of the chamber and nozzle.

Large rocket engines utilize active cooling mechanisms because they allow the rocket to use higher temperatures than the un-cooled chamber material would survive. The chamber pressure is a function of the turbopump capability, itself adding significant mass and complexity to the rocket engine. Effusion cooling may reduce the pressure loss when the fuel flows through regenerative cooling lines, reducing the turbopump size and mass. While a variety of cooling methods are available and in use, effusion cooling may have significant benefits over current cooling methods, allowing higher chamber pressures and temperatures.

1.2 Film Cooling

Film cooling is a subset of a greater category of cooling known as effusion cooling. In general, effusion cooling uses coolant fluid or gas seeped through a wall to cool the wall in the presence of a high temperature flow. Figure 1 shows two types of effusion cooling: film and transpiration. Film (or wall) cooling keeps the wall cool with a discrete set of large holes in some predetermined orientation. Transpiration cooling uses a porous material with much smaller holes, often varying in size and orientation.

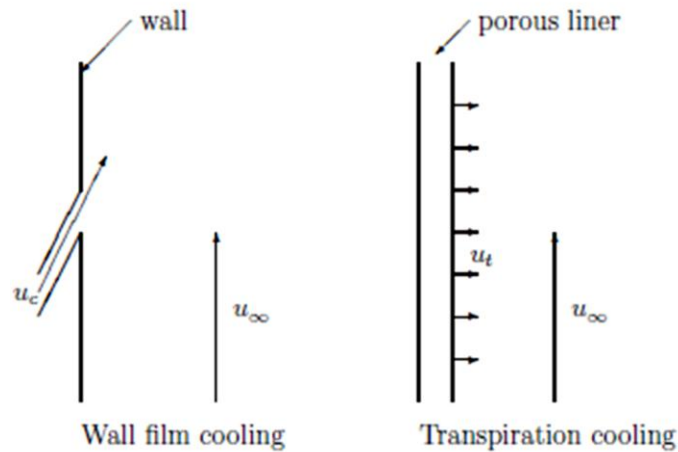


Figure 1: Two types of effusion cooling (2)

In either case, the coolant acts as a protective barrier, reducing the heat flux to the underlying material. The leading edges of aircraft turbine blades utilize film cooling, protecting the turbine from the high temperature combustion gasses exiting the combustion chamber. Despite research into transpiration cooling for rocket engines over 60 years ago, it is rarely used due to the difficulty in manufacturing something that is both porous and meets the original design intent. The increased cooling capability of transpiration cooling versus traditional cooling methods may allow engineers to increase

the chamber temperature, or they could keep the temperature constant, decreasing the cooling flow requirement. The decreased cooling flow requirement then decreases the pressure loss to cooling, allowing higher chamber pressures. In either case, the exit velocity increases producing more thrust and higher specific impulse (see Equation 3).

1.3 AFIT Film Cooling Rig

Captain Jonathan McCall (2) designed and built the AFIT Film Cooling Rig (FCR) to study radial curvature effects on film cooling. In a traditional turbine application, the cooling fluid encounters a concave or convex wall as it travels in the direction of flow. In a rocket engine, the fluid may encounter a concave wall in the nozzle, but it will also encounter the radial curvature of the chamber and nozzle. The FCR allows comparison of traditional film and transpiration cooling relationships due to radial curvature effects.

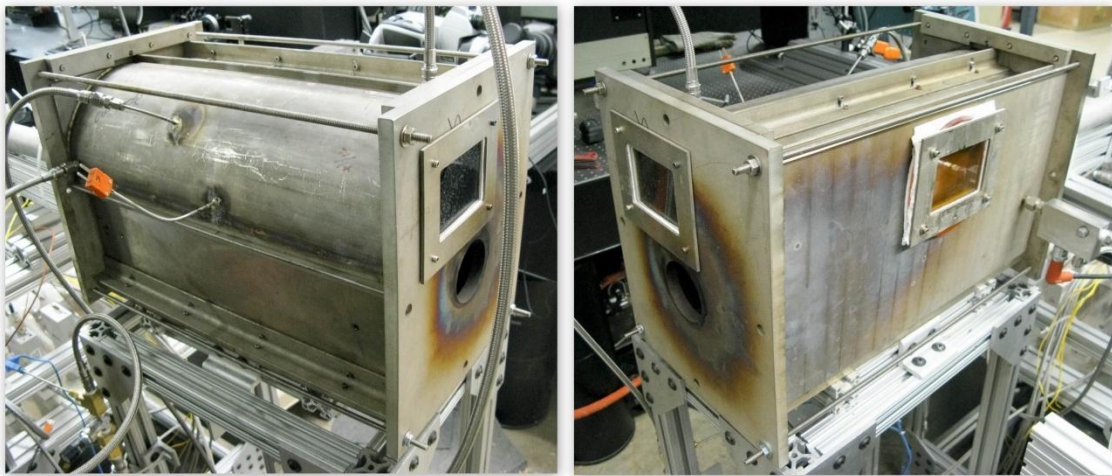


Figure 2: AFIT film coolant rig

Figure 2 shows the FCR after the modifications accomplished in this thesis. Test sections with varying curvature, hole size/orientation, or a number of other variables are easily tested due to the modular design of the FCR. Three view ports allow access for non-intrusive combustion diagnostic techniques. Stainless steel construction allows high temperatures and combustion environments. Finally, a water cooling system accommodates the high-temperature combustion environment and allows heat flux measurements.

1.4 Research Purpose

The purpose of this research is to modify the FCR and demonstrate its operation, to include film cooling of a radially curved wall. While the initial FCR design called for a combustion environment, previous research stopped well short of actual implementation. The modification tasks include design and build of the burner, ignition system, water-cooling system, and stainless steel test sections. In addition to the FCR changes, modification to the water delivery system, the fuel delivery system and the LabVIEW® computer program are also necessary.

Once modifications are complete, infrared thermography will capture the coolant effects on the wall yielding cooling efficiency statistics. The modified FCR will also allow laser diagnostic techniques to characterize the combustion environment and coolant flow in the film-cooled region.

Chapter 2 will describe the fundamentals of rocket engine performance and effusion cooling. It will also cover the research progress preceding this work. Chapter 3 details the experimental setup and modifications to the FCR while chapter 4 details the

experimental results. Finally, chapter 5 contains the conclusions, lessons learned, and suggestions for future research.

II. Literature Review

2.1 Rocket Engines

For a rocket to launch a payload into space, it must convert the latent energy stored inside its fuel into propulsive force (thrust). Chemical systems such as liquid, solid, and hybrid-fueled rockets use the energy present in the chemical bonds of the propellant to generate thrust. Alternatively, electrical propulsion systems use electrothermal, electromagnetic, or electrostatic thrust generation techniques (3). Modern space launch vehicles often use a combination of solid and liquid systems, while electric propulsion is limited to space applications due to the lower thrust levels. Any numbers of textbooks covering rocket propulsion document the benefits and drawbacks of solid versus liquid systems as summarized in Table 1 (3)(4).

Table 1: Solid vs. liquid fuel advantages

| Solid | Liquid |
|-------------|-------------|
| High thrust | High ISP |
| Simplicity | Throttling |
| Storable | Restartable |

The mission designer must evaluate each mission to determine what combination of solid and/or liquid fuel systems will meet their thrust and I_{sp} requirement.

Both solid and liquid fueled rockets require cooling for both the combustion chamber and nozzle regions due to the extremely high temperatures and pressures. The

main cooling options include regenerative, ablative, and film cooling (3). In addition, the heat may simply radiate to the surrounding environment. The presence of liquid fuel and oxidizers make regenerative and effusion cooling options for liquid systems; solids are limited to ablative and radiation cooling. Most large launch vehicles employ regenerative cooling where the liquid fuel flows through small tubing brazed to the nozzle. The liquid carries away the heat, not only cooling the wall, but also adding energy to the fuel. The drawback to this approach is that it complicates manufacture of the nozzle and significant pressure is lost through the small coolant tubes (2). The pressure loss in turn drives the pump size (mass) and available pressure to the combustion chamber.

2.2 Effusion Cooling Basics

Before addressing the literature on effusion cooling, it is useful to provide some background on the technique itself and the various parameters that define it. In any effusion cooling scheme, coolant flow is added to the main flow of the engine, not with the direct intent of adding to the work done by the engine, but rather to cool various components in the engine.

2.2.1 Effusion Cooling Flow

The main parameter in defining effusion cooling is the ratio of the coolant flow flux to main flow flux, also known as the *Blowing Ratio* (F).

$$F = \frac{\rho_c v_c}{\rho_\infty u_\infty} \quad (4)$$

where ρ_c is *coolant density*, v_c is *coolant velocity*, ρ_∞ is *main flow density*, v_∞ is *main flow velocity*. In turbine engines, the blowing ratio is important because it represents air bled

off the compressor stage and diverted past the combustor. While the coolant flow adds some energy to the cycle, there is a net loss when compared to the same inlet flow with no diverted coolant (5). For rocket engine applications, the blowing ratio may be even more important due to the need to carry the coolant onboard the vehicle itself, versus an aircraft capturing the coolant from the surrounding environment.

Another useful effusion cooling parameter is the momentum ratio (I), the ratio of the coolant flow to the main flow momentum:

$$I = \frac{\rho_c v_c^2}{\rho_\infty u_\infty^2} \quad (5)$$

The momentum ratio is important in defining how the kinetic energy of the main flow and the cooling flow interact. Physically this interaction is observed in how the coolant jet turns when injected off-axis from the main flow. The momentum ratio also affects the maximum coolant mass flux before the coolant stops coating the wall in a film-like manner and starts jetting into the main flow (2).

The density ratio (DR) is simply the ratio of the cooling flow density to the main flow:

$$DR = \frac{\rho_c}{\rho_\infty} \quad (6)$$

Research has considered the effects of the density ratio on film cooling, but mostly on a scale that applies to aircraft. In the typical rocket engine with cryogenic fuels injected into a hot chamber, the density ratio can be orders of magnitude greater than aircraft engine applications (2).

2.2.2 Transpiration Cooling Efficiency

Transpiration cooling is essentially just convective heat transfer from the main flow to the cool wall combined with a mass transfer from the cool wall into the main flow. The Stanton number (St) characterizes the convective heat transfer involved in transpiration cooling. McCall(2) characterized the Stanton number as the heat transfer perpendicular to a wall in a flow to the heat transfer parallel to the wall:

$$St = \frac{\dot{q}_{s-\infty}''}{\dot{m}_{\infty}'' c_{p,\infty} (\Delta T_{s-\infty})} \quad (7)$$

where St is the *Stanton number*, \dot{q}_s'' is *heat flux into surface*, $c_{p,\infty}$ is *specific heat* (at constant pressure), and \dot{m}_{∞}'' is *main flow mass flux*. Modifying Equation 7 is possible by recognizing the temperature difference factor in the surface heat flux.

$$St = \frac{h}{\dot{m}_{\infty}'' c_{p,\infty}} \quad (8)$$

where h is the *heat transfer coefficient*. Typical transpiration cooling analysis ignores radiation from the main flow to the wall because it is a small percentage of the total heat transfer.

The *cooling efficiency* (η_t) of transpiration cooling is the ratio of cooled Stanton number to uncooled Stanton number, or even more specifically, the ratio of the two heat transfer coefficients:

$$\eta_t = \frac{St}{St_0} = \frac{h}{h_0} \quad (9)$$

2.2.3 Film Cooling Efficiency

While the blowing ratio defines the flow of the coolant and main flow, it does not give any insight into cooling performance. The film cooling efficiency, or adiabatic effectiveness, quantifies the performance of film cooling. Adiabatic effectiveness is the ratio of the temperature reduction of an adiabatic wall due to film cooling to the temperature difference between the main flow and the coolant flow.

$$\eta_f = \frac{T_\infty - T_{aw}}{T_\infty - T_c} \quad (10)$$

where η_f is *film cooling efficiency* (adiabatic effectiveness), T_∞ is *main flow recovery temperature*, T_{aw} is *adiabatic wall temperature* (cooled), and T_c is *coolant temperature*.

When the wall is the same temperature as the main flow, the efficiency is zero.

Conversely, the efficiency is one when the wall is the same temperature as the coolant flow.

As coolant flows out of the coolant channels and onto the wall it will eventually evaporate or mix into the main flow. Averaging the adiabatic effectiveness perpendicular to the flow highlights this effect when plotted vs. streamwise distance from the coolant hole. Equation 11 shows this *spanwise* adiabatic effectiveness.

$$\eta_{span} = \frac{1}{\zeta_2 + \zeta_1} \int_{-\zeta_1}^{\zeta_2} \eta_f dx \quad (11)$$

The origin in this example is at the middle of the coolant hole; the x axis is in the radial direction while the y axis is in the streamwise direction. ζ is often the lateral distance between film cooling holes, although it is also useful to describe any region of interest¹.

Finally, the entire cooling effect is describable using the *area-averaged* adiabatic effectiveness:

$$\eta_{area} = \frac{1}{\zeta_2 + \zeta_1} \frac{1}{\gamma_2 + \gamma_1} \int_{-\gamma_1}^{\gamma_2} \int_{-\zeta_1}^{\zeta_2} \eta_f dx dy \quad (12)$$

In this last case, γ is often the spacing between film cooling holes (streamwise), although other values may be appropriate in certain situations as with ζ .

2.3 History of Effusion Cooling Research for Rockets

With the availability of liquid fuel and oxidizer, effusion cooling is another option for liquid fueled rockets. Much of the literature relevant to film cooling applications in rocket engines is traceable to Duncan Rannie (6) at the Jet Propulsion Laboratory (JPL) in the 1940's. Rannie was a student of von Karman at JPL and his work coincides with some of the early American development of modern rocket applications taking place at JPL in this era. A notable early application of film cooling for a rocket engine occurred when Aerojet² demonstrated chamber film cooling in 1967 with the ARES 100,000 Lbf thrust chamber (7). Unlike the work of Rannie and other transpiration researchers using porous materials, the ARES experiments used photo etched metal plates (platelets) bonded together to provide the coolant to the transpiration cooled surface. The platelet

¹ For example, in transpiration cooling the hole spacing is small and variable, so it may be necessary to choose values of ζ and γ based on the hardware geometry or other parameters.

² Aerojet itself started by von Karman and a number of his students from Cal Tech (and JPL)(34)

construction addresses one of the principal shortcomings in transpiration cooling for rockets: the difficulty in manufacturing a porous material that effectively delivers coolant in the presence of a pressure gradient (as found in the throat region). Despite this early work on effusion cooling applications for rocket engines, modern rocket engines such as the Space Shuttle Main Engines (SSME) utilize film cooling only for the injector faces (8). Large rocket engines do not typically employ full coverage film cooling on the combustion chamber or nozzle walls.

In the mid-1990's a number of AFIT students performed experimental and numerical studies on transpiration cooling applications for rocket engines. Previous students used a low speed shock tunnel to investigate transpiration-cooling effects on flat plates. Lenertz (9) began a series of research using the same shock tunnel, but with a Mach 2.0 nozzle cooled via transpiration cooling. Later, Landis (10) numerically demonstrated that the Space Shuttle Main Engine (SSME) chamber walls would be 35% cooler using transpiration cooling instead of regenerative cooling. While these students investigated the nozzle cooling problem specific to rockets, they never addressed the curvature effects of the nozzle when compared to a flat plate. More recently, McCall's research (2) is notable for specifically addressing the radial curvature effects present in a rocket engine. In a departure from the previous AFIT studies, McCall looked at film cooling effect in a radial section, showing that increasing curvature generally increases cooling efficiency, up to a point.

2.3.1 Early Transpiration Cooling Models

In 1947, researchers at JPL delivered a series of reports for a missile program contracted to JPL by Air Material Command. Progress report 4-50, *A Simplified Theory of Porous Wall Cooling* by W.D. (Duncan) Rannie (6) contained both analytical predictions of transpiration cooling efficiency as well as experimental results to back up those predictions. Rannie related the temperature change to the blowing ratio as shown in Equation 13.

$$R = \frac{T_\infty - T_c}{T_w - T_c} = \left[1 + \left\{ 1.18 \text{Re}_\infty^{0.1} - 1 \right\} \left\{ 1 - e^{-37 F \text{Re}_\infty^{0.1}} \right\} \right] \left[e^{37 F \text{Re}_\infty^{0.1} \text{Pr}_\infty} \right] \quad (13)$$

where R is the *Rannie temperature ratio*, T_w is *wall temperature*, Re_∞ is the *main flow Reynolds number*, and Pr_∞ is the *main flow Prandtl number*. Rannie's experiments considered only air/air interactions, and as McCall (2) points out, do not factor in the difference between the physical characteristics (such as density) of the main flow and the coolant. In addition, the Rannie model overestimates actual cooling performance by about 15% (11).

Spalding (12) later proposed a general solution to the mass transfer problem as:

$$\dot{m}_c'' = g \cdot B \quad (14)$$

where \dot{m}_c'' is *coolant mass flux*, g is the *surface conductance*, and B is the *driving force*.

Furthermore, the surface conductance is:

$$g = \frac{h}{c_{p,mix}} \quad (15)$$

where $c_{p,mix}$ is the *specific heat of the mixture*, and h is the *heat transfer coefficient*.

Spalding showed that the driving force for the transpiration cooling problem is:

$$B = \frac{c_{p,\infty} (T_\infty - T_w)}{c_{p,c} (T_w - T_c)} \quad (16)$$

where T_w is *surface wall temperature*. Spalding neglected radiation and assumed the specific heats were the same although they are shown here for completeness. The surface heat transfer coefficient is found using Spalding's relationships, leading back to the transpiration cooling efficiency (Equation 9).

Later developments by Simpson, Kays, and others (13) at Stanford bridge the gap to more recent transpiration cooling research. Spalding (12) expressed the cooling efficiency in terms of the blowing ratio as shown in Equations 17 and 18.

$$\frac{C_f}{C_{f,0}} = \frac{St}{St_0} \approx \frac{\ln(B+1)}{B} \quad (17)$$

where C_f is the *cooled skin friction coefficient*, $C_{f,0}$ is the *un-cooled skin friction coefficient*, and:

$$B = \frac{F}{St} \quad (18)$$

Simpson et al. (13) experimentally determined the Stanton number and skin friction factor as a function of the blowing ratio (F) and the momentum Reynolds number (Re_θ), modifying Equation 17 as shown in Equation 19.

$$St = \frac{C_f}{2} = 0.0130 \left[\frac{\ln|1+B|}{B} \right]^{0.7} Re_\theta^{-0.25} \quad (19)$$

At the time, a number of researchers published experimental transpiration cooling data and Simpson sought to evaluate the other data and set conditions for qualification of the test apparatus. The qualification included verifying the un-cooled friction factor ($C_{f,0}$),

Stanton number (St), mean velocity profile (U_∞), and boundary layer thickness. The qualification proved the accuracy of Simpson's test data, something he questioned when evaluating the previous research.

Kays (14) later equated the problem to one in which the momentum and thermal boundary layers are the same thickness because the boundary layer is almost entirely turbulent. In this case the uncooled Stanton number is approximated using Equation 20.

$$St Pr^{0.4} \approx 0.0287 Re_x^{-0.2} \quad (20)$$

where Re_x is the *length scale Reynolds number*. Equation 20 is valid when:

$$0.5 < Pr < 1.0$$

and

$$5 \times 10^5 < Re_x < 5 \times 10^6$$

Combining Equations 17 and 20, the Kays method (Equation 21) algebraically relates the transpiration cooled wall Stanton number to the blowing ratio (via B), the Reynolds number, and the Prandtl number.

$$St Pr^{0.4} = 0.0287 Re_x^{-0.2} \frac{\ln(1+B)}{B} \quad (21)$$

The Spalding (12), Simpson (13), and Kays (14) methods of relating the Stanton number ratio to some equation involving the blowing ratio serve as the springboard for most subsequent transpiration cooling research.

2.3.2 Previous AFIT Research

In 1994, Joseph Lenertz (9) modified a low speed shock tunnel at AFIT to perform transpiration cooling research. Lenertz found the relationship between blowing

ratio and cooling effectiveness was linear when $-0.0035 \leq F \leq 0.0051$. This allowed him to relate the cooling efficiency to the blowing ratio as shown in Equation 22.

$$\frac{h}{h_0} = 1 - 27.381F \quad (22)$$

A modified version of the Bartz equation gives Lennertz the uncooled heat transfer coefficient (15). Equation 23 shows the traditional Bartz equation.

$$h_0 = \left[\frac{0.026}{D_*^{0.2}} \frac{\mu_0^{0.2} c_p}{\text{Pr}^{0.6}} \left(\frac{p_0 g}{c^*} \right)^{0.8} \left(\frac{D_*}{r_c} \right)^{0.1} \right] \left(\frac{A_*}{A} \right)^{0.9} \sigma \quad (23)$$

where μ_0 is *main flow viscosity*, D^* is *throat diameter*, c^* is *characteristic velocity*, r_c is *radius of curvature of the nozzle* (at point of interest), A^* is *throat area*, A is *nozzle area* (at point of interest), and:

$$\sigma = \frac{1}{\left[\frac{1}{2} \frac{T_w}{T_0} \left(1 + \frac{\gamma-1}{2} M^2 \right) + \frac{1}{2} \right]^{0.8-m/5} \left[1 + \frac{\gamma-1}{2} M^2 \right]^{m/5}} \quad (24)$$

where M is the *Mach number*, and $\mu \sim T^m$. The maximum blowing ratio tested by Lenertz (0.0055) resulted in a 14% decrease in heat transfer coefficient. Comparable film cooling efficiency requires orders of magnitude greater blowing ratios, requiring the rocket to set aside even greater amounts of fuel as coolant.

Later, Chen (8) used the shock tube method to investigate a larger range of blowing ratios ($-0.0016 \leq F \leq 0.017$). The maximum coolant mass flow possible, given the available pressure and material porosity, limited the maximum blowing ratio. Chen implemented Lennertz's suggestion to limit the cooling to the throat region where the heat flux was the greatest. Despite limited test data (only three heat flux gauges remained

operational), Chen proposed the following modification to the Lenertz efficiency calculation:

$$\frac{h}{h_0} = 1 - 38F \quad (25)$$

Although never stated explicitly, Chen asserts that the cooling efficiency relationship is linear through his test range. Casual observation of Chen's cooling efficiency vs. blowing ratio figure raises the question of whether a higher order curve fit would be more appropriate.

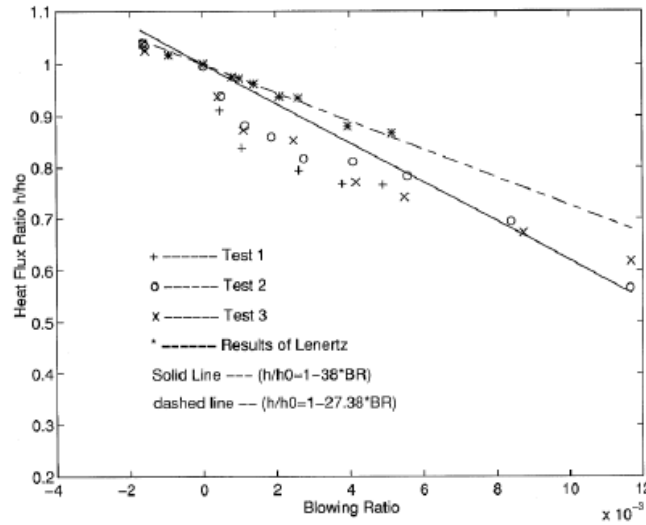


Figure 3: Chen's experimental transpiration cooling efficiency (8)

Unfortunately, Chen does not provide actual cooling efficiency and blowing ratio data. Chen also used a shadowgraph system to verify that the boundary layer did not grow significantly at this blowing ratio, a concern raised by Keener (16). Keener previously showed that the exit Mach number (and velocity) decreased with increased blowing ratios, decreasing thrust as shown in Equation 1.

Following Chen, Landis (10) developed a computer model for transpiration cooling of the Space Shuttle Main Engines. The maximum blowing ratio was limited to 0.010 to stay consistent with Chen. Landis demonstrated that the SSME could be transpiration cooled using a blowing ratio of only 0.004 and that a hot side temperature decrease of 35% is possible for a blowing ratio of 0.010. The computer model also showed the heat flux increased with porosity, although he contributed the increase in heat flux to the decrease in surface area of the larger spheres constituting the higher porosity test cases models. One important result of Landis' work was his finding that the transpiration cooled wall thermal gradient was 72 times the regeneratively cooled wall. The temperature gradient may be a major factor in material selection for transpiration cooled walls.

2.3.3 Current AFIT Research

Immediately preceding this work, McCall (2) designed and built the FCR. More energy is devoted to reviewing McCall's research as this effort springs directly from his work. While most of the research cited by McCall concerns transpiration cooling, he starts by using a computational fluid dynamics (CFD) simulation to modify the Rannie transpiration model (Equation 13) for full coverage film cooling (FCFC). First, combining Equations 10 and 13 yields:

$$\eta_f = 1 - \frac{1}{R} \quad (26)$$

McCall curve-fit the plot of $\frac{\eta_{area}}{\eta_f}$ (Equations 12 and 26) vs. the *film cooling area ratio* (S)

as shown in Equation 27:

$$\frac{\eta_{area}}{\eta_t} = -24.2792S^2 + 4.4087S + 0.0755 \quad (27)$$

The film cooling simulation results approached the transpiration cooling calculations as the spacing between the holes decreased. For the hole spacing cited by McCall as most likely for rocket engine applications, the film cooling effectiveness was only 10-17% of the transpiration cooling efficiency based on the Rannie model. Beyond this point, McCall's research only addresses film cooling and not transpiration cooling.

McCall's (2) CFD results showed increasing the blowing ratio increased the cooling efficiency, as expected. Figure 4 shows the effect of the radial curvature for the 90° compound injection case.

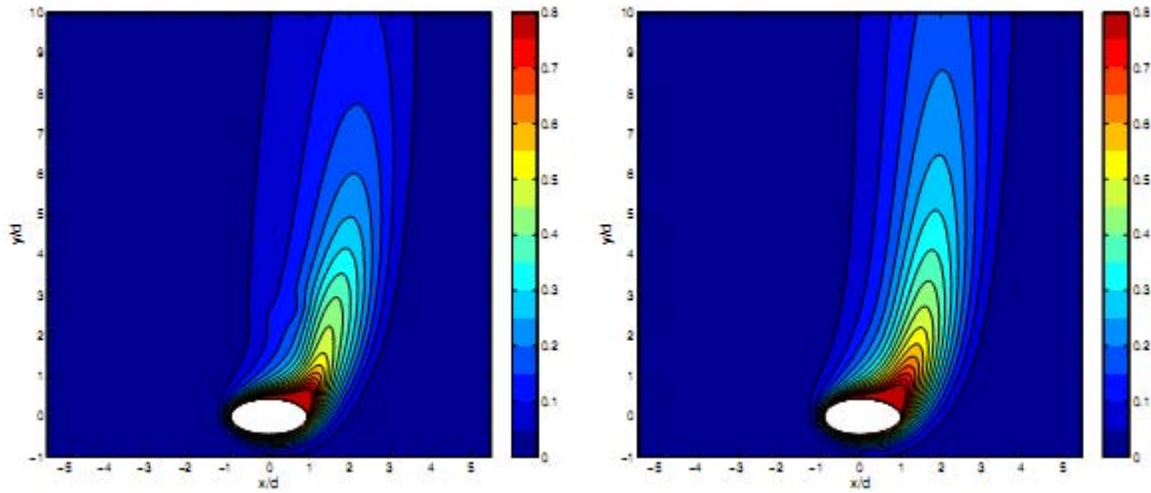


Figure 4: Adiabatic effectiveness for a flat plate (left) and curved plate (D_∞/D_j , right) ($F = 0.5$)(2)

The spanwise cooling efficiency increased as the curvature “cradled” the coolant flow and delayed blowoff. The lengthening of the coolant jet increases the required distance between rows of holes (streamwise). There does appear to be some narrowing of the

coolant flow in the radial (x) direction although McCall does not provide a metric to evaluate it. Presumably, less coolant in the radial direction leads to a decrease in the coolant hole pitch, or radial spacing. A second expected result was that the increase in spanwise efficiency was more pronounced at 90° than at 45° or 0°.

McCall (2) designed the FCR to accommodate data collection from a variety of techniques. Some of the possible techniques include infrared thermography, planar laser induced fluorescence (PLIF), particle image velocimetry (PIV), calorimetry (leading to average heat flux), and emissions testing. Despite the choice of diagnostics, the scope of McCall's research was limited to infrared measurement of air/air³ film cooling due to the number of variables he tested. The test variables include compound injection angle ($\alpha = 0^\circ$ and 90°), density ratio (1.17, 1.76), diameter of curvature to hole diameter ratio ($D_\infty/D_j = 16.0, 32.2, 48.5, 64.4, 97.0$), and presence of a stream-wise pressure gradient (with/without—not characterized). The blowing ratio varied between 0.50 and 1.50 for all cases and the injection angle into the flow (θ) was 30°. Figure 5 shows the two film cooling injection angles, α and θ .

³ air/air refers to the main and coolant flows respectively

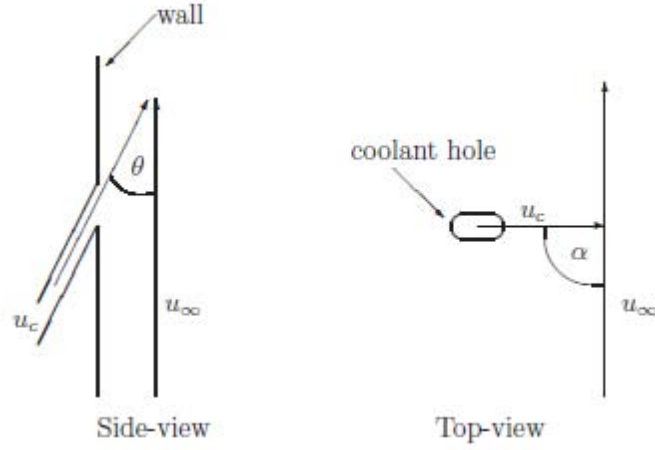


Figure 5: Film cooling injection angles (2)

McCall used closed-cell polyurethane foam to manufacture the test section. The foam would not reach steady-state conditions so a transient technique resulted in h and T_{aw} for each test case.

Equation 28 shows the Buckingham- π solution proposed by McCall to characterize the test results.

$$\eta_{area} = a \left(\frac{D_{\infty}}{D_j} \right)^c F^f (1-K)^k DR^d \quad (28)$$

where D_{∞} is *diameter of curvature*, D_j is *coolant hole diameter*, and K is *pressure gradient*. The coefficients (a, b, c, d) for each test case are show in Table 2.

Table 2: McCall's Experimental Coefficients (2)

| | α | a | c | f | sse |
|-------------------------|----------|--------|---------|---------|--------|
| Curvature Study | 90° | 0.1941 | -0.2806 | -0.5871 | 0.0154 |
| Pressure Gradient Study | 90° | 0.2491 | -0.2352 | -0.4607 | 0.0194 |
| Density Ratio Study | 90° | 0.1556 | -0.1190 | 0.0110 | 0.0203 |
| Curvature Study | 0° | 0.0036 | 0.6815 | -0.5333 | 0.0042 |
| Pressure Gradient Study | 0° | 0.0191 | 0.3737 | -0.3964 | 0.0076 |
| Density Ratio Study | 0° | 1.5222 | -0.6715 | -0.4575 | 0.0092 |

McCall's (2) results are specific to his experiment because the limits of integration for η_{area} , area are not linked to a definition of coolant row spacing and/or hole pitch. Future experimentation with multiple holes may remedy this issue. Despite this limitation in Equation 28 and its coefficients, McCall's research proved that increasing curvature increases cooling efficiency when the coolant encounters a concave surface (due to compound injection). The cooling effectiveness decreased without compound injection.

In addition to the curvature results, McCall (2) proved the streamwise pressure gradient improved cooling efficiency by delaying blow-off, as did an increasing density ratio (ρ_c/ρ_∞).

McCall (2) provided multiple recommendations serving as the starting point for this research. Two of McCall's suggestions address refinements to the simulation and modeling effort. He also recommends studying variations in Reynolds number and turbulence levels in the context of radial curvature, as well as utilizing combustion diagnostics (such as PLIF and PIV) with fuel-based coolant in a combustion environment to calculate performance effects (on thrust and I_{sp}).

2.4 AFIT Test Capability

The AFIT COAL Lab is rapidly expanding its capability to perform modern laser diagnostic techniques for combustion analysis. Recent years have seen a series of students focusing their research on Planar Laser Induced Florescence (PLIF) for the Ultra Compact Combustor (UCC). In addition, one student recently detailed Particle Image Velocimetry (PIV) for the combustion environment of the UCC. Finally, portable infrared cameras are available for temperature measurement. McCall (2) used the infrared camera for his research while Bohnert (17) investigated a Hall thruster inside a vacuum chamber with the same camera.

2.4.1 COAL Lab Setup and PLIF for the UCC

Anderson (18) designed and built the COAL lab for his thesis work in 2006-2007. Lab setup consumed most of Anderson's time, although he discusses a number of intended diagnostic techniques to include: Coherent Anti-Stokes Raman Scattering (CARS), Laser Induced Incandescence (LII), PLIF, and PIV. Koether (19) and Hankins (20) went on to further refine the COAL lab and actually performed PLIF with a Hencken burner (a burner capable of producing a laminar premixed flame). Lakusta (21) was the first student to utilize PLIF in the UCC; he was not able to get temperature or species concentrations from his data, but did identify flame locations inside the UCC cavity-vane area. Lakusta recommended, and Drenth (22) implemented two-color PLIF to obtain temperature data inside the UCC.

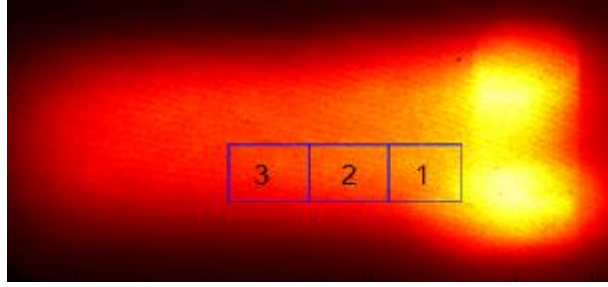


Figure 6: OH concentrations inside the UCC (22)

Drenth refined and documented the methodology to obtain OH concentration using PLIF. Figure 6 shows a false-color image of the OH intensity inside the UCC. Drenth's work is the best source for current COAL lab documentation and procedures. Even though Drenth used the UCC for his research, many of the gas delivery system and laser systems that he describes are also used by the FCR. Drenth also described the experimental technique to acquire time and spatially averaged temperature data. Signal-to-noise limitations forced Drenth to average temperature data, although he did describe various upgrades to both the laboratory and the UCC to increase the PLIF signal.

2.4.2 PIV in the UCC

Thomas (23) departed from previous UCC research to perform PIV inside the UCC. Thomas used PIV to obtain 2-D data for velocity, turbulence, and vorticity in the combustion zone. Silicon carbide particles served as the seed material for the PIV due to their high melting point. Figure 7 shows PIV data from the UCC.

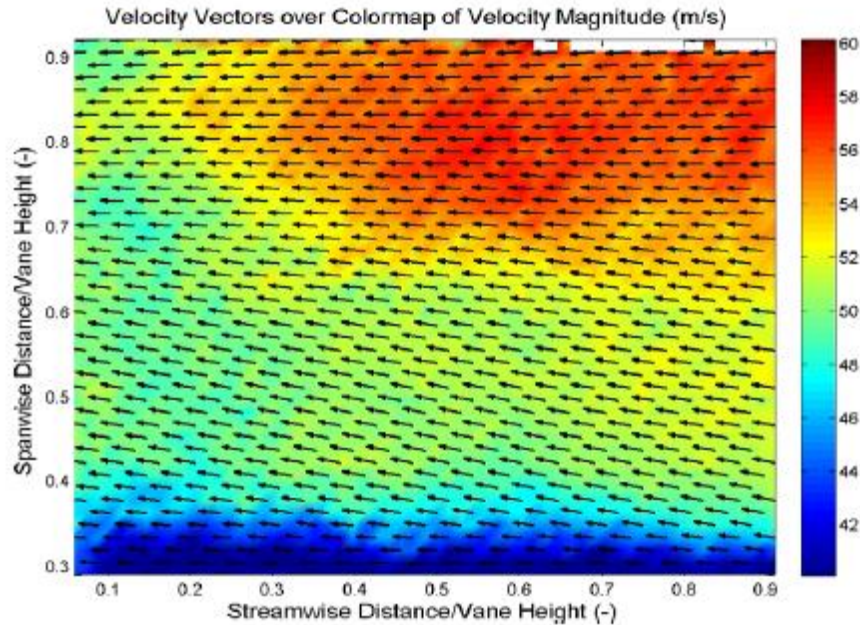


Figure 7: PIV data in the UCC (23)

Thomas used a different laser, camera, and computer equipment than Drenth (22), although many of their optics were compatible. The PIV setup rests on a wheeled cart and numerous labs at AFIT share the equipment.

2.4.3 Infrared Thermography

The infrared energy emitted by an object is a function of that object's temperature. Infrared imaging captures the intensity of the infrared radiation onto a 2-D focal plane where the voltage at each pixel corresponds to the energy absorbed by that pixel. The voltage translates into a temperature, based on the camera and user-defined settings. Bohnert (17) describes the science behind infrared thermography in his thesis on Hall thrusters. Figure 8 shows the possible sources of energy measured by the infrared camera.

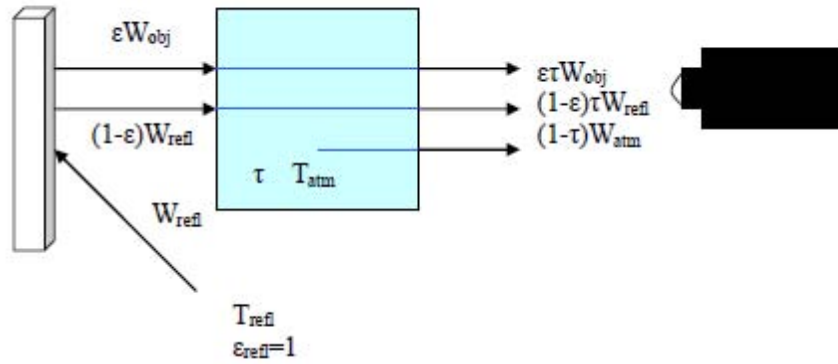


Figure 8: Infrared thermography signal sources (17)

The radiated power (W_{obj}) corresponds to the object's true temperature. Of the many variables that can affect the IR camera's performance, emissivity (ϵ) has the largest effect. Emissivity is a measurement of the radiation from an object compared to a perfect blackbody emitter ($\epsilon = 1.0$). An object with an emissivity near 1.0 emits or absorbs most of its radiative heat. An object with a very low emissivity reflects the surrounding heat (W_{refl}) and emits little of its own. The atmosphere also affects the infrared camera's measurement of the object's temperature. First, it attenuates the signal from the source via the transmissivity ($0.0 < \tau < 1.0$). Second, the atmosphere emits on its own infrared radiation. The lower the transmissivity, the more the atmosphere masks the desired signal. Camera settings to characterize these factors allow the user to obtain the true temperature. Bohnert(17) describes how to determine each factor in detail. The result is a 2-D matrix of temperature values; if a color scale is used to indicate the temperature intensity then the result is an infrared picture as shown in Figure 9.

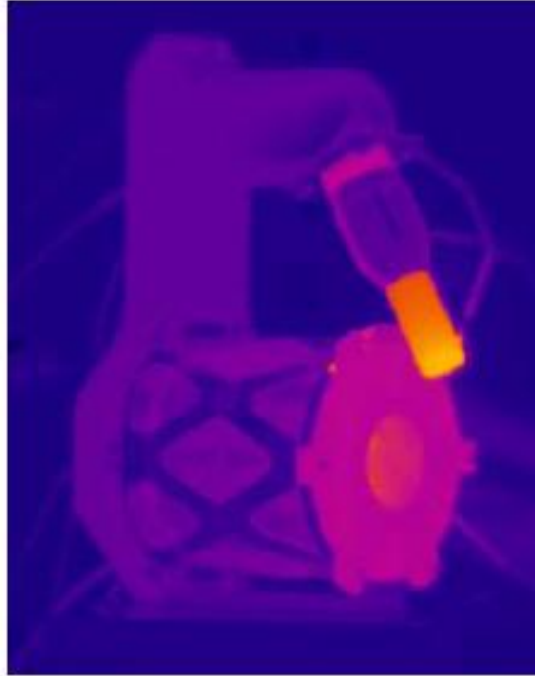


Figure 9: Infrared picture of a Hall thruster (17)

The accuracy of the temperature measurement is tied to the accuracy in defining the camera settings. Infrared thermography is especially useful for this research because the cooling efficiency is a factor of temperature differences and not absolute temperatures, minimizing bias error due to incorrect camera settings.

III. Methodology

3.1 Research Objectives

The FCR was initially intended as a combustion experiment, although McCall ultimately decided to perform his experimentation using only hot air. The introduction of a combustion environment to the FCR required a number of modifications to the rig itself, as well as the laboratory support systems. The research objectives for this thesis included:

- *Build curved test section articles.* Previously the FCR experiment used foam curved sections to test air/air film cooling. The combustion upgrade required stainless steel test sections. The material change significantly complicated manufacture and instrumentation of the test section.
- *Design/test burner system.* The burner system provides the combustion source for the FCR. The burner design must provide proper mass flow rates without instability or risk of flameout.
- *Design/test heat flux measurement system.* While McCall designed the FCR with a water-cooling/heat flux measurement system in mind, it was never implemented. The system included changes to the FCR, the laboratory, and instrumentation for the heat flux measurements.
- *Develop/test appropriate operating regime.* Once the combustion modifications were completed, the test conditions for the main flow, coolant flow, and water-cooling flow were determined. In addition, the LabVIEW® control software

required modification to increase its usefulness and applicability to the FCR.

Finally, infrared thermography and calorimetry results attempted to validate the hardware design.

3.2 Laboratory Setup

The AFIT COAL (Combustion Optimization and Analysis Laboratory) laboratory facilitates research on the Ultra Compact Combustor (UCC), a radial combustion chamber design intended to reduce the length (and weight) of the combustion chamber in gas turbine engines (as commonly seen in aircraft.) The radial burning concept in the UCC also has the potential to increase the efficiency of the engine (22). A series of AFIT Masters students have designed, built, upgraded, and redesigned the COAL lab. McCall (2) first used the lab for non-UCC related research with the FCR. Chapter 2 described some of the UCC research using PLIF and PIV while others have accomplished Laser Induced Incandescence (LII) and Tunable Diode Laser Absorption Spectroscopy (TDLAS). Both portable and laboratory grade emissions analysis equipment are also available.

The COAL lab consists of three major systems and a variety of other equipment for use in various experiments. The three major systems are the fuel/air delivery system, the exhaust system, and the control system. Most experimentation in this laboratory uses all three systems. Other equipment, such as the various lasers, is used selectively for individual experiments. The three major systems are discussed next, while the equipment used for testing will be discussed in the related sections.

3.2.1 Fuel/Air Delivery Systems

The tank farm is an area outside building 640 at AFIT that houses the propane for the FCR burner, the air, and ethylene used in the igniter, as well as a variety of other gases used in the AFIT laboratories. The gaseous ethylene and zero (pure) air are stored in “K” type bottles, while liquid propane is stored in three larger 150-gallon tanks.

Figure 10 shows both the smaller K bottles and the larger propane tanks. Figure 11 shows the gas flow path for each gas used by the FCR. Complete procedures for operation of the gas system are given by Drenth (22).



Figure 10: K bottles (left), propane tanks (right), and propane vaporization system (upper right) inside the tank farm

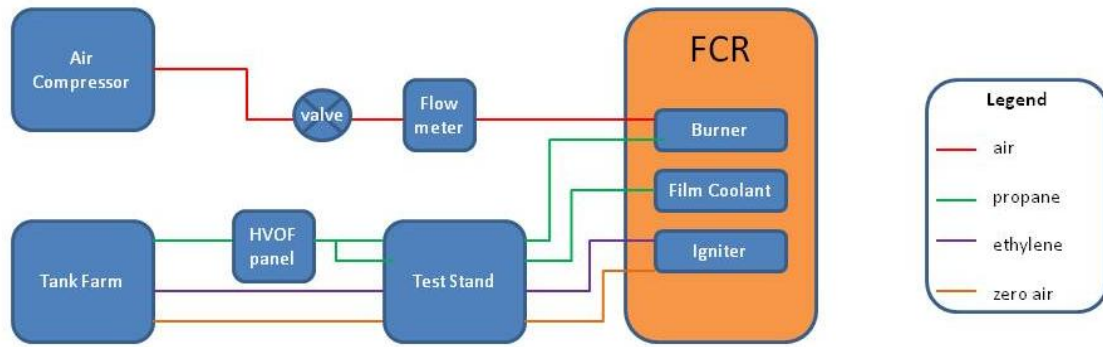


Figure 11: FCR gas flow diagram

Most of the gasses from the tank farm run through copper tubing to a bank of valves on the north wall of the COAL lab. The ethylene and air lines for the FCR igniter are included in these valves. From there, the gas connects to the test stand with polyethylene tubing routed over the superstructure. The test stand routes each gas through a solenoid valve, filter, and mass flow controller (MFC) as shown in Figure 12.

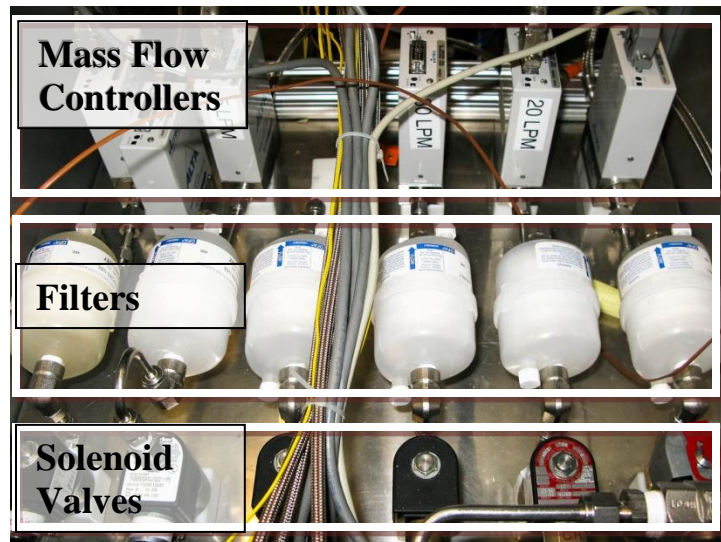


Figure 12: Test stand setup

The operator controls the solenoid valves through the LabVIEW® VI (described in section 3.2.3); the MFCs are controlled with one of the two MKS type 247 digital readout panels shown in Figure 13.



Figure 13: Control panels for MFCs

The setting for each channel is a function of the gas and the MFC for that channel. The procedure to set the MFC is given in Appendix B. The FCR used four channels for the igniter fuel, igniter air, propane coolant, and propane main flow fuel. Table 3 summarizes the fuel system setup for the FCR.

Table 3: Gas system summary

| | Gas | storage | Flow Control | Operator Control |
|-----------------------|---|------------------------------|-------------------------------|----------------------------|
| Igniter fuel | ethylene (C ₂ H ₄) | K bottle | 20 SLPM (N ₂) MFC | MKS control panel |
| Igniter air | zero air | K bottle | 50 SLPM (air) MFC | MKS control panel |
| Film coolant | propane (C ₃ H ₈) | 150 gallon tanks | 100 sccm (Xe) MFC | MKS control panel |
| Main flow fuel | propane (C ₃ H ₈) | 150 gallon tanks | 50 SLPM (N ₂) MFC | MKS control panel |
| Main flow air | laboratory compressed air | 6000 gallon tank (shared) | flow meter/pneumatic valve | LabVIEW®- secondary air |

The liquid propane is vaporized with a heat vaporization system in the tank farm (visible in Figure 10). The system was installed for use with a Sulzer Metco High Velocity Oxy-Fuel (HVOF) Diamond Jet® spray gun. The manufacturer markets the Diamond Jet® for high temperature surface coating applications. AFIT uses the HVOF system for high temperature material testing inside the COAL laboratory. The FCR originally used a smaller traditional gaseous propane tank (100 lb), but eventually switched to the larger liquid tanks due to large amount of propane used during testing. The propane enters the COAL lab in a separate location from the remainder of the gasses from the tank farm. Figure 14 shows the HVOF panel.



Figure 14: HVOF control panel

The propane enters at the bottom center of the figure, runs through a ball valve, a pneumatic valve, and then a needle valve with a rotary control knob. A rotameter shows the flow rate and pressure gauges display the upstream and downstream pressure. A lab

tech forced the pneumatic valve to the open position by disconnecting the air-out line and switching the air-in line to the air-out connector. Forcing the pneumatic valve to the open position simplifies startup procedures by eliminating the need to start the computer and LabVIEW® VI controlling the HVOF setup. Even after removing the pneumatic valve there are still the two valves on the control panel to regulate propane flow, in addition to eight valves in the tank farm, and a solenoid valve and mass flow controller at the test stand. The HVOF panel propane outlet was connected to the test stand in the same manner as the other gasses, although the flow was split to both the main flow and coolant mass flow controllers.

The airflow setup is completely different than the other gasses for the COAL lab. The main airflow comes from a 6000 gallon pressurized tank outside the lab. Two Ingersoll-Rand compressors in an adjacent building supply compressed air to the tank, although one broke down during testing. Figure 15 shows the air supply tanks.



Figure 15: Air supply tanks

The AFIT supersonic wind tunnel shares the tank, and it has the capability to empty the entire tank in seconds. COAL lab operations must be coordinated with the wind tunnel operations to ensure the air supply is not lost during testing.

After entering the lab, the air splits into two lines: the main and secondary line. The FCR only uses the secondary air line. A Fox FT-2 mass flow meter measures the mass flow rate, while a pneumatic valve controls the flow based on operator input to the LabVIEW® VI. Figure 16 shows the flow meter and valve for the air supply.



Figure 16: Flow meter and valve for air supply

Further information on the air supply hardware, installation, and design choice is available in the thesis by Dittman (24) and Anderson (18).

3.2.2 Exhaust System

Stainless and galvanized steel ductwork exhausts the hot gas from the FCR to outside the building. Lakusta (21) installed dual fans to provide redundancy in case of failure. Together, the fans move approximately 108,000 SLPM of air. The current configuration allows vertical installation of the FCR (as with McCall (2)) or horizontal

installation (current setup). Doors over the room exhaust vents isolate the lab from the other parts of the building during testing.

3.2.3 Control System



Figure 17: COAL lab master control station

The COAL lab Master Control Station (MCS, Figure 17) allows complete control of most COAL lab functions from one central station. In the top-center of Figure 17 are the two MKS Type 247 MFC control panels. To the right are emissions testing equipment. Dittman (24) first discussed the California Analytical Instruments (CAI) gas test bench, although Anderson (18) goes into more detail. COAL lab testing has not employed the CAI test bench to date. AFIT installed the Agilent 5975 series Gas Chromatograph (GC) and Mass Selective Detector (MSD) during this research. Future research may utilize the GC/MSD to investigate combustion efficiencies in the UCC. In the left of Figure 17 are a 52'' monitor and computer capable of displaying information

from any of the other eight computers in the COAL lab. The FCR testing used this monitor to display the thermal camera control software and a live video feed. Not shown in the picture are the data acquisition system and myriad of wiring necessary to connect the various sensors to the MCS.

The heart of the MCS is the central computer running LabVIEW® software. Dittman (24) pioneered LabVIEW® in the lab, while many of the subsequent students added functionality. Figure 18 shows the LabVIEW® interface used by McCall (2) and Drenth (22).

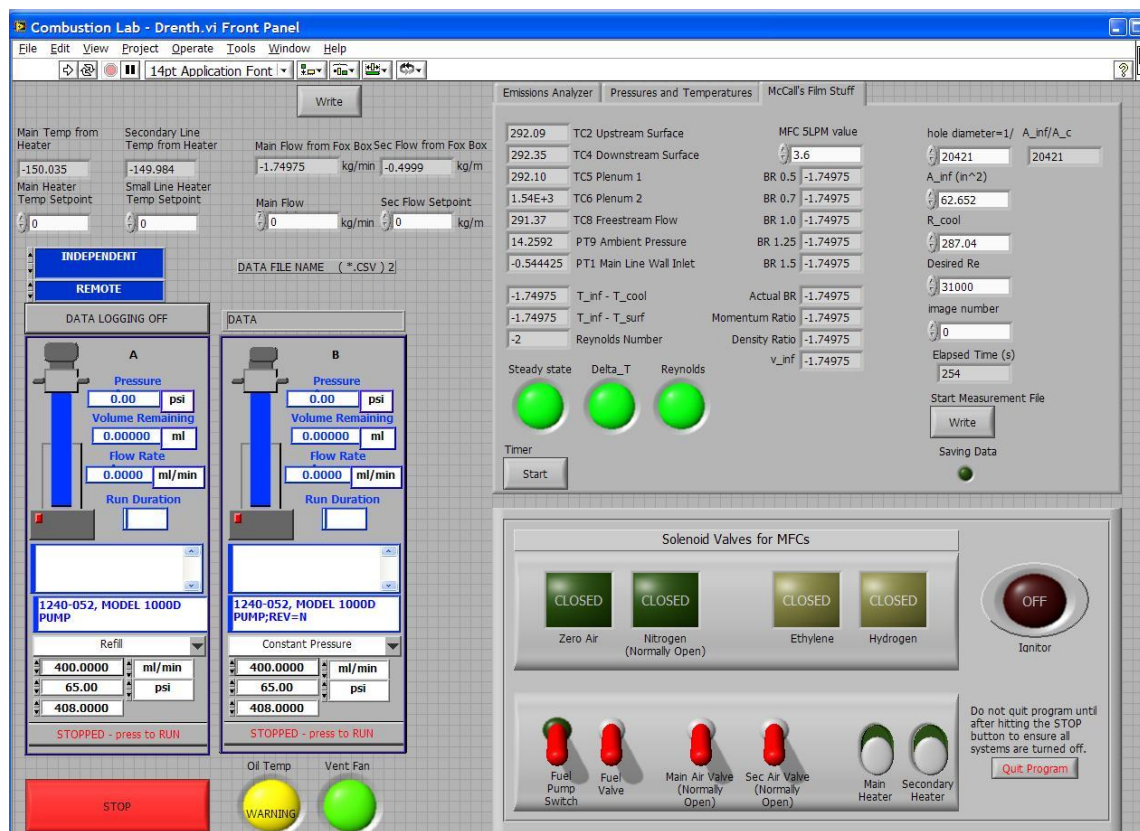


Figure 18: Original COAL lab LabVIEW® VI

McCall added some FCR functionality to the program, but the interface remained largely focused on the UCC. This research is the first major overhaul of the LabVIEW® interface in the COAL lab. Figure 19 shows the current interface.

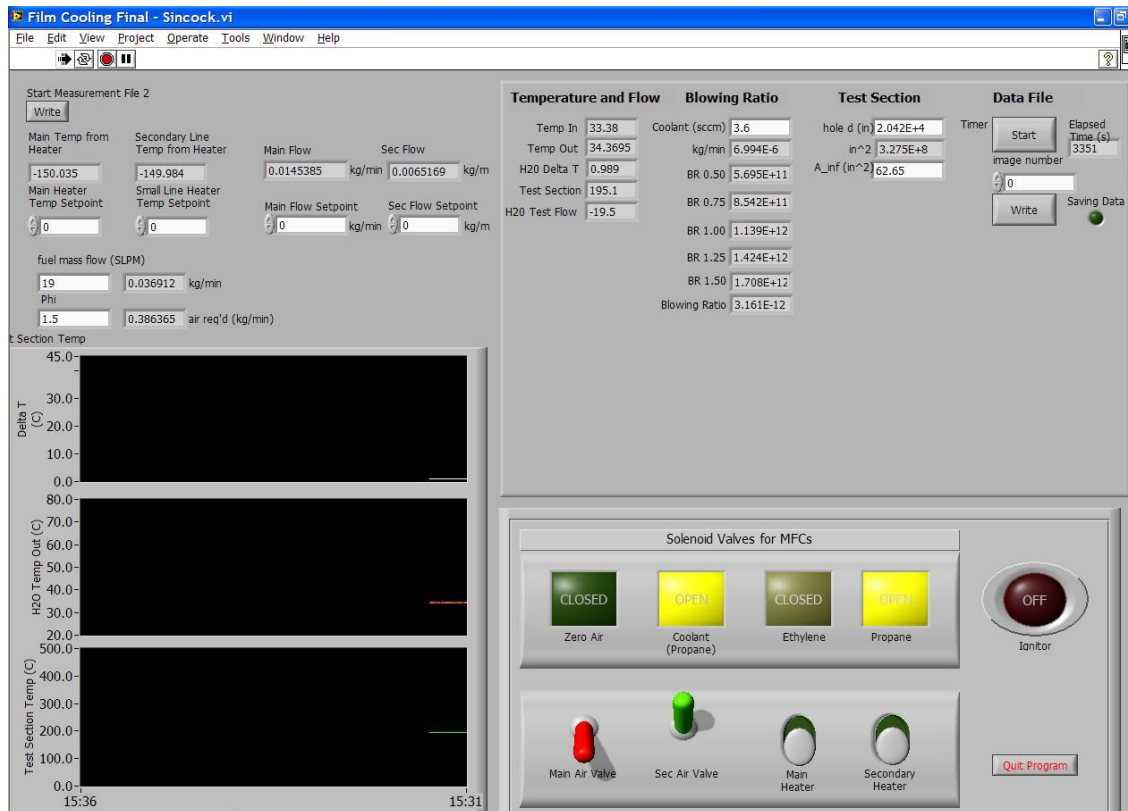


Figure 19: New FCR LabVIEW® VI

While some legacy code remains on the back end of the program, the interface focuses entirely on the FCR. The only visible artifact from the UCC is the main/secondary flow indicators and switches. This was left in place in case using the main flow became necessary at some point (due to secondary flow equipment failure). The most noticeable change is the temperature time history display for the test section, water coolant out, and change in water coolant temperature. This display easily shows when the FCR has

reached steady-state conditions. The water outlet temperature allows the operator to monitor the water temperature to avoid boiling inside the test section. There is no change in how the various valves and airflow settings work, but the VI now performs many of the calculations that were previously performed in others programs (MATLAB®, Excel®) and kept in reference tables. The program determines the required air flow rate when operator inputs the fuel flow rate from the MKS control panel, the desired equivalence ratio. The operator is still required to manually input the air flow rate into the secondary flow setting. In addition, the program displays the propane coolant flow rate for each of the test blowing ratios. Appendix B provides more detail on operation of the LabVIEW® program during testing.

3.3 Film Cooling Rig Modification

3.3.1 Test Section

This research updated the stainless steel test section design proposed by McCall (2) (but not built). Once a viable design solution was reached, test sections were built with curved section radii of 4'' and 6'', with compound injection angles of 0°, 45°, and 90° (6 total).

The curved wall of test sections match 4'' and 6'' schedule 40 pipe (102 mm and 154 mm inner radius). 316 Stainless steel pipe was chosen for the new test sections for its high temperature, corrosion resistant properties, as well as to match the rest of the FCR. Figure 20 shows a CAD drawing of the stainless steel test section.



Figure 20: Test section CAD drawing

The steel test sections contain a cooling channel created by using an outer wall with a larger radius than the inner wall to provide a cooling channel between the walls. Figure 21 shows a cross section of the test section, the water cooling channel in between the walls, and the coolant hole.

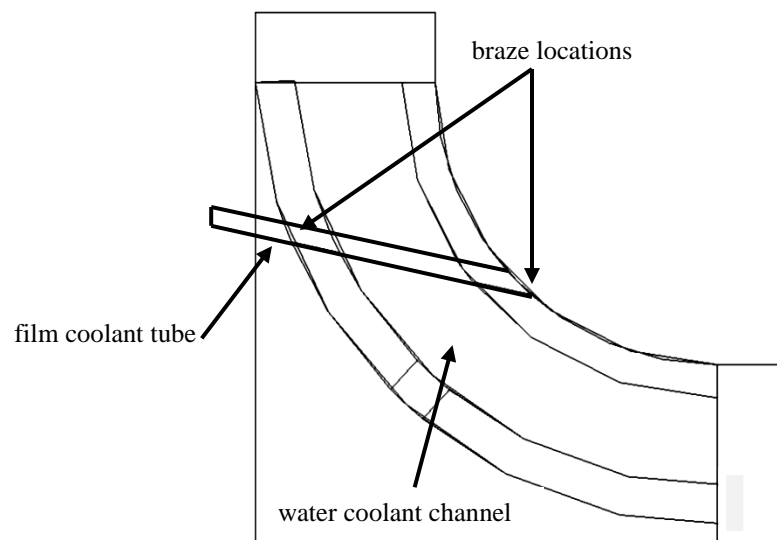


Figure 21: 90° compound injection test section cross-section (flow out of page)

There are three main features of the stainless steel test sections different from the foam articles. First, the steel sections contain the cooling channel necessary to perform the heat transfer analysis. Second, the cooling flow enters the FCR via a steel tube brazed in place. Finally, the thermocouples were brazed through the walls of the test section.

The AFIT machine shop teamed with a local welding company to produce the stainless steel test sections. First the machine shop cut necessary material to produce four 6'' and four 4'' inner radius test sections. Figure 22 shows the various parts that make up one test section.

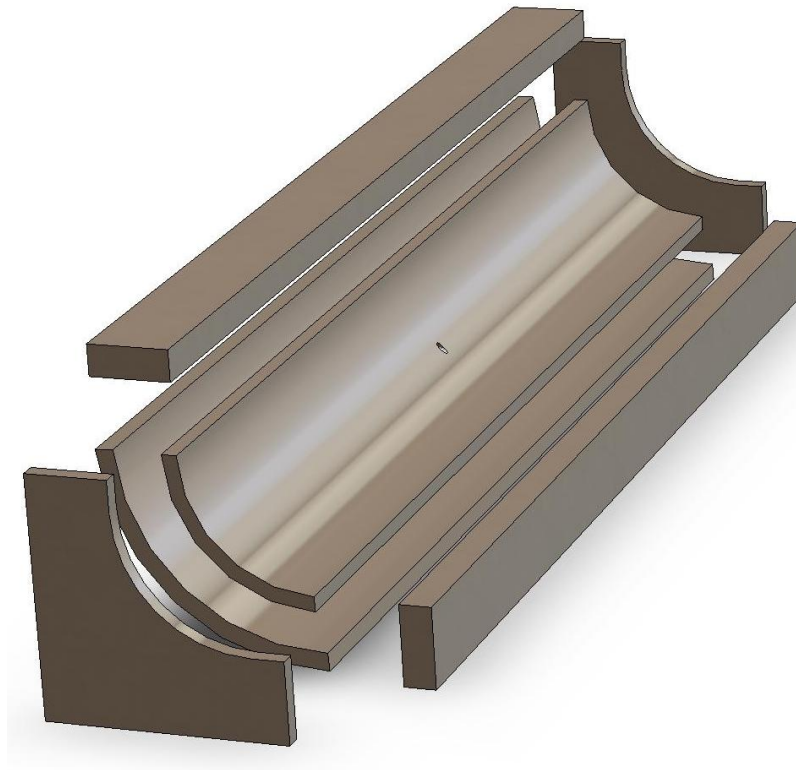


Figure 22: Exploded view of a test section

AFIT contracted the welding company because the test sections were beyond the capability of the AFIT machine shop. The cost of the welding was significant though necessary due to the overall complexity. After the test sections returned from welding, the machine shop fit them to the FCR, drilled the necessary holes for attachment and the coolant tube/thermocouple, and milled the curved section to a constant radius. A computer controlled 3D end mill produced a precise 4'' or 6'' radius, correcting either production flaws or warping due to the welding. The machinist avoided the ends of the section, preventing compromise of the weld in those areas. The lip created by this process is shown in Figure 23.

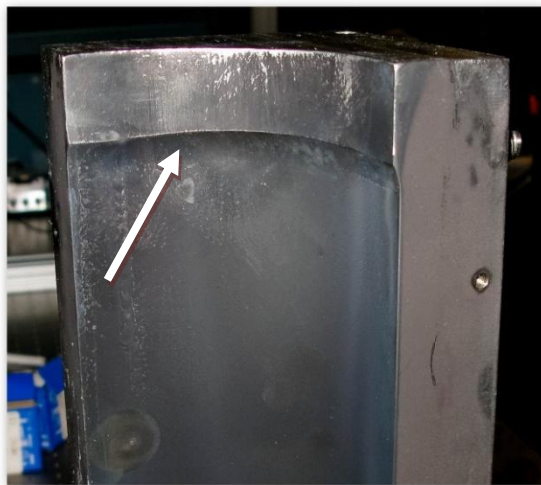


Figure 23: Machined lip on test section

The amount of material removed varied from section to section, even within a single section. The most severe cases removed as much as 0.14'', over half the thickness of the material.

Adding the coolant tube/thermocouple holes was the next step in the fabrication process. The steep compound injection angles, the dual wall, the curved surfaces, and the size of the test section all complicated drilling the holes. The major concern was that a traditional drill bit would slip off the surface before it ever got started. Even if the outside wall was pre-drilled, there was no access to the inner wall and so the problem repeats. One alternative to traditional drilling is Electrical Discharge Machining (EDM). EDM is a method of machining metals by creating a potential between the tool and the material. The voltage discharges as the tool approaches the article, removing very small amounts of material. Colloquially, this is known as hole burning. The tool would not slip on the curved surface because it does not touch the surface. The AFIT machine shop has EDM capability, but neither the maximum hole size nor the overall machine size met the needs of the FCR test sections. Once again, a private contractor provided the setup and burned the holes.

Next, the machine shop brazed the coolant tube and thermocouple to the test sections. In the foam test section, the coolant entered a cooling plenum below the surface of the test section and then flowed through a hole to the inside wall, as shown in Figure 24.

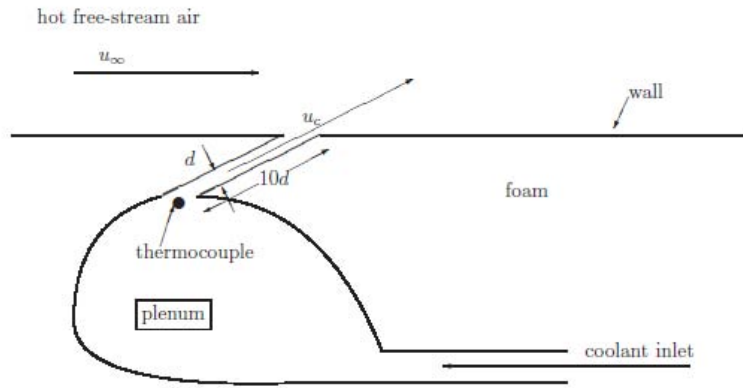


Figure 24: McCall's cooling plenum (2)

The cooling channel of the stainless steel test section prevented a similar implementation so the updated design included a 1/8" 316 stainless steel tube brazed into place. Brazing offered the best combination of high temperature resistance with minimal effects on the surrounding material. Figure 21 shows both braze locations for the coolant tube. The thermocouples were also brazed into the test section, although they are not shown in the figure.

The FCR was initially tested using JB-WELD® high temperature epoxy to secure a 1/8" thermocouple in place (to test applicability in securing both the coolant tube and thermocouple). Numerous issues presented themselves. First, it was very difficult to produce a watertight seal with the JB-WELD®. Water leaked from the cooling channel into the test section at even the lowest water flow rates. Next, it was very difficult to apply a small amount of JB-WELD® and still produce a good seal. On the outside of the test section sealing is not an issue, but on the inside the epoxy lump would unacceptably

alter the cooling and main flow. The final issue is the JB-WELD burned off in the combustion environment.

Precision laser welding was also considered as an option for securing the coolant tube. A private welding company stated they would be able to provide a precise weld between the tube and wall using a laser welding technique. The advantage of the laser welding is that the heated region is very small, it adds very little additional material (weld), and there is little deformation to either the wall or tube. The disadvantage is the cost per unit is very high. While welding was a possible solution, the cost and they in using private contractors made brazing a better solution.

Each test section required four brazed joints total, sealing the thermocouple and coolant tube to both the inner and outer wall. After brazing, the machinist pressurized each section with air to reveal any leakage. Most sections had some leakage, although it decreased as the shop brazing proficiency increased. The last test section brazed was the only section to exhibit zero leakage. Automotive radiator stop-leak effectively stopped any remaining leaks on the inside of the test section. High temperature Room Temperature Vulcanizing (RTV) silicon sealed any remaining leaks in the outer wall joints. Figure 25 shows an outer wall-coolant tube-joint both with and without the RTV sealant.



Figure 25: Coolant tube outer seal, braze on left, RTV on right

With the coolant tube and thermocouple attached, the test sections were nearly complete. Final preparations for testing included attaching the tube fitting for both the water and film coolant and painting the inner surface. The paint is further described in the infrared testing section

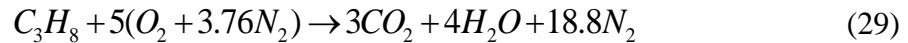
3.3.2 Burner Design

Designing the burner proved one of the larger challenges in modifying the FCR. Consideration was given to the existing design, desired flame type/shape, and desired fuel/oxidizer flow rate. Ultimately, the total flow rate of air and fuel through the burner was the driving factor because it directly ties this research to McCall's (2) work (via the blowing ratio). In addition, the hardware associated with controlling the flow (mass flow controller) is the most expensive and requires substantial lead-time.

The first step in designing the burner was selecting the fuel and oxidizer. Air was the only choice for the oxidizer because the lab did not have enough oxygen available to run the FCR, nor the correct size MFC to control it. In addition, at the beginning of

testing the lab did not have an available channel on the MFC to control another gas. The secondary air supply did not rely on the MFC control panel, and the supply was plentiful. Gaseous fuel was chosen to simplify the burner design and operation. The long-term goal for the FCR is liquid-fuel combustion, similar actual rocket applications. The COAL lab has a variety of fuel available (H_2 , C_2H_4 , C_3H_8), but only the propane (C_3H_8) was available in sufficient quantities to last the entire test program. Propane is also a good choice because it is a very low producer of soot (25). Soot may fog the windows and alter the laser and IR data. Adequately cleaning the soot from the FCR windows may be a laborious process. Finally, a wealth of literature is readily available on propane combustion.

To find the required propane and air mass flow rates, the combustion process for propane with air was studied. Equation 29 shows the stoichiometric relationship for propane-air combustion.



Equation 30 likewise gives the stoichiometric air-fuel ratio for hydrocarbon/air combustion.

$$(A / F)_{st} = \frac{4.76a}{1} \frac{MW_{fuel}}{MW_{air}} \quad (30)$$

where a is *number of moles of oxidizer* (5), MW_{fuel} is the *fuel molecular weight* (44.1 g/mol), and MW_{air} is the *air molecular weight* (28.97 g/mol). The stoichiometric air-fuel ratio is then 15.64, meaning it takes 15.64 grams of air to combust one gram of propane.

Actual testing may require either lean or rich mixtures, so the range of equivalence ratios (ϕ) is needed to solve for the actual air-to-fuel ratio. The equivalence ratio is:

$$\phi = \frac{(A/F)_{st}}{(A/F)} \quad (31)$$

The lean flammability limit for propane is $\phi = 0.51$, so a minimum test value of $\phi = 0.75$ allows some margin. Similarly, the upper test limit was set at $\phi = 2.0$, based on the rich flammability limit of $\phi = 2.83$ (25 p. 287). Using Equation 31, the range of air-to-fuel ratio was, $7.82 < (A/F) < 20.85$. Equation 32 shows (A/F) is the ratio of the air and fuel mass flow rates.

$$(A/F) = \frac{\dot{m}_{air}}{\dot{m}_{fuel}} \quad (32)$$

Setting the fuel mass flow rate to the maximum possible rate for propane (based on the available MFC), yields the air mass flow rate range. For the desired equivalence ratios and the maximum propane mass flow rate (19 SLPM), the airflow rate was between 226.1 SLPM and 602.9 SLPM.

The first burner design was based on the inlet wall section already built but never used in the previous research. The original (unused) inlet wall had a $\frac{1}{4}$ '' hole for the fuel and oxidizer to enter the FCR. In an attempt to decrease the incoming turbulence, McCall (2) instead built a three foot long aluminum tunnel to match the cross sectional size of the FCR. Heated air entered at the bottom of the tunnel and flowed into the FCR. For the combustion upgrade, the machine shop enlarged the hole to $\frac{3}{8}$ '' (the maximum possible given the existing inlet plate). The first burner design is shown in Figure 26.



Figure 26: Original burner design

It featured a co-axial propane-air flow through a 3/8" stainless steel "T" fitting. The fuel enters through 1/8" stainless tubing running through the middle of the fitting, while the air comes in the side of the fitting and flows around the fuel tubing. Many production rocket injectors use a similar co-axial design (26). Testing outside of the FCR showed this size burner would never meet the mass flow requirements. In fact, only 16% (3.1 SLPM) of the required fuel flow and no air flow was ever possible before the flame blew out. The fuel only flame is shown in Figure 27, lifted significantly off the burner and about to blow out.



Figure 27: 3/8" Burner lifted flame

In addition to the blowout issues, the maximum airflow (without flame) through the stainless steel air supply line was only 40% of the requirement.

Significantly increasing the size of the burner was the best solution to achieve the desired fuel/oxidizer flow rates. The blowout velocity for a propane/air flame was calculated to determine the required fuel tube size. The blowout calculation process documented in Turns uses the characteristic flame length to find the Reynolds number, and then a velocity correlation to solve the velocity based on the Reynolds number (25).

The characteristic length (H) is given by:

$$H = 4d_j \left[\frac{Y_{f,e}}{f_s} \left(\frac{\rho_e}{\rho_\infty} \right)^{1/2} - 5.8 \right] \quad (33)$$

where d_j is *jet diameter*, $Y_{f,e}$ is *mass fraction at exit* (1.0), f_s is *mixture fraction*, ρ_e is *fuel density at exit*, and ρ_∞ is *room air density*. Each variable is known, allowing H to be solved directly. The Reynolds number (Re_H) is:

$$Re_H = \frac{\rho_e SL_{\max} H}{\mu_e} \quad (34)$$

where SL_{\max} is *maximum laminar flame speed*, and μ_e is *fuel viscosity at exit*. The Reynolds number leads to the blowout velocity in Equation 35:

$$v_e = SL_{\max} \left(\frac{\rho_\infty}{\rho_e} \right)^{1.5} \left[0.017 Re_H (1 - 3.5 \cdot 10^{-6} Re_H) \right] \quad (35)$$

The blowout velocity for the inner fuel tube is 23.2 m/s, well below the 140 m/s required for the desired fuel mass flow rate. The first burner blew out at 22.7 m/s, close to calculated blowout velocity.

A 2'' stainless steel "T" fitting provided the basis for the next iteration of the burner. A stainless nipple connected the fitting to the inlet wall. The fuel entered through a 3/4'' stainless tube, in the same coaxial fashion as the smaller burner. The fuel tube was also designed to allow it to either protrude from the burner or be nested inside. This design can be seen in Figure 28, next to the previous design for comparison.



Figure 28: 2" burner and 3/8" burner

The blowout velocity for the new fuel tube is 157 m/s, while the propane velocity is only 1.75 m/s. The maximum air velocity was 5.62 m/s (at $\phi = 0.75$). The blowout calculation does not apply to a premixed or co-axial flow, so the largest fitting size available was chosen for the new burner design. While the calculation does not directly apply to co-axial flow, it still gives insight into the behavior of the flame. With the new design, flow velocity should not be an issue.



Figure 29: 2" coaxial burner flame

Figure 29 shows the 2'' co-axial burner flame at $\phi = 1.55$. Additional airflow extinguished the flame. While the flame is lifted, it is not due to the gas velocity (see above), rather, it is probably due to a lack of mixing at the burner exit.

The 2'' burner performed better than the 3/8'' burner, but it still did not achieve the required mass flow requirements. Altering the fuel tube length proved the worst performance came when the tube was the furthest out, blowing out at only 10% of the desired flow rate. Lowering the tube into the fitting boosted the flow rate to 40% of the requirement, but at this rate the flame was unstable and would occasionally blow out with no warning. Turbulence resulting from the ninety-degree turn made by the air is most likely the cause of the instability in the flame for this configuration. The burner was reconfigured so the air entered the bottom of the fitting and the fuel tube on the side, but

the turbulence created by the fuel tube crossing the airflow extinguished the flame before reaching full flow.

In another attempt to straighten the airflow, the outer section of the burner was packed with 1 ½'' pieces of 1/4'' stainless tubing. This helped somewhat, but the flame blew out at 55% of the desired flow, and it was still unstable. Again, it appeared that turbulent pockets of air were randomly blowing out the flame. The next step was to allow the fuel and air to mix fully inside the fitting, possibly preventing unmixed air from blowing out the flame. The fuel tube was retracted to a point below the air inlet and additional 1/4'' tubing was packed into the nozzle. It was hypothesized that the tubing would keep the flow straight out of the burner and keep the flame out of the "T".

Immediately upon starting the test, it was obvious the tubing was not sufficiently small to keep the flame out of the fitting. Despite this issue, the flame appeared stable so the air mass flow was increased in small steps.

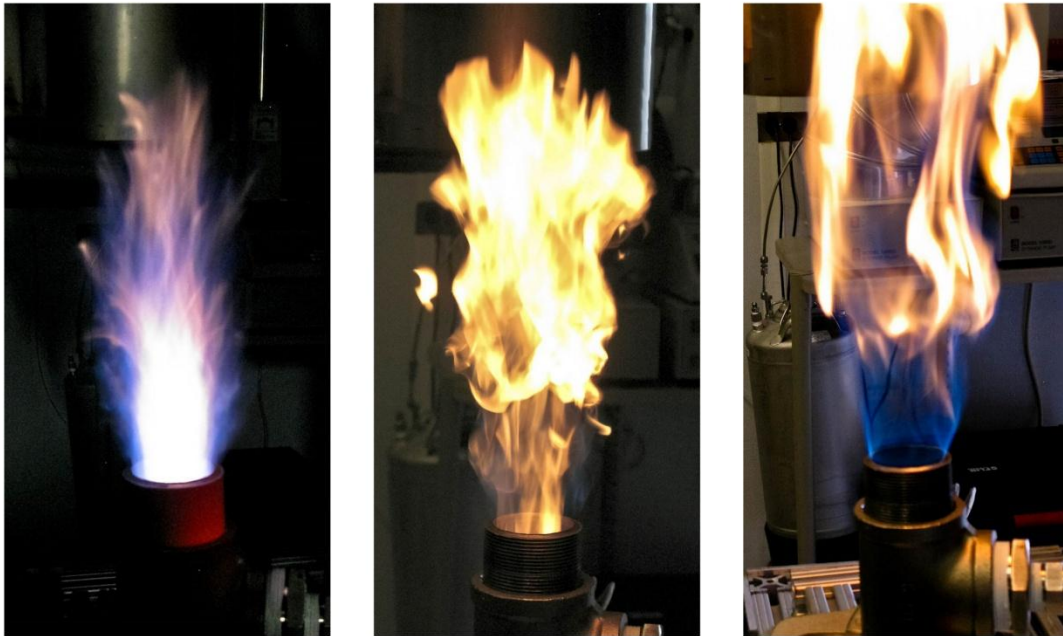


Figure 30: 2" Burner, increasing ϕ (left to right)

The flame decreased in luminosity and length as the airflow increased. This result was expected because the flame was changing from a diffusion flame to a pre-mixed flame. Around 50% of the desired air flow, various parts of the burner began to glow red and the combustion could be best characterized as violent (loud, very turbulent). Flow was increased to 100% but by this point the nipple was bright orange, the fitting was bright red, and the 1/4" tubing was melting. The component melting along with the general safety concern from having a violent flame inside the fitting caused this design to fail.

The previous design demonstrated that allowing the fuel and air to mix inside the fitting would lead to the desired flow rate. By keeping the flame out of the fitting, the

melting and safety issues are eliminated. To keep the flame outside the burner body, an insert was designed for the nipple section. The insert is shown in Figure 31.

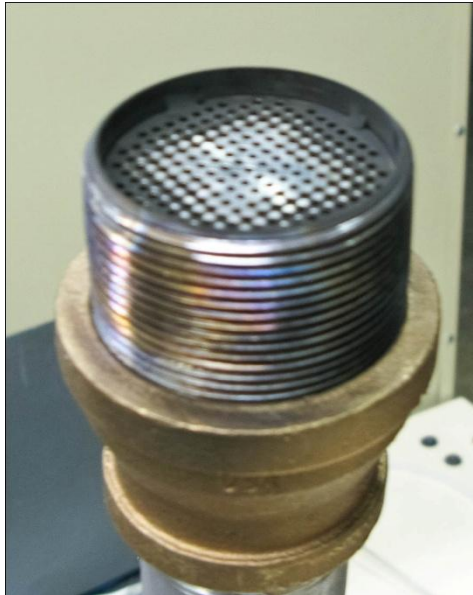


Figure 31: Burner insert

Designing the insert involved three considerations:

1. Maximizing the open area to avoid blow-out (minimize velocity)
2. Minimizing the hole size to prevent flashback
3. Factor in machine-ability concerns with the hole size and proximity

As a starting point, the maximum velocity was set to 18 m/s to avoid blowout.

With the mass flow rate and velocity, the total area of all the holes is constant. To prevent the flame from propagating through the holes, the maximum hole size must be less than the quenching distance for propane. The minimum quenching distance for propane is 0.071'' (25); the insert design had 193 holes each with a diameter of .068''.

This iteration of the burner design did keep the flame out of the “T”, but once again, the burner was plagued by random blow-outs and instability. The flame did not lift off, so the gas velocity was not an issue. Based on the theory that a lack of mixing was causing the blowouts, small stainless steel beads were placed into the nipple (~1.5” deep) to encourage mixing. The steel beads in conjunction with the nipple insert finally allowed full flow combustion with the burner. Despite the apparent solution, the beads presented a design challenge. In the burner testing, the beads rested in the nipple, supported by the insert. With the horizontal configuration of the FCR for this testing, the beads would spill out of the nipple and into the body of the box. There are many possible solutions to this problem, but most involved the machine shop producing more hardware. In this case, a simpler solution was to put the “T” upstream of the nipple/insert and allow the gasses to mix along some length of pipe. The hardware necessary to build a 2” burner with an 18” long, 1.5” mixing pipe was on hand and put to use. No beads are required when using the mixing tube. Figure 32 shows the final burner configuration next to the original for comparison.

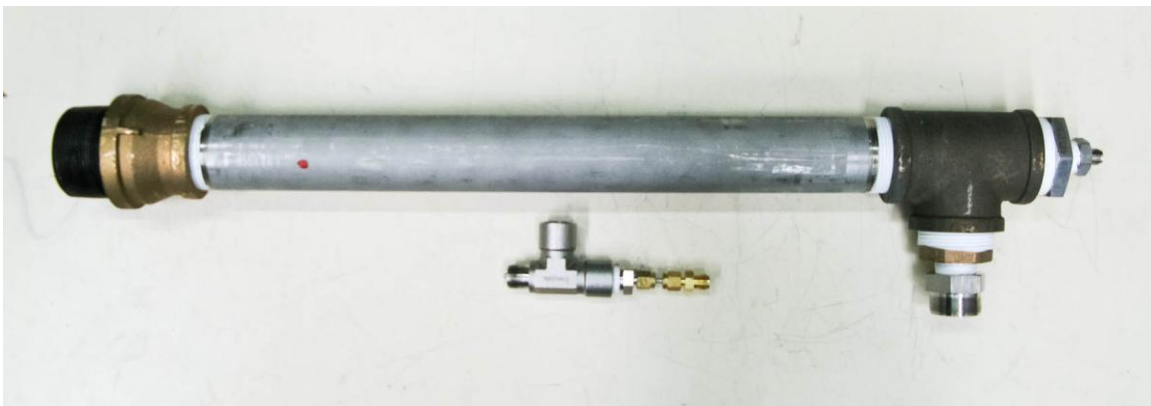


Figure 32: Final burner configuration

Not only did this configuration allow for full flow combustion in a horizontal position, but it also had the straightest (most laminar) flow of any tested configuration.

Chapter 4 will further discuss the final burner design and flame.

The larger burner diameter forced rebuilding of the inlet walls. The old and new inner inlet walls (without the cover) are shown in Figure 33.



Figure 33: Old (left) and new (right) inlet wall

In addition to increasing the burner size, the new walls move the flame closer to the test section and add some material around the window (on the inner wall) to provide a better seal for the water coolant.

3.3.3 Water Cooling-Heat Flux Measurement

The water-cooling feature of the FCR protects the metal from the hot combustion environment, along with providing a method to quantify the heat transferred to the rig.

The AFIT labs have built-in coolant lines using a 30% propylene glycol coolant, but plain tap water was used due to concerns related to fluid loss in the coolant system along with the environmental issues related to any leaked fluid.

Tap water was also chosen because it is convenient and cheap. Garden hoses connect the source to the inlet manifold and the outlet manifold to the drain. The FCR leaked at various times in various places, but the leaked water posed no environmental risk. No pump is required to move the fluid through the system due to the inherent head pressure at the tap. The main drawback to tap water is its cleanliness. A filter was placed in-line with the inlet hose to stop large contaminants from fouling the system, but nothing was done to address hard water build-up. Even after short test runs, calcium carbonate buildup was evident on the interior of the FCR walls. The small passages in the needle valves and flow meters are particularly susceptible to the hard water deposits. .

The inlet and outlet water manifolds are not an actual part of the FCR, but are critical to collecting the heat transfer data desired for the calorimetry experiment. Along with splitting the flow to each wall, the manifolds measure temperature and flow, and control flow to each wall.

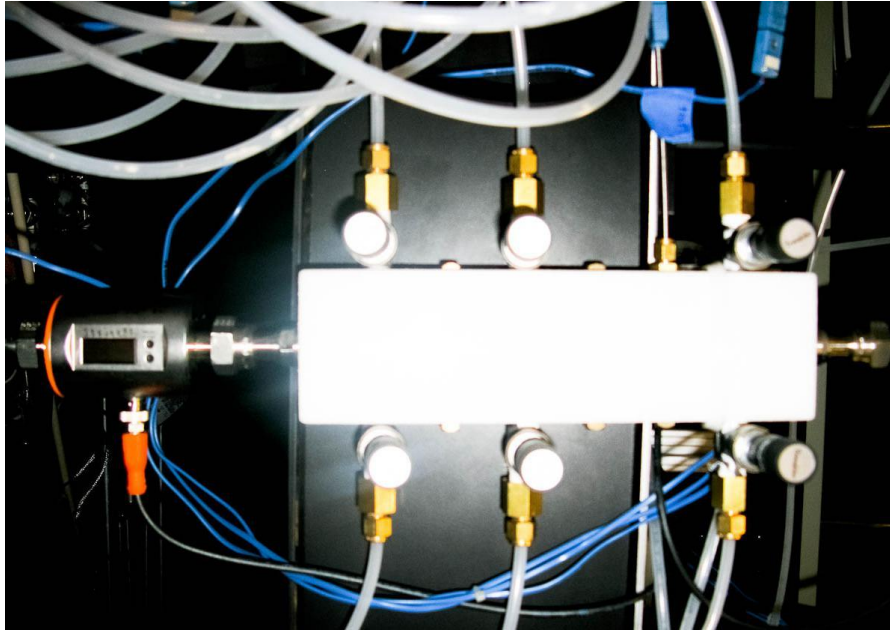


Figure 35: Inlet manifold

Figure 35 shows the bottom portion of the water-cooling inlet manifold. The top portion contains a valve and flow sensor for the test section flow. The first component of the inlet manifold is a 396 gallon-per-hour magnetic-inductive flow sensor, approximating the observed maximum volumetric flow rate of a standard tap. The flow meter has a digital display as well as digital and analog output. The analog output (4-20 mA) was wired to the control computer data acquisition system and brought into LabVIEW®. Next, the water enters a Delrin® (polyoxymethylene plastic) manifold that splits the flow into seven parts. The incoming temperature was measured using a “T”

type thermocouple due to their accuracy at relatively low temperatures (the greater of 1°C or 0.75%)(27). The thermocouple connects to the control computer and imported into LabVIEW®. Needle valve with Vernier handles control flow from the manifold to each wall of the FCR. The Vernier handles provide precise control of the flow as well as repeatability between runs. The film cooling is expected to primarily affect the test section wall, so an additional 78 GPH flow meter was added in line with the coolant flow to the test section. The inlet temperature in to the test section is assumed equal to the overall temperature measurement in the inlet manifold.

$1/4''$ polyethylene tubing connects the inlet and outlet manifold to the FCR. The tubing connects to the outer wall with a $10/32''$ National Pipe Thread (NPT) fitting and gasket. The thin ($1/8''$) outer wall necessitated a small, shallow fitting. Despite the included gasket, the $10/32''$ fitting was prone to leaks, stripping out the hole, and coming loose.



Figure 36: Outlet manifold

Figure 36 shows the outlet manifold. The temperature is again measured using “T” thermocouples, but this time it is measured for both the test section and the overall flow. The seven lines combine into one and then the hot water flows out to a drain built into the floor of the lab.

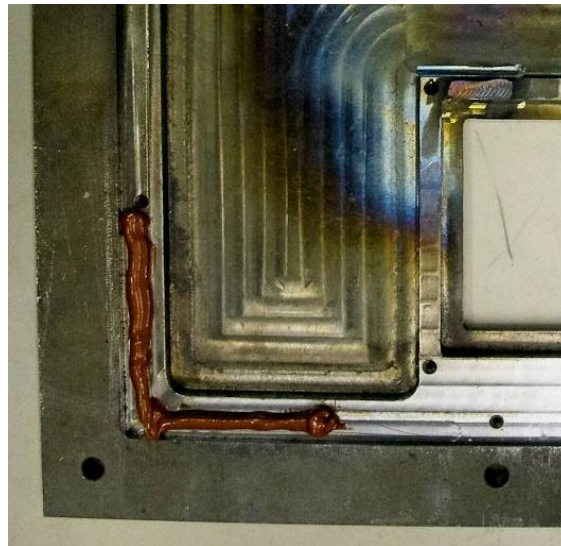


Figure 37: Inner wall with RTV applied (not yet sealed)

The other major modification to the system to allow water-cooling was sealing the cooling walls. Figure 37 shows part of an inner wall with RTV applied to a portion of the mating surface. A high-temperature silicon RTV gasket sealant intended for automotive (oil and transmission pan gasket) applications provides the seal between the inner and outer walls. Once a bead is placed around every mating surface the outer wall is fastened to the inner wall and the RTV is allowed to fully cure. The screw holes are particularly vulnerable to leakage and extra sealant was required in these areas. The lessons learned section describes the procedure for applying the RTV gasket. Even with the best possible sealant application, leakage will occur at high flow rates. The Vernier handles limited the

flow rate to acceptable levels to prevent leakage. The drawback to limiting the water flow is some minimum flow needs to be maintained to prevent boiling in the walls. Once the water boils, the temperature is meaningless.

Each panel was tested with flow rates up to 20 gph (gallons per hour). Some panel had minor leaks, especially around the fittings for the tubes carrying water from/to the manifolds. Any leaks would be sealed using RTV once the FCR was assembled. Chapter 4 describes the performance of the heat flux measurement system and the changes required to operate the FCR.

3.3.4 Other Modifications

A number of smaller changes were also required to prepare the FCR for combustion and testing. The ignition system for the propane/air mixture came directly from the UCC. Anderson (18) initially built the igniter assembly, while Lakusta (21) was responsible for characterizing its operation. The igniter assembly is show in Figure 38.

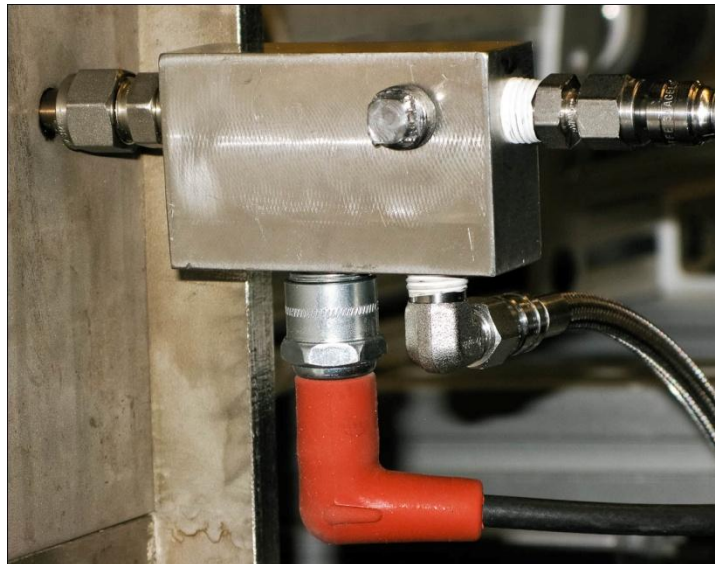


Figure 38: UCC/FCR igniter

The igniter uses an automotive spark plug to ignite an ethylene/air mixture inside the igniter body. The spark plug is controlled through LabVIEW® while the gasses are controlled through the MKS mass flow controller panel. The ethylene/air mixture ignites inside the igniter body and then the flame travels through a 3/8" tube to the FCR body. Drenth (22) showed the original igniter tube was quenching the flame and a shorter tube was more effective. The FCR uses the shortest practical tube length still with the fitting common to the UCC. Propane ignites quickly so the igniter is not required to sustain a flame, although testing showed that a steady flame is possible (Figure 39).

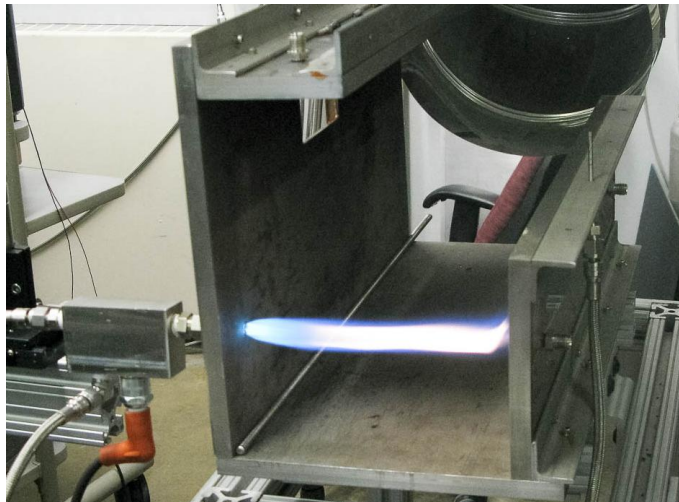


Figure 39: Ethylene/air igniter operation

Windows were also necessary for the FCR. The windows would protect the cameras from the flame, direct the flow of hot combustion gas toward the nozzle and exhaust system, and stop room air from reaching the fuel-rich combustion gases (thereby altering the fuel/air mixture in the rig). McCall (2) specified sapphire windows, although

previous experience with quartz in the UCC led to its use in the FCR. The quartz window is shown in Figure 40.

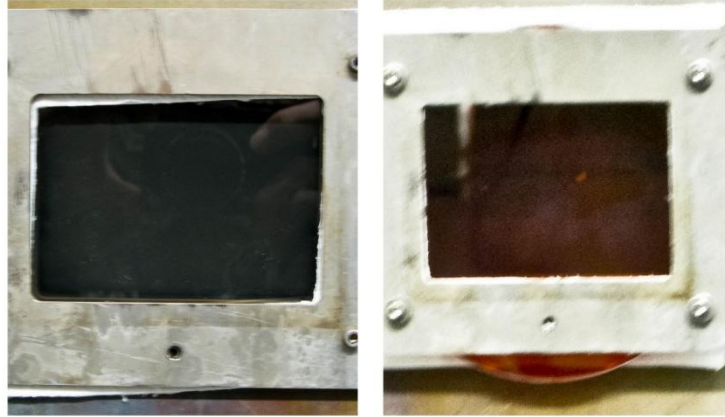


Figure 40: Quartz and zinc selenide (ZnSe) windows

Fiberfrax, a high temperature insulating ceramic paper, initially served as a gasket on both sides of the window. The UCC used the same Fiberfrax material (1/8" 970-J) for gaskets with no issue, but the environment of the FCR led to the gasket combustion. While the gasket was believed to be a non-combustible material, a call to the manufacturer revealed the presence of a small amount of organic material serving as a binder. The representative recommended a slightly different material, where the organic material was baked out of the product during manufacture. The new product (1/8" 882-J) was significantly more fragile, but it no longer caught fire during testing.

3.3.5 Operating Regime

Testing the operating regime of the FCR began once the combustion related modifications to the FCR completed. The three major questions answered by this testing are: what are the correct starting conditions for the igniter and burner, what main and

coolant flows are necessary to achieve the correct blowing ratios, and what water flow is required through the cooling channel of the test section.

Drenth (22) gives the igniter settings for the UCC. As originally designed, it was difficult to achieve a steady flame in the UCC due to the igniter tube length, as discussed in section 3.3.4. To prevent the same issue in the FCR, the igniter was first tested outside the FCR, but with the intended length of stainless steel tube attached. The starting conditions for the igniter are shown in Table 4. The igniter was then tested installed in the FCR, but without the end caps or test section, and then finally in the complete FCR. The igniter never failed to start when properly configured.

With the igniter installed and tested, it was time to find the starting conditions for the main fuel/air mixture and verify the equivalence ratios found during the burner testing. Testing for the starting conditions was largely a trial and error process, although the lessons learned during the burner testing certainly aided the process. Two lessons were particularly valuable. First, there was an upper limit to the starting mass flow rate, lower than the operating limit. Similarly, the lean starting limit is higher than the operating limit.⁴

From an operations standpoint, the easiest solution would be to start at the intended operating condition. The burner testing generally proved that the rich case was more stable than the lean case, so testing inside the FCR began at $\phi = 1.5$ (the richest intended equivalence ratio). The test plan was to change the air mass flow rate to vary

⁴ A lean mixture has an equivalence ratio (ϕ) less than one. A higher lean starting limit means that the FCR required a richer mixture to start than to operate.

the equivalence ratio, and change the propane coolant mass flow rate to vary the blowing ratio. In this scenario the propane main flow would always be at its upper limit (~19 SLPM). With this in mind, the propane set point was 19 SLPM with the appropriate air mass flow rate. At this setting the main flow was not attached to the burner, instead the igniter flame acted as a flame holder for the main flame. Consequently, the main flame would not stay lit without the igniter. The air flow was reduced by half for the second test ($\phi = 3.0$), but the rig once again failed to start. During the open-air burner testing there was no rich limit because the mixture immediately exited into a semi-infinite reservoir of air, but the FCR restricted the air to whatever was present in the mixture. Reasoning that the decreased air flow was causing the mixture to reach the rich flammability limit, the fuel mass flow rate was decreased until the rig started reliably. The correct starting conditions for the FCR are shown in Table 4.

Table 4: FCR starting conditions

| | |
|---|-------------------------|
| zero air – igniter | 12.5 SLPM |
| ethylene (C ₂ H ₄) – igniter | 1.35 SLPM |
| propane (C ₃ H ₈) – burner | 12.5 SLPM |
| lab air – burner | 198 SLPM (0.250 kg/min) |
| propane (C ₃ H ₈) – coolant | N/A |
| water – test section cooling | 10 gph |

The flame attached to both the burner and the exit nozzle because the flow exited the FCR with excess fuel. As expected, the outer flame diminished and then disappeared completely with decreasing ϕ . The starting flow is less than the test flow conditions so the fuel and the air should be incrementally increased to the max fuel flow point. If the air is increased entirely at once then the flame will blow out. If the fuel is increased at once then the rig reaches an unsteady operating condition at $\phi = 2.1$ where the flame oscillates between the outside and inside the box. This condition is shown in Figure 41.

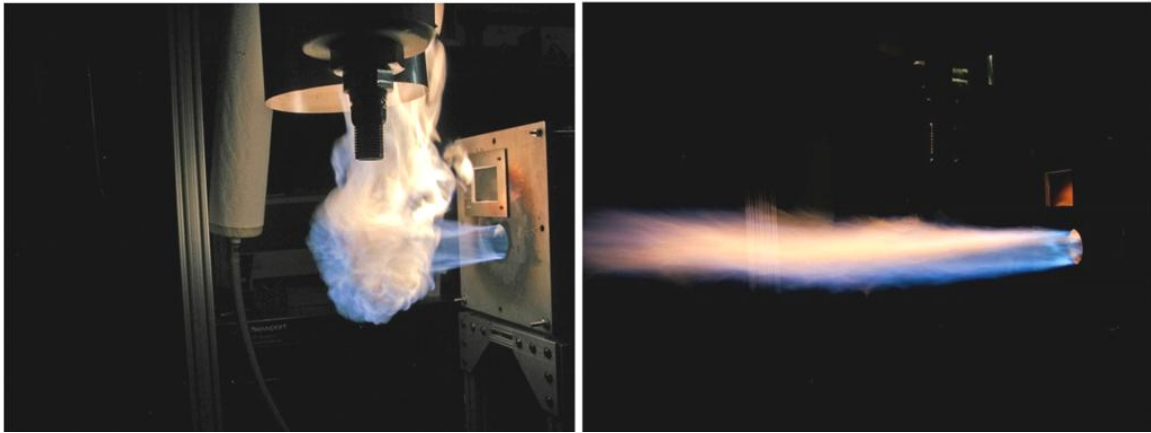


Figure 41: Unsteady operation

The final operating condition test was verifying the range of equivalence and blowing ratios. The air and fuel flow rates were increased incrementally until reaching the max fuel flow rate at $\phi = 1.5$. Next, we increased the air flow, decreasing the equivalence ratio. As ϕ decreased, the interior flame decreased in size, similar to the open-air tests. At $\phi = 0.85$ the flame detached from the burner and turbulently swirled around the inside of the FCR. To avoid this condition, the lower test equivalence ratio needed to remain at 0.90 or greater.

With the upper and lower equivalence ratios tested and set, the coolant flow was determined. Testing verified operation of the FCR with blowing ratios from 0.5 to 1.5. There was no noticeable change in the main flow or flame. Chapter 4 will discuss the IR testing of the coolant flow.

3.4 Testing Methodology

Designing the testing methodology goes hand in hand with designing the test rig. Build issues sometimes drove testing methods, such as when the total heat flux measurement was abandoned due to issues with the water-cooling in the sidewalls. In others cases, the tests necessitated changes to the design, such as when the zinc-selenide window addition to accommodate infrared measurement. In most cases the test methodology took precedence unless the issues absolutely could not be overcome.

3.4.1 Infrared Surface Temperature Measurement

McCall (2) first performed infrared testing in the FCR for his earlier work. Figure 42 shows the test setup used by McCall.

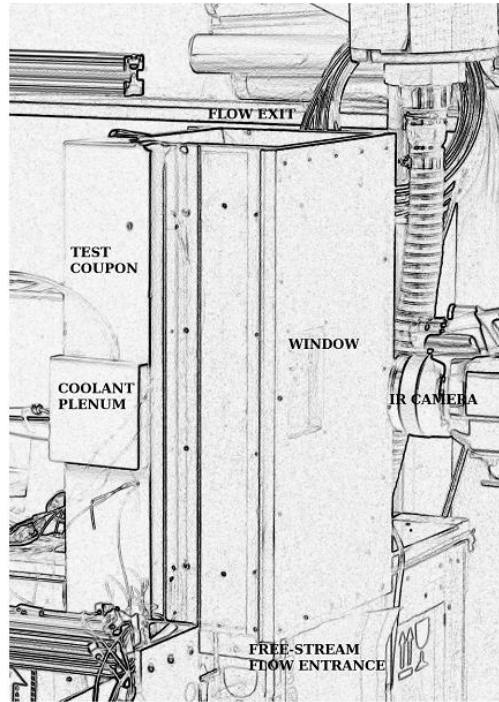


Figure 42: McCall's infrared test setup (2)

The addition of the end caps and burner prevented vertical mounting of the FCR. Placing the FCR horizontally also permits easier access for laser diagnostics.



Figure 43: Horizontal test setup

Section 3.3.4 describes the quartz windows, but the first infrared test with the FCR revealed that quartz does not transmit infrared wavelengths. AFIT's IR camera detects wavelengths from 7.5-13 μm (28) while the standard quartz windows initially ordered for the FCR modification do not transmit wavelengths longer than 3 μm . A common material used for infrared windows is zinc-selenide (ZnSe). The transmissivity for the ZnSe window in the FCR is around 70% for wavelengths between 0.6 and 11 μm , as shown in Figure 44.

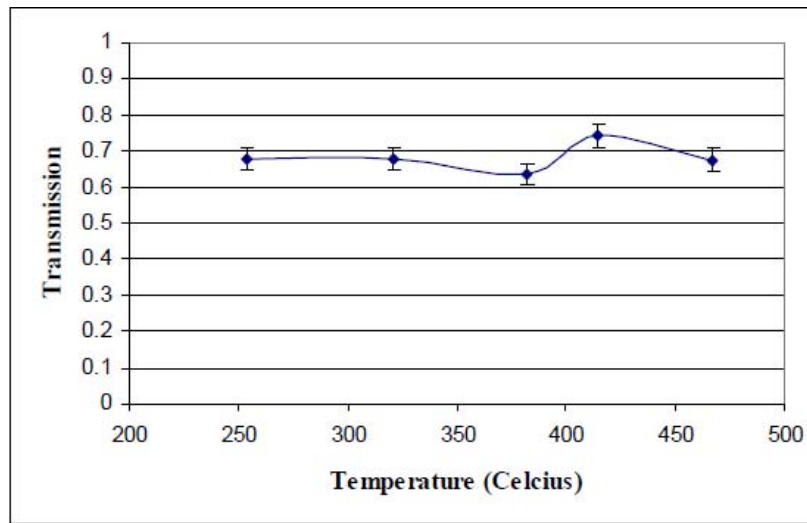


Figure 44: ZnSe window transmissivity (17)

The long lead-time for large custom ZnSe windows prevented ordering of a custom window for the FCR. Fortunately, the AFIT Space Propulsion lab owns a 5'' ZnSe window for infrared testing inside a vacuum chamber. The FCR window is 3'' x 4'', the diagonal dimension being 5''. No modifications were necessary to incorporate the ZnSe window.

The second modification to the FCR related to the infrared testing was painting the test sections. The polished test sections have an emissivity in the range of ~0.18-0.35, compared with the painted sections emissivity of ~0.95. In practice, this meant that the polished sections reflected the background temperatures, while the painted sections emitted more IR radiation.

The long direct exposure to direct flame necessitated high temperature paint. A variety of products is available for use in engines, furnaces, and stoves. VHT® Flameproof flat black paint was available online and chosen for the FCR. VHT® Flameproof is a ceramic spray paint able to withstand temperatures up to 1093°C (2000°F). Three coats of paint were applied to each test section and allowed to dry overnight. The instructions give baking times and temperatures to fully cure the paint, but the air supply hose in the COAL lab could not sustain the required temperatures. In addition, the un-insulated hose caused the air temperature to drop substantially before reaching the FCR. At higher upstream temperatures, the hoses started to melt. The recommendations section gives more information on the high temperature hose issue. Failure to bake the paint did not seem to affect performance in any way.



Figure 45: FLIR systems SC640

The FLIR® Systems IR camera shown in Figure 45 is the same camera used by Bohnert (17) and McCall (2). Appendix C covers operation of the camera and software. It is a portable unit, easily hand carried, and somewhat ruggedized. The manufacturer markets the camera for professional users in the home inspection, electrical, and other industries. Table 5 lists the specifications of the IR camera.

Table 5: P640 camera properties (17)

| | |
|--------------------------|---|
| Detector Type | Focal Plane Array (FPA) |
| Spectral Range | 7.5 to 13 μm |
| Resolution | 640 X 480 pixels |
| Temperature Range | -40 °C to 1500 °C Optional up to 2000 °C |
| Accuracy | ± 2 °C, $\pm 2\%$ of reading |
| Interfaces | Firewire, USB, IrDA, SD-card |

The camera distance from the window was approximately 10''. The distance is greater than McCall's to protect the camera from the high heat output of the FCR. In addition,

the camera was removed from the setup while not actively testing to avoid heat buildup. The cost of increasing the distance from the camera to the FCR is a loss of resolution around the coolant hole region.

For each IR test, the FCR was started, set to $\phi=1.5$, and the rig allowed to reach near steady-state conditions. Steady-state was defined as less than 2°C temperature change in the water coolant over 10 minutes. Once at steady state the water temperature data was recorded and the software commanded to start data acquisition. For each test case 10 seconds of data was recorded at 10 Hz (300 pictures total). The software then converted the data to a MATLAB® file format. A MATLAB® program (Appendix D) mapped the picture of the curved section to a 2-D plane and averaged the temperature values.

Recall from Equation 10 that the film cooling efficiency is defined as:

$$\eta_f = \frac{T_\infty - T_{aw}}{T_\infty - T_c}$$

For the efficiency to properly vary between 0.0 and 1.0, $T_{aw} = T_\infty$ when no cooling is present and $\eta_f = 0$. This condition means T_∞ for any pixel is the value of that pixel if no coolant was present. Similarly, for the perfectly cooled case $T_{aw} = T_c$, and $\eta_f = 1.0$. In the second case, the wall temperature is the coolant temperature. The camera is measuring the value of T_{aw} at each pixel location if that pixel is steady-state (adiabatic). If we assume the temperature of the each pixel is a function of the length from the burner, then T_∞ is obtained from an uncooled test section at the same streamwise location. Comparison of the water coolant temperature change ensures that the cooled and uncooled test cases are for the same conditions.

The coolant temperature at the hole exit, T_c , is the toughest variable to solve in this situation. McCall (2) found that measured temperature at the center of the hole equaled the coolant temperature obtained with thermocouples inside the cooling plenum. Without a cooling plenum like McCall, it is difficult to obtain the temperature due to the small tube area. Chapter 5 describes one possible method to determine the coolant temperature. This research used the temperature at the center of the coolant hole for the coolant temperature. Chapter 4 will discuss the results of this assumption.

With all three temperatures from Equation 10 known, η_f is also known at each pixel location. It is also possible to integrate in the manner of Equations 11 and 12 to obtain the spanwise and area-averaged efficiency.

3.4.2 Calorimetry

The calorimetry data from the FCR is a byproduct of the water cooling system. The water flows behind the entire test section, entering near the burner and departing near the nozzle. The maximum heating from the burner on the test section occurs somewhere downstream of burner, while the water temperature is increasing constantly as it moves across the test section. The total temperature change is the only recorded data, permitting an average heat flux measurement for the entire test section. Film cooling works by carrying heat away from the surface, and blocking heat from being transferred to the surface. As the cooling efficiency increases, the heat flux from the test section to the water coolant should decrease. It is also possible that the rejection of the heat by the film coolant causes another region to experience more heat. The six flat walls of the FCR originally included water cooling to capture the total heat flux.

The heat added to the water is shown in Equation 36.

$$\Delta Q = \dot{m}c_p\Delta T \quad (36)$$

where ΔQ is *heat added to the water*, \dot{m} is *water mass flow rate*, c_p is the *specific heat of the water*, and ΔT is *change in water temperature*. The heat flux is then the total heat divided by the interior area of the test section wall:

$$\Delta q = \frac{\Delta Q}{A} = \frac{2\Delta Q}{\pi r l} \quad (37)$$

where A is *test section area*, r is *test section radius*, and l is *test section length*. The decrease in heat flux will be very small due to a single coolant hole, but future testing may involve arrays of holes to implement full coverage film cooling. The change in heat flux due to the coolant hole reinforces the surface temperature measurement by the IR camera. It may also be useful when the combustion products obscure infrared measurement of the wall temperature.

IV. Analysis and Results

The objective of this thesis was to build and test a film-cooling rig for combustion environments in the AFIT COAL lab. The results generally fall in two categories: the build/modification results, and the test results with the completed rig. Chapter 3 discussed the design changes necessary to add combustion to the FCR, the new hardware required to support those modifications, and changes to the existing COAL lab hardware. This chapter focuses the final product of each thesis objective and actual operation of the FCR. Finally, the infrared thermography and calorimetry test validation of the FCR design are discussed.

4.1 Test Section Construction

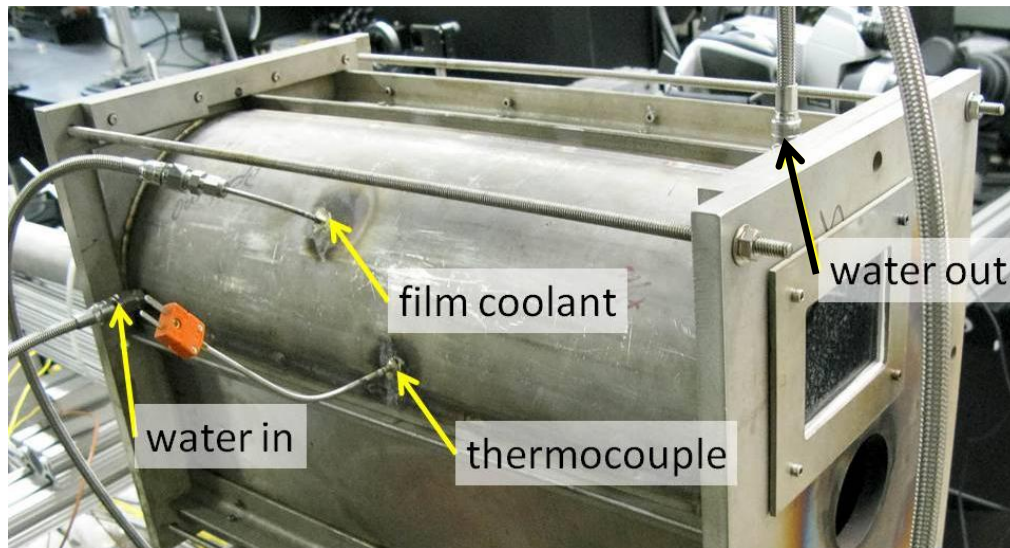


Figure 46: Final test section configuration

The final test section closely resembled the original design (Figure 46). Despite lacking any significant changes to the design, construction of the test sections required

the most time (and money) of any activity in this research. There are currently eight test articles. Two (one 4'' and one 6'') were welded and machined, but otherwise unfinished. The unfinished test section allowed development of the operating regime while production continued on the remaining articles. Two (one 4'' and one 6'') have coolant holes for 45° compound injection but do not have coolant tubes, thermocouples, and are not painted. The remaining four test sections (0° and 90° injection, 4'' and 6'' radius) were completed and used for testing.

The thermocouples in the stainless steel test sections were brazed into place as discussed in Chapter 3. Prior to brazing, each thermocouple was calibrated using the same technique as McCall (2). Each thermocouple measured the temperatures of an ice bath and boiling water, setting the calibration points for 0 °C and 100°C. The linear curve fit of the calibration points gives the true temperature for any thermocouple measurement. McCall's calibration showed his thermocouples did not have any bias error beyond the capability of the data acquisition system so calibration curves were not necessary. Figure 47 shows a portion of the calibration curve for one of the three thermocouples used in this research. The calibration yields a more accurate temperature measurement than simply using the manufacturer's published error range (shown by the error bars).

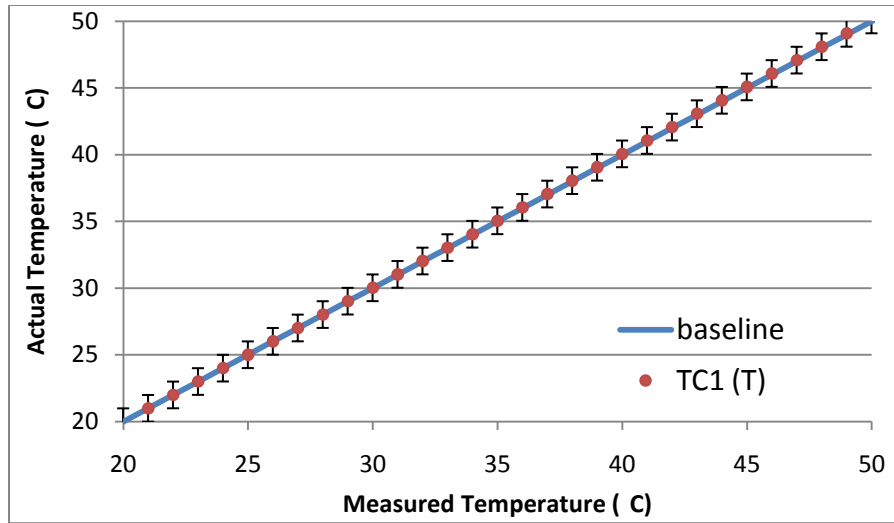


Figure 47: Thermocouple error (@20-50 °C). The baseline is where the measured temperature equals the actual temperature

At very high temperatures ($\sim 700^{\circ}\text{C}+$) the calibration curve may fall outside of the manufacturer data, in which case a better calibration method for high temperatures is required. For the temperature range expected in the FCR ($<300^{\circ}\text{C}$), every calibration curve fell inside the manufacturer's error range.

McCall (2) corrected the infrared temperature measurement by recording the infrared temperature of the thermocouple (at the tip) inside the FCR for each test. Each pixel was adjusted by the difference between the thermocouple and IR measured value. For example, if the thermocouple read 77°C , and the IR camera 83°C , then each pixel from the IR camera would be adjusted down 6°C in the same manner as McCall(2). The plan for this research was to use the same technique, minimizing bias error in the camera temperature measurement. The major benefit to this method is avoiding the requirement to find the emissivity, transmissivity, and all the other factors necessary to calibrate the

camera. Not only does each factor have a contribution to the overall error, but also some of the factors (atmospheric temperature) change dramatically over the path from the test section to the camera sensor. The camera settings are not complex enough to cover every possible test setup.

The first test section produced was a 6'' radius section. The AFIT machine shop brazed an "N" type thermocouple into the test section using the same technique as for the coolant tube, except the tip extended approximately 0.135'' into the test section (Figure 48).

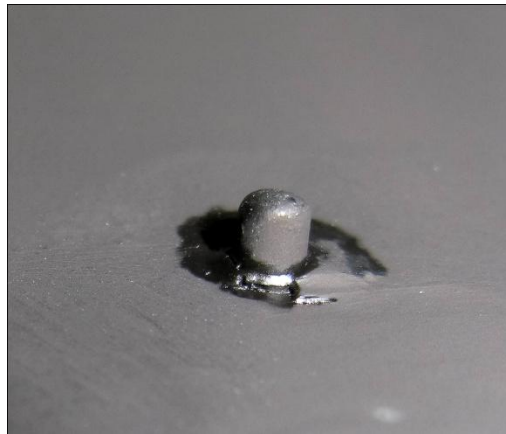


Figure 48: Thermocouple extending from test section

The "N" type thermocouple was chosen for its stability at high temperatures compared to the more common "K" type thermocouple. A handheld device displayed the thermocouple temperature during the brazing to ensure the thermocouple was not damaged by the high temperatures of the oxygen-acetylene torch. The maximum temperature displayed during brazing was 322°C, well below the maximum temperature rating (1300°C). The tip of the thermocouple was glowing bright red in the direct flame

of the brazing torch. The actual temperature was estimated using the color of the glowing metal. For 316 stainless steel (with a similar melting point as the thermocouple sheath), the color indicated a temperature well above 500°C (29). The thermocouple is therefore not reading the temperature at the tip of the sheath (the surface temperature), but rather it is reading some average temperature of the test section wall. Testing inside the FCR verified the same result.

With the IR camera temperature calibration by thermocouple in question, the remaining option was to use the internal camera calibration settings. Chapter 3 covered the drawbacks to using the internal camera settings. Without a better method of determining the temperature bias, the calculated efficiency values only allow qualitative conclusions regarding the cooling efficiency.

4.2 Final Burner Design

After much iteration, the final burner design was a turbulent pre-mixed propane-air flame. The mostly fuel-rich operating range of the burner resulted in a pre-mixed inner flame surrounded by a diffusion flame. The excess fuel in the mixture reacting with the room air created the diffusion flame. Figure 49 shows the diffusion flame growing with the equivalence ratio.

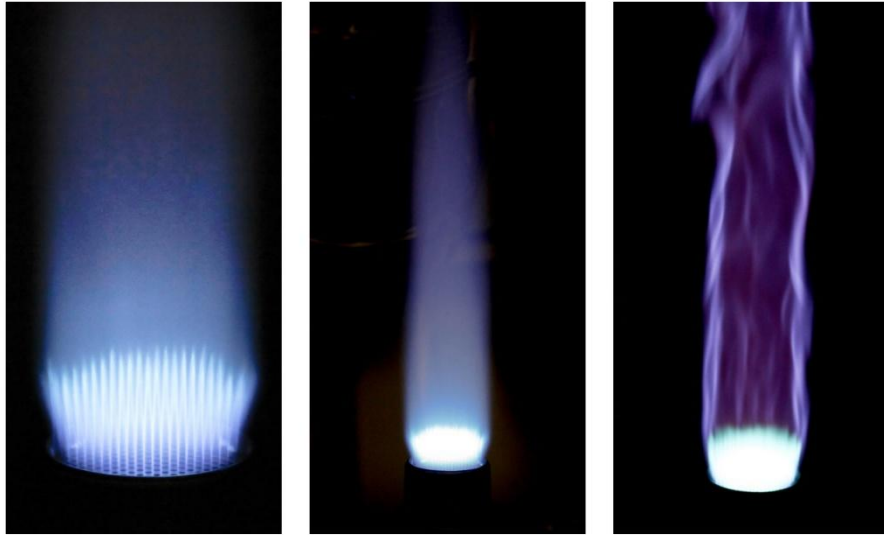


Figure 49: Burner flame in open air, ϕ increasing left (0.9) to right (1.5)

If the FCR were perfectly sealed, only the pre-mixed flame would exist inside the rig, while the diffusion flame would exist outside of the rig. The unsealed wall joints allowed room air to create a small diffusion flame inside the rig. The air supply was limited enough to force a diffusion flame at the exit of the FCR, as expected of a sealed box.

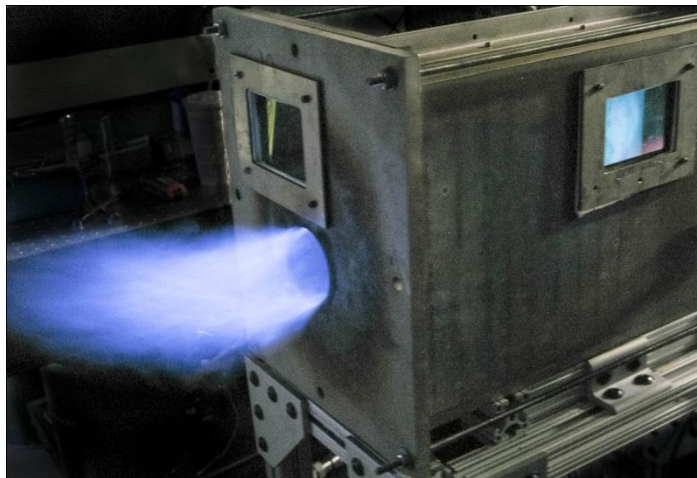


Figure 50: Diffusion flame at FCR exit

The velocity of the gas through the burner limits the low end of the operating range. The flame base constricts as the airflow increases, probably due to boundary layer growth inside the mixing pipe. As the boundary layer grows, the air mass must pass through a smaller effective passage, increasing its velocity further. Eventually the flame detaches from the burner and either extinguishes or attaches to the nozzle. This in turn forces the velocity of the air in the middle of the pipe to increase in order to maintain the same mass flow rate. Figure 51 shows the burner flame narrowing at the base due to the boundary layer effect.



Figure 51: Burner flame at $\phi = 0.90$

One possible research area for the FCR is relating the equivalence ratio to cooling effectiveness. Lean main flows combined with a fuel coolant may behave very differently than rich main flows. Calibrating the air and propane flows is important to determining the true equivalence ratio. The propane calibration used a BIOS Definer 220, shown in Figure 52.



Figure 52: BIOS definer 220 used for MFC calibration

The maximum flow rate for the BIOS 220 is 30 SLPM, enough to calibrate through the entire range of propane flows (< 20 SLPM), though far too little to calibrate the airflow. The scaling control knob on the type 247 mass flow control panel was adjusted until the display matched the measurement on the BIOS. The limiting factor for the propane mass flow errors is then the readout of the control panel. For the main propane flow, using a 50 SLPM (N₂) MFC, the controller reads to one tenth of a SLPM. The bias error is then ± 0.05 SLPM. The random error was not obtained because the MFC control panel is not currently configured to output the signal to LabVIEW®. The propane coolant flow was calibrated in a similar manner, except the 100 sccm (Xe) MFC reads to 0.1 sccm, resulting in bias error of 0.05 sccm. The relative error is the reading error divided by the displayed value.

The main flow air was not calibrated in the same manner because the flow rate far exceeds the capability of the BIOS. The manufacturer's published error range for the Fox MFC is 0.1% of the reading. The main and secondary mass flow controllers in the

COAL lab have not been calibrated since installation. Without an adequate calibration device, it is difficult to determine the bias error, but the random error was obtained using the signal input to LabVIEW®. It is first important to note the airflow overshoots the intended value when changed. The airflow was allowed to settle before taking any data for this research. Figure 53 shows the airflow settling after changing the setting from 0 kg/min to 0.25 kg/min (the startup setting). Minimizing the input changes reduced the overshoot.

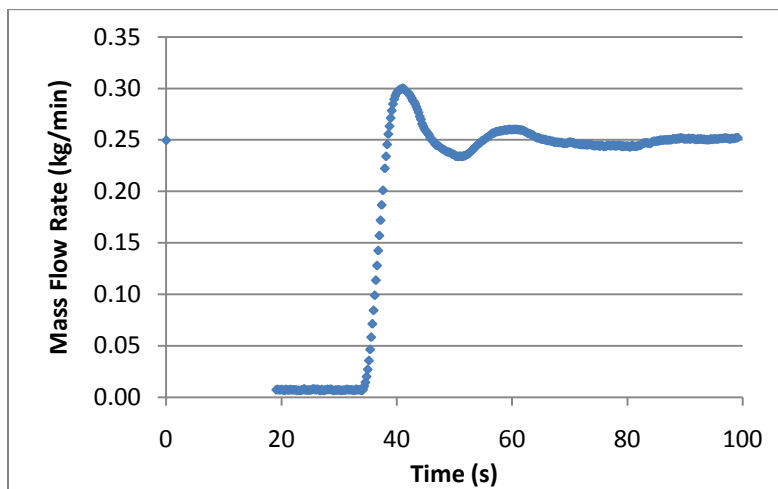


Figure 53: Air flow overshoot and settling when changing flow rate

The airflow oscillates even without the setting changing. Figure 54 shows a three-minute window of the airflow, 10 minutes after the previous setting change.

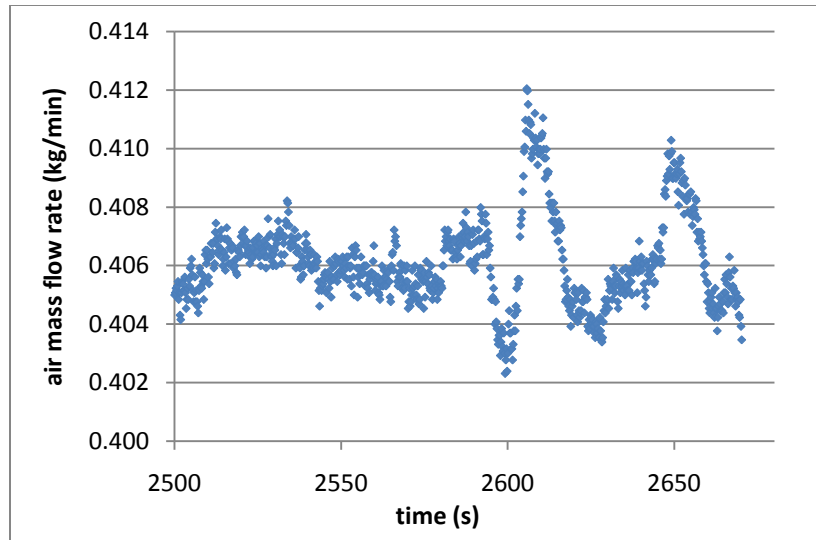


Figure 54: Air flow oscillation at 0.4067 kg/min setting

The airflow was recorded at a sampling rate of approximately 5 Hz for 10 seconds.

Figure 55 shows a typical 10 second airflow sample, where the set point was 0.4067 kg/min ($\phi = 1.5$ for 20 SLPM of C_3H_8).

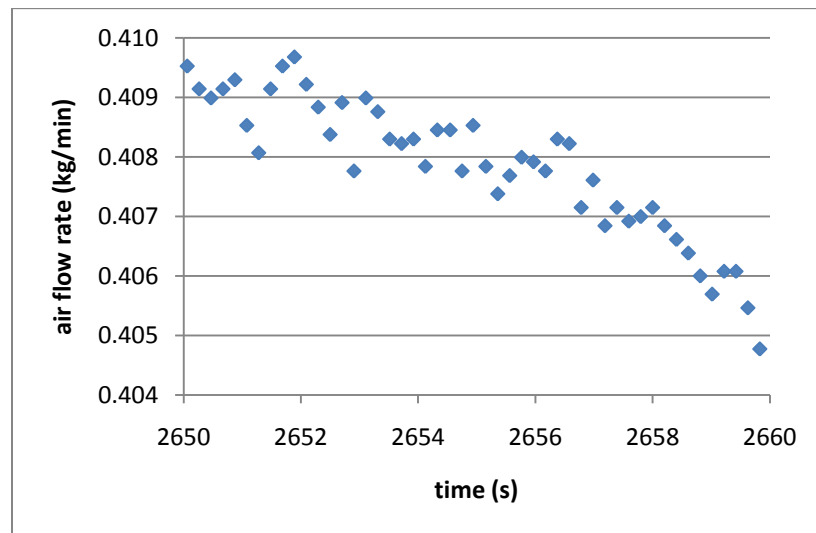


Figure 55: Air flow during test window

The mean flow rate is 0.4078 kg/min with 95% confidence that the true mean is $\pm 0.0817\%$. The relative error in the equivalence ratio is then the sum of the relative errors of the propane (0.0025 for 20 SLPM) and the air (0.000817). In this example, the error in the calculated equivalence ratio ($\phi = 1.5$) is 0.33, or $\phi = 1.5 \pm 0.005$.

4.3 Heat Flux Experiment Design

Implementing the water cooling/heat flux measurement system was one of the first tasks of this research. Chapter 3 described the water cooling system and the method used to seal each wall. Once the burner and test sections were ready, the entire FCR was assembled and run. This section describes the results of the heat flux system testing in the full FCR and the modifications that resulted.

The testing of the complete heat flux system began with the water flow to each wall of the FCR set at 10 gph, half the amount tested in the stand-alone panels. No leakage was immediately apparent, although once the flow increased to 12 gph some small leaks appeared in multiple panels. This was a much lower flow rate than previous successful testing. The two main factors in the leakage were probably the orientation of the panels and the stresses introduced when the panels were connected.

During stand-alone testing, each panel rested horizontally on the test bench with the inner wall on bottom and the outer wall on top. Only the top panel orientation matched the test configuration once the FCR was constructed. The four sidewalls sat on their long end, while the bottom wall was upside down (the outer wall was on bottom) and supported by a 1 1/2" aluminum T-slot frame. In this orientation, the weight of the

water inside the panel presses against the outer wall and the weight of outer wall does not hold it against the inner wall and gasket.

The second cause of the leakage was the connection between panels. The stainless steel construction made the weight of each panel significant. With the panels connected together, the weight was focused at the joints, instead of distributed across the inner wall in the stand-alone testing. The result was some bending and twisting of the panels once assembled.

Together, these two factors limited the maximum water flow to 10 gph in the assembled FCR. Once heat was added however, even 10 gph caused sustained leakage. As the rig temperature increased, the leakage increased. As water leaked from the sidewalls it seeped into the cracks between the walls and then into the rig, contaminating the flame. In addition, the seals around the windows leaked profusely, clouding the windows with mineral deposits (from the hard water). The changes necessary to implement this water cooling/heat flux measurement system would require almost an entire rebuild of the FCR. Rebuilding the FCR was not an option, so testing began without any water cooling.

The existing two-piece walls could not withstand the heat output of the burner. There were once again two contributing factors. First, each inner wall was machined from 1/2" thick 316 stainless steel. The outer wall was 1/8" thick 316 stainless steel. 1/8" was removed from the inner wall to hold the outer wall. Another 1/4" was removed to form the coolant channel. Only 1/8" of material remained for most the side wall area. Such a small amount of material could not conduct heat from the hot regions

to the cooler regions fast enough to avoid damage. Figure 56 shows the inner wall construction.

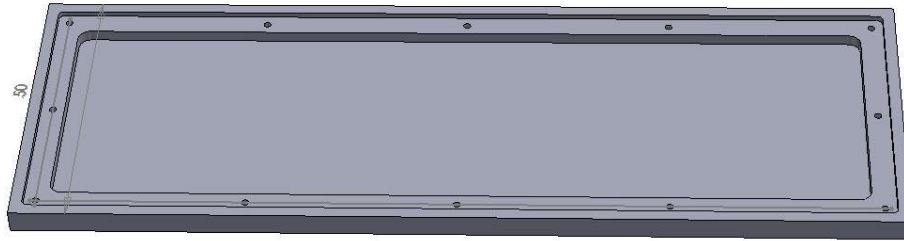


Figure 56: CAD drawing of walls for water cooling

The exit wall was the hottest section because the burner flame directly impinged on the inner wall and the outer flame attached to the exit nozzle. The window side wall and top wall also began to glow red-hot during relatively short test runs. Figure 57 shows the dramatic red glow from the exit panel, indicating temperatures over 800°C (1500 °F).

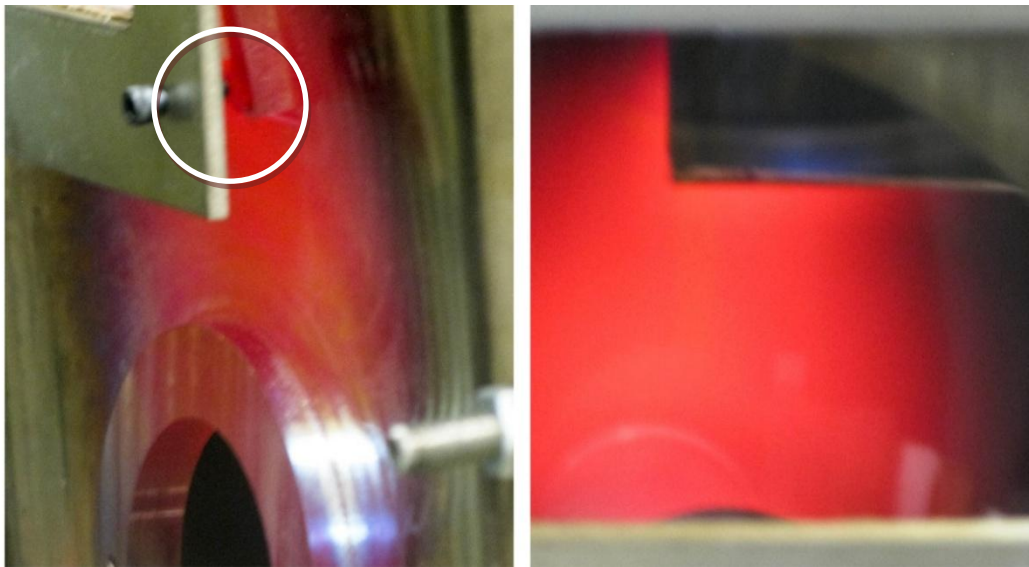


Figure 57: Inner (right) and outer (left) view of red-hot exit panel

The exit panel also warped inward (see the circled region of Figure 57). Eventually the screws holding the exit panel window frame popped out of the panel. The second contributing factor to the failure of the hollow walls was that without fluid movement through the cooling channels, the air inside the channel insulates the inner panel so the heat cannot radiate to the surrounding environment. Removing the outer panels could mitigate this effect, but it introduces a completely new set of design challenges and still fails to solve the problem (the wall in Figure 57 did not have the outer wall attached).

The only remaining option was to rebuild the walls. Time constraints prevented construction of improved water-cooled walls, but simple 1/2'' thick solid walls required much less effort by the machine shop. The exit and the window sidewalls were the main priorities because they showed the highest heating during the test run. New solid top and small side walls for the 4'' test sections were also constructed, as McCall's (2) walls were incorrectly sized. The original bottom, inlet, and small sidewalls for the 6'' section remained, with no adverse effects. Figure 58 shows an old (hollow) and a new (solid) sidewall.



Figure 58: Solid (top) and hollow (bottom) small side walls for the 4'' test section

The schedule savings are a result of not requiring milling of the cooling channel, manufacture of the outer wall, or drilling and tapping the numerous screw holes. The original walls took a few days each to complete while multiple solid walls took only in a few hours. Test runs with the solid walls showed no signs of warping; glowing due to elevated temperatures was limited to small regions around the exit nozzle (Figure 59).

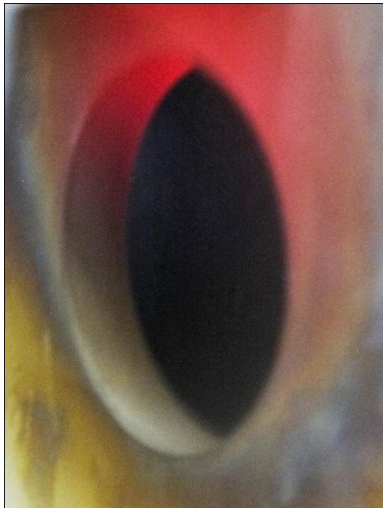


Figure 59: Solid exit wall nozzle

The drawback to using solid walls was losing the ability to measure the total heat flux on the FCR. This was acceptable because any changes in the heat flux are most pronounced on the test section with the coolant hole. Film cooling prevents heat from reaching the wall, possibly causing increased heat flux to un-cooled regions. In this experiment, with a single coolant hole, any change in heat flux to the un-cooled panels would most likely be lost in the noise of the total heat flux.

In addition to simplifying the walls, abandoning water-cooling for the side panels simplified the water manifold setup. Figure 60 shows the new manifold setup.

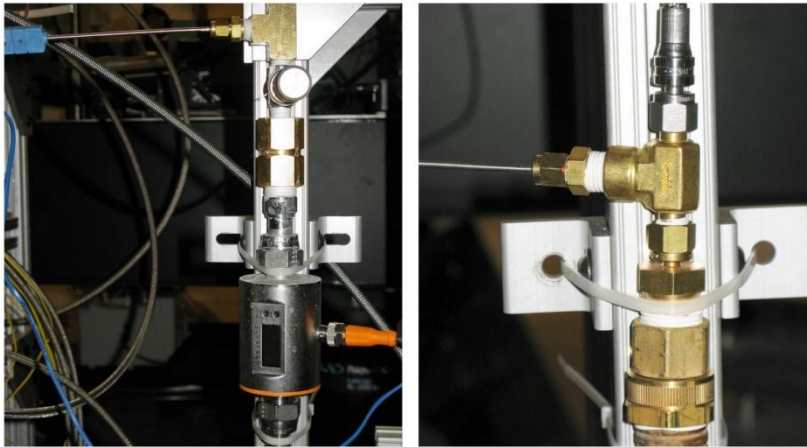


Figure 60: New inlet (left) and outlet (right) water-cooling manifolds

With water only flowing to the test section, the new manifolds are not actually manifolds at all. The terminology remains the same because they perform the same functions as the original manifolds: measuring temperatures and flow rate. Future FCR designs may incorporate the original manifolds.

The water flow rate to the test section was constant throughout the experiment. A flow rate of 10 gph allowed an adequate temperature change without boiling. The

polyethylene tubing started to leak at the connection to the test section so stainless steel tubing replaced it with no sign of leakage.

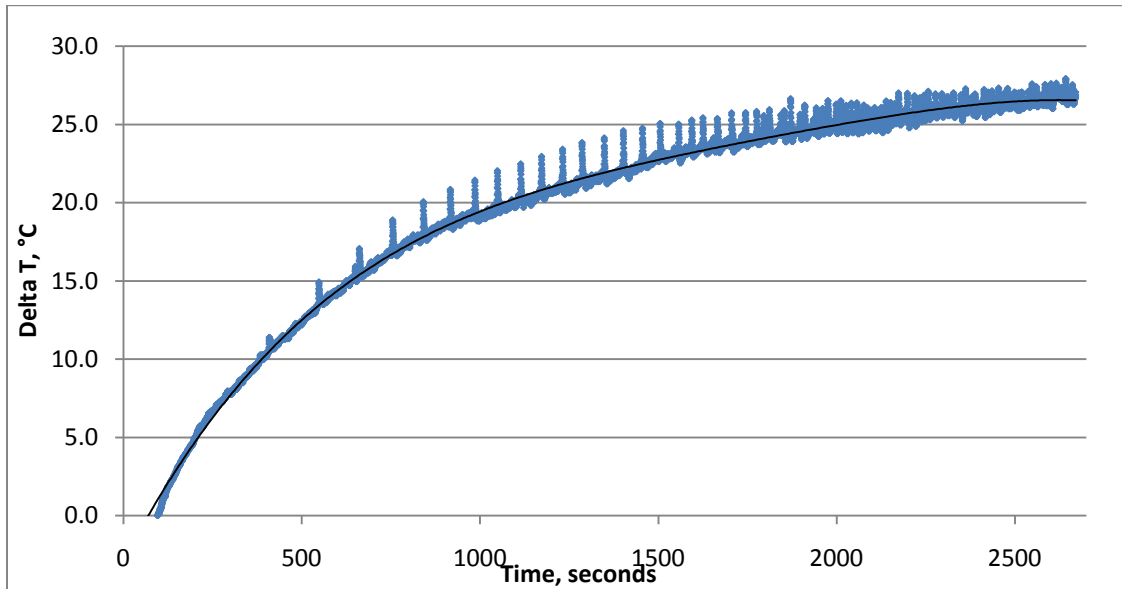


Figure 61: Water temperature change for complete test

Figure 61 shows the change in water temperature for one test run (measured at the inlet and outlet manifolds). The data collection occurred at the end of the run (from $t = 2650$ - 2660 s). It is unknown why the temperature periodically spiked, or why there was so much variation in the data at the end of the test. The temperature spikes and noise did not correspond to simultaneous changes in the air or water flow rates.

After the water temperature reached steady state, the IR camera and water temperature values were recorded near-simultaneously⁵ for 10 seconds. Figure 62 shows the change in water temperature during data collection for one test run.

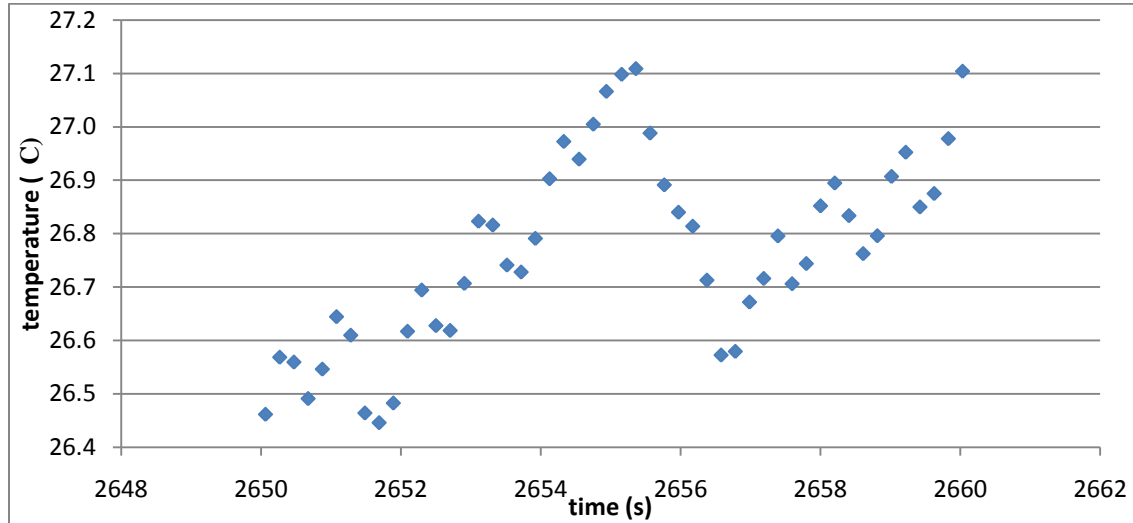


Figure 62: Water temperature change during IR data collection

The mean temperature change in this example was 26.77 °C, with a 95% confidence that the true mean is $26.77^{\circ}\text{C} \pm 0.19\%$. The thermocouples were calibrated using the technique described earlier. LabVIEW® simultaneously collected the water flow rates as shown in Figure 63

⁵ The test operator starts the camera recording by pressing F5 on the camera control computer and then presses a button in LabVIEW to start the water temperature, water flow, and airflow recording. A fraction of a second elapses between the two events.

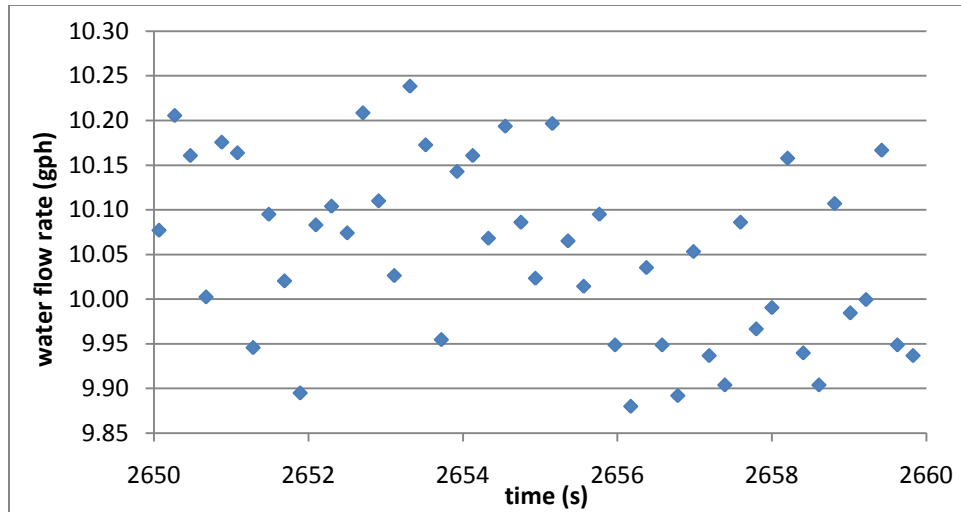


Figure 63: Water flow rate during data collection

The mean water flow rate was 10.05 gph with a 95% confidence that the true mean is $\pm 0.27\%$.

4.4 Infrared and Heat Flux Test Results

FCR cooling performance was validated using IR testing, in the same manner as McCall (2). Once the test sections were complete and the operating range known, data collection began. This section describes the various configurations of the FCR tested while attempting to obtain meaningful film cooling data. Thirteen conditions were tested with none showing the desired film cooling.

The baseline configuration utilized the 4'' radius test section, 0° compound injection angle, 1.5 blowing ratio, and 1.5 equivalence ratio. The propane main flow was near 100% (20 SLPM), with the air flow and the propane coolant settings based on the blowing and equivalence ratios. The water-coolant flow rate was 10 gph. Figure 64

shows the coolant hole region for one time step. The temperature color range was optimized to show the coolant hole.

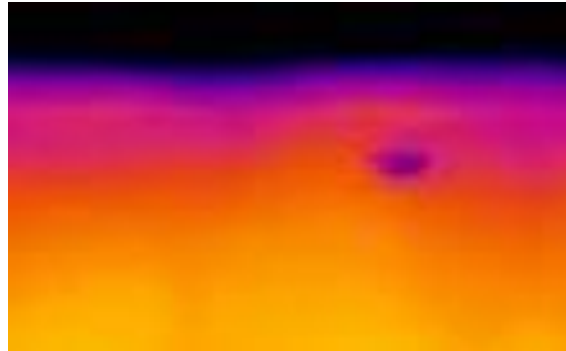


Figure 64: IR camera view of cooling hole ($BR = 1.5$). Main flow from right to left.

The dark region at the top of the picture is a result of the test section curving toward the camera. The coolant hole is actually near the middle of the curve, but it appears at the top when viewed from the camera. The wall of the coolant tube is barely visible, and the brazing has not affected the wall temperature in the region of the cooling hole. The temperature is the hottest at the bottom of the picture (for Figures 64-66, and 70), closer to the burner flame.

Initially, two issues arose. First, the temperature fluctuated rapidly across the test section from frame to frame. It is unlikely the metal is changing temperature at that speed, but rather the combustion products are either emitting or absorbing infrared energy as they pass between the window and the wall. This issue will be discussed in more detail later.

The second problem is the lack of any trace of film cooling on the test section wall. Figure 65 shows the coolant hole region after the curve was flattened and the 300 pictures averaged in MATLAB®.

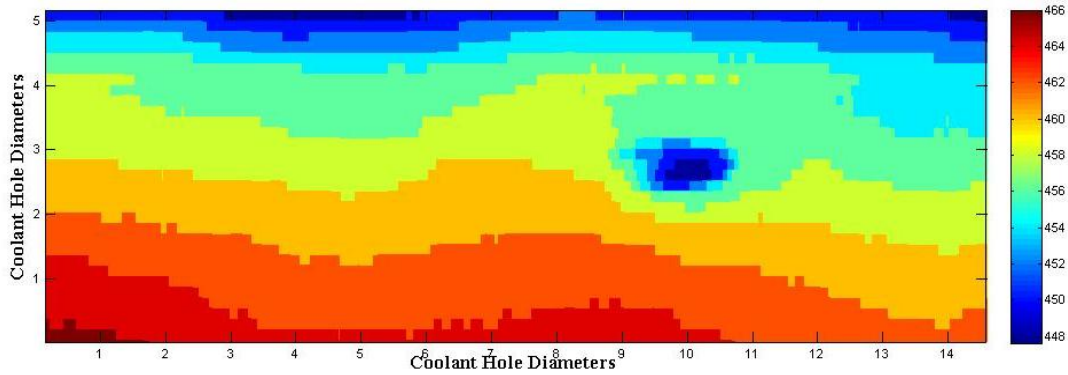


Figure 65: MATLAB® Averaged temperatures, 0° injection, BR = 1.5 (temperature in Kelvin). Main flow from right to left.

The hole is visible and cooler than the surrounding material, but the typical cooling tail streaming from the hole is not evident. Without any downstream effect, the cooling effectiveness is not measureable.

The 90° compound injection was tested next, because it previously showed better cooling effectiveness. In addition, the 90° orientation blows coolant down onto the test section in the region more closely perpendicular to the camera. The MATLAB® code interpolates the camera data to *stretch* the top region, meaning the pixel size is greater at the top than the bottom (less fidelity at top). Despite these two advantages of the 90° test section, multiple test runs demonstrated no cooling effect for this configuration either.

The 6'' test section has the same benefits as the 90° injection: better expected cooling efficiency and better wall visibility for the camera. The expectation was for the

larger radius to allow the coolant to spread more than the tighter radius, although the length of the coolant stream may decrease. Testing showed no cooling effect for the 6'' test section.

The blowing ratio has a direct effect on the cooling effectiveness, so it was varied in an attempt to collect data. First, the test range of 0.5 to 1.5 was attempted, with no results. Next, the blowing ratio was decreased to 0.1, in case the main flow velocity was too low to turn the coolant flow, and the coolant was jetting out into the main flow. Again, no cooling was visible. Figure 66 shows the 0.5 blowing ratio test with no evidence of film cooling and a similar temperature pattern as the 1.5 blowing ratio test (Figure 65).

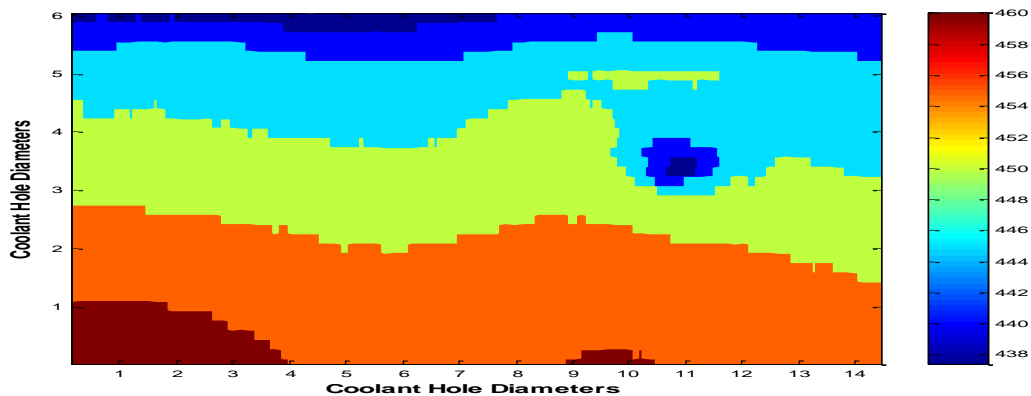


Figure 66: 0° injection, BR = 0.5 (temperature in Kelvin). Main flow from right to left.

Finally, a five SLPM (N2) MFC was installed (50X larger), allowing orders of magnitude greater blowing ratios. No cooling was observed for blowing ratios of 15 or 150. To verify propane was actually reaching the test section, the propane line was tested

in open air. Figure 67 shows the propane flame using the original 100 sccm (Xe) MFC at 100%, equivalent to a blowing ratio of 2.24 for the baseline configuration.

Figure 67 shows just how little propane is flowing through the coolant line. The tube in the figure is the same size as the coolant tube (0.125") and the flame is approximately twice that height (~0.25").

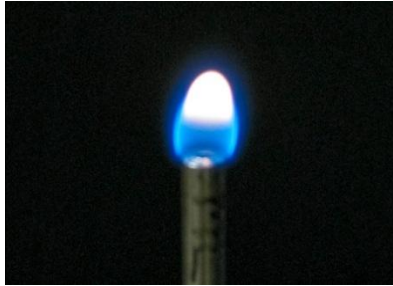


Figure 67: Propane flame from coolant line

The coolant flow was also tested inside the FCR, using the larger MFC and the coolant flow for an ostensible blowing ratio of 150. Figure 68 shows the resulting flame from the propane coolant.



Figure 68: Coolant flow combustion inside the FCR (exit wall removed)

The FCR was started with the exit wall removed to allow observation of the coolant flame in the presence of the main flow. It was clear the main flow was not spreading adequately to force flow across the wall. In this configuration, the coolant flame swirled chaotically, often upstream toward the inlet wall of the FCR. The fuel rich main flame sucking air in from the room may have caused this flow characteristic. This test proved that coolant was reaching the interior of the FCR, but it cast serious doubt on the main flow across the wall.

The equivalence ratio was also varied through the range of operating conditions ($0.9 \leq \phi \leq 1.5$). Decreasing the equivalence ratio (increasing the main air flow rate) meant more fuel was combusting inside the FCR. More combustion meant more H_2O and less C_3H_8 inside the FCR. Changing the equivalence ratio did not decrease the temperature fluctuations due to the combustion products. Film coolant effects were not visible at any equivalence ratio.

With the full range of normal operating conditions exhausted and no apparent cooling flow, testing of new configurations and operating conditions ensued. The primary motivation was getting adequate main flow across the wall. The first option replaced the nozzle end of the FCR with the stainless steel frame shown in Figure 69.

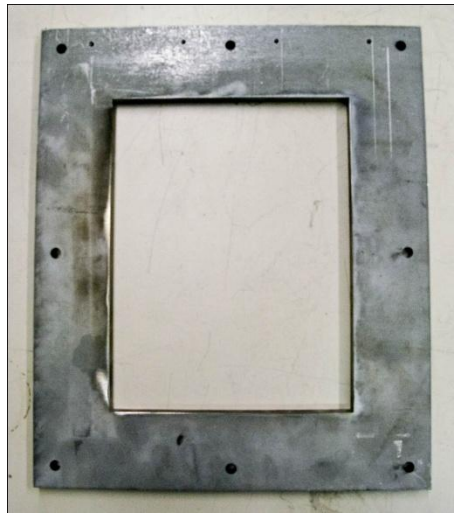


Figure 69: Open exit wall

This variation attempted to minimize any turbulence caused by the flow impinging on the exit wall and then wrapping around to the nozzle. The drawback to this design was room air interacting with the main flow inside the FCR, creating an unknown equivalence ratio at the coolant hole. A diffusion flame starting at the end of the pre-mixed flame and extended out of the FCR. Despite the larger exit area, the main flow did not spread to the wall and the IR camera did not show film cooling near the coolant hole. Figure 70 shows the open end test case.

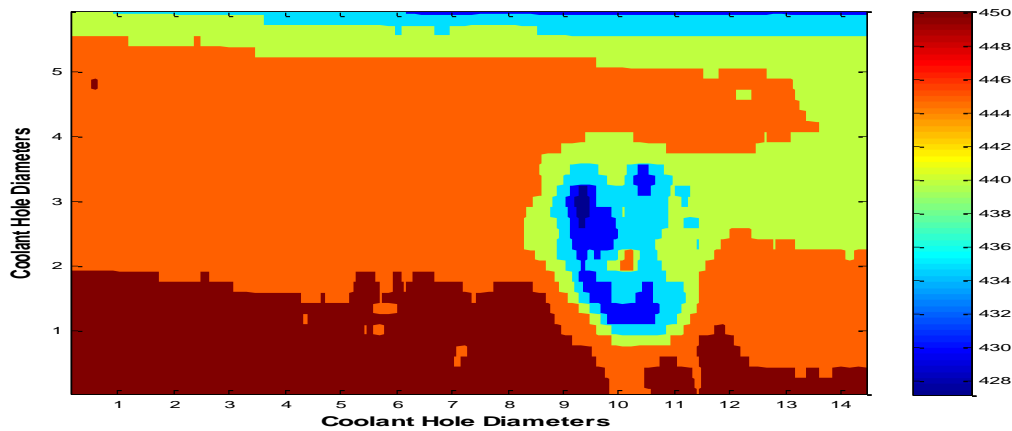


Figure 70: 90° injection, BR 1.5, open end (temperature in Kelvin)

The coolant hole does not appear clearly as in the previous pictures for two reasons. First, the braze attempt is much rougher in this test section. Second, there was a slight leak from the coolant hole, resulting in calcium carbonate build up below the hole. The leak was remedied as previously described, but minerals from the leak appear as hot spots in the IR pictures.

Another attempt utilized a wedge insert, used by McCall (2) for pressure gradient testing, to direct the flow up toward the test section wall. The apex of the wedge sat just before the coolant hole in the streamwise direction and out of view of the camera. The burner flame directly impinged on the wedge, heating it to over 800 °C; a wave of flame was visible over the top of the wedge near the coolant hole. Once again, there was no trace of coolant flow on the wall.

The next attempt addressed the possibility of the film coolant temperature rising before reaching the test section wall, therefore not cooling the wall. Without a thermocouple in the coolant line, it is difficult to correctly assess the coolant temperature,

as previously discussed. One possible solution was increasing the water flow to lower temperatures surrounding the coolant line and lower the wall temperature. Once again, no film cooling was visible using a 30 gph (3X) water coolant flow.

In another attempt to address the temperature variations of the combustion products, the rig was tested using only hot air in the main flow. Figure 71 shows the temperature variation for a single pixel, both with and without combustion. The error for the combustion case was 0.093% (0.43°K) while the error for the non-combustion case was 0.023% (0.093°K). The temperature error in the combustion case was nearly 4X greater than the non-combustion case. Despite the obvious difference in temperature fluctuation for the combustion case, the large sample size yields a very small error and makes infrared thermography a viable option for both conditions.

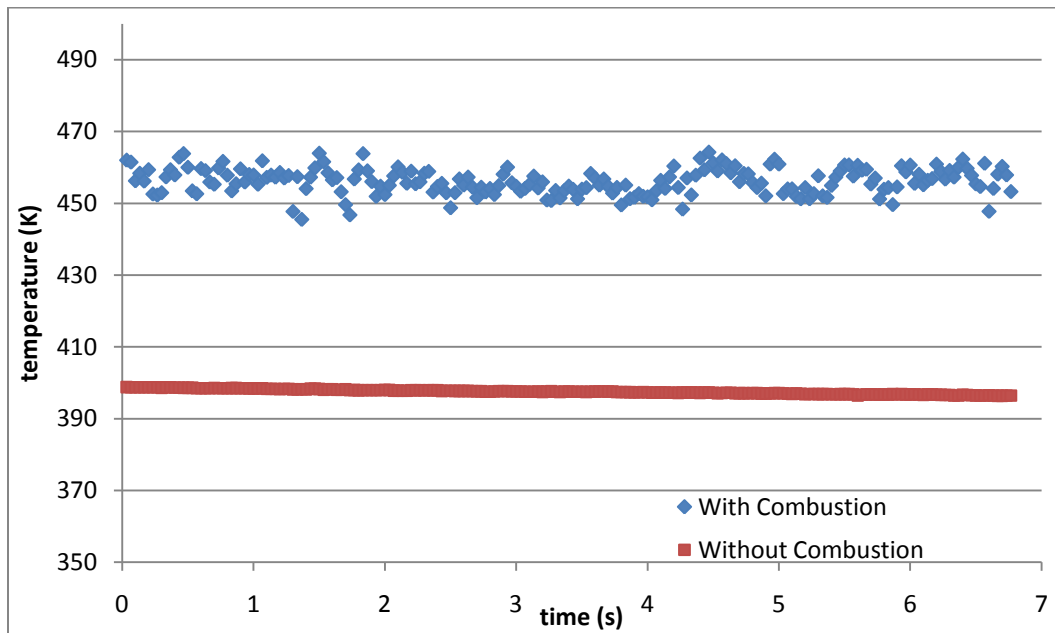


Figure 71: Wall temperature variation for a single pixel, with and without combustion

In the no combustion test, the air temperature was set to 600°F in LabVIEW®, with the temperature at the burner exit considerably less. Heat is lost from the poorly insulated pipes running from the heater to the test stand, from the uninsulated hoses running to the burner, and from the 18'' burner mixing tube. The burner is not equipped with thermocouples to measure incoming or outgoing gas temperatures. Once again, no coolant flow was observed on the wall. Varying the coolant flow from 0% to 100% did result in the temperature inside the hole decreasing, the first notable effect of cooling inside the FCR. This test further reinforced the assumption that inadequate main flow velocity along the test section wall was causing the coolant flow to jet into the main flow without adhering to the wall.

All attempts to capture film cooling along the test section wall were unsuccessful. The single largest factor was a lack of main flow velocity along the test section wall. The temperature variation caused by the combustion products was statistically insignificant with a sample size of 300. Thirteen different configurations were tested in the attempt to demonstrate film cooling with many more minor variations not described above. Chapter 5 will discuss the viability of the FCR for combustion testing of film cooling and also gives recommendations for future testing.

V. Conclusions and Recommendations

5.1 Conclusions of Research

This research has shown that the FCR is not viable for film cooling research in its current configuration using gaseous coolants. Despite successfully completing three of the four primary objectives, basic design flaws prevent combustion-based film cooling research in the FCR. The four research objectives are reviewed next, followed by recommendations for future modifications, and future research.

5.1.1 Curved Test Section Design and Build

The previous researcher left behind a clear design for the stainless steel test sections. The only undefined features were the coolant tube and the instrumentation (thermocouples). The combustion environment and stainless steel construction complicated both features, but the most significant challenge was actually building the test sections themselves. The pitfall in a complicated component design is that it does not allow rapid prototyping, testing, and redesign. In this case, only one attempt was possible, and even that was a challenge. Brazing the coolant tubes was effective at delivering gas coolant to the test section wall, although brazing required both skill and practice to accomplish effectively. The thermocouple did not read the surface temperature as intended. The camera software settings were an acceptable means of obtaining the test section temperature only because the cooling efficiency equation relies only on temperature difference and not absolute values. Even had cooling flow been obtained, this limitation represented a significant weakness in the FCR design. The

recommendations section discusses changes to simplify the test section design and possible temperature calibration methods.

5.1.2 Burner Design and Build

Starting only with a 1/4'' hole tapped into the inlet wall of the FCR and no burner plans, this research designed, built, and tested a 2'' premixed burner capable of operation from $0.9 \leq \phi \leq 2.0+$. A co-axial design was originally designed and built, but open air testing proved that it was not viable without significant additional design effort. A coaxial design is preferable due to its use in actual rocket engines, but the pre-mixed burner was simple, stable, and provided the heat and combustion products necessary for this research. The flame from the 2'' burner did not adequately spread and provide the hot combustion flow along the test section as intended. The main flow characteristic is critical to film cooling research so this flaw prevented collection of cooling data. The recommendations section will describe in detail changes to resolve the main flow issue.

5.1.3 Heat Flux System Design and Build

This research successfully implemented a heat flux measurement system for the curved test section of the FCR, but failed to demonstrate total heat flux measurement for the FCR. The heat flux system measured the volumetric flow rate and temperature change of water flowing over the known area of the test section. LabVIEW® sampled and recorded these measurements to allow calculation of the average heat flux to the test section wall. The inability of the FCR to produce film cooling on the test section wall prevented demonstration of cooling with the heat flux system. For a single coolant hole in a large test section, the water temperature change due to the film coolant may be lost in

the signal noise. The recommendations section discusses changes to heat flux measurement to allow total heat flux measurement, as originally designed for the FCR.

5.1.4 Operating Regime Design and Test

With the test sections, burner, and heat flux measurement system complete, FCR operation was demonstrated using the existing COAL lab fuel, air, and control systems. Simple modifications allowed direct connection of the ethylene/air torch previously designed for the UCC. The starting conditions for the torch and main burner were found, as well as the operating range for the FCR with propane/air combustion. Coolant mass flows equivalent to a blowing ratio range of 0.5 to 1.5 were demonstrated, although lacking the corresponding film cooling effects due to the coolant jetting into the main flow. The failure of the coolant to turn and adhere to the wall is due to inadequate main flow velocity, as previously discussed.

The next section gives recommendations for the issues discussed here as well as other issues. With these recommendations, the AFIT COAL laboratory is ready to continue film and effusion cooling research for rocket engine applications. Despite the lack of measureable data, this research leaves behind a significant amount of knowledge and lessons learned for future projects.

5.2 Recommendations

Due to inadequacy of the current FCR design, it is appropriate to include a detailed list of recommendations for future researchers. The first section covers recommendations for modification to the current FCR. These recommendations are intended to correct the main flow velocity, allow measurement of the total heat flux, and

generally improve the characterization of the operating environment. The second section discusses a new FCR design that addresses many of the issues with the current design.

5.2.1 Recommendations to Improve the Current FCR

Correcting the main flow velocity along the test section wall must be the main concern for any future research involving the FCR. This correction may be accomplished by moving the location of the burner much closer to the test section wall, or changing the design of the burner so that it incorporates more of the area of the inlet wall.

If the existing burner design is moved closer to the test section wall, then the main flow combustion gases will travel along the wall, forcing the coolant to turn and cool the wall. One drawback to moving the burner location is the laser diagnostics access window location. The window is situated between the burner and test section. The current window is 3''X4'', much larger than necessary to study the coolant effects along the wall. For laser diagnostics of the film coolant region alone, a much smaller window is suggested. The inlet wall must be rebuilt to incorporate these changes.

Another possibility is rebuilding the entire inlet wall to incorporate a burner over most of the wall area. This more closely resembles a rocket engine combustion chamber where the inlet end of the chamber mostly consists of fuel and oxidizer injectors. If possible, the new burner design should include impinging air and fuel jets, resulting in a diffusion flame inside the FCR. This change would also bring the FCR more in line with actual engine design, but would require additional effort to design the injection angles, flow rates and hole spacing. Fabrication issues with such an assembly would also add to the design challenge.

Once the new burner is built, the flow velocity should be tested inside the FCR (along the test section wall) using hot wire anemometry or PIV. The fragile hot wire anemometry instruments would probably not survive the combustion environment so hot air could be substituted for combustion gases to complete the test. The current LabVIEW® readout for the air temperatures does not reflect the true temperature of the air at the input to the FCR, so type “T” thermocouples should be added at the junction of the air/fuel lines to the burner and at the end of the burner. High temperature stainless steel hosing should be used to connect to the air supply and it should be insulated as much as practical. Flow velocity testing could be accomplished using the existing test section walls.

The basic test section design is sound, while some changes may improve the data. First, omitting the cooling channel will greatly simplify construction of the test sections. The value of the heat flux data is much less than the infrared surface temperature data or the laser diagnostic data and removing it solves a number of problems. Without a cooling channel, it is possible to implement some kind of cooling plenum in the manner previously described by McCall (2). A cooling plenum simplifies manufacture of the coolant hole, eliminating the need for a coolant tube or brazing while a single wall can be machined using traditional mechanical tools and not the EDM used for this research. The plenum may also allow direct measurement of the cooling flow close to the injection point.

Another change to the test section should be moving the coolant hole. First, the hole should be located so the wall near the hole is as close to perpendicular to the camera

as possible. The resulting hole will be near the bottom of the test section, and should be oriented so the coolant flows up the wall when there is compound injection. The hole should also be moved toward the exit end of the FCR. Moving the hole should result in a thicker boundary layer, improving the cooling results. Moving the hole location will require rebuilding of the large side wall, although the test sections could be reused. The new wall could incorporate the current 5'' ZnSe window, or a new window could be ordered in the current size (3'' X 4'').

Finally, thermocouple calibration is preferable to relying on the camera settings for absolute temperature measurement. This research used sheathed, ungrounded thermocouples. Sheathed-grounded, sheathed-exposed, and bare wire thermocouples should be tested. The thermocouples may not need to be brazed into the section to calibrate the camera readings. The thermocouple could be independent of the test section, but close enough to be in focus when viewing the test section wall.

One change related neither directly to the test section or the burner is the addition of a gasket or other seal to every wall joint in the FCR. The diffusion flame inside the current FCR resulted from sucking outside air into the rig. At times, a flame could even be seen at the corner of the large side wall and the exit wall. Any gasket must be capable of surviving the intense heat environment. The Fiberfrax® currently employed to seal the windows may be adequate, but it may alter the fit enough to require rebuilding of every wall. Properly seating the gasket on every joint will be difficult, and greatly complicates changing out test sections.

In general, further heat flux data collection is not recommended for the reasons already mentioned. Should the heat flux data be necessary to support the IR data then the current design may serve as a starting point. Leakage in the FCR walls prevented water cooling from being included. This leakage effect could be overcome by properly designing the inner walls and inserts. The lip where the screws attach the two walls and where the other wall rests should be at least 0.5'' (preferably 1''). This width allows RTV gasket material to seal the two surfaces together without leaking. The screw holes should be no more than 2-3'' apart, providing uniform pressure to the seal, and preventing the outer walls from warping.

Another change to the heat flux system would be to incorporate a reservoir and pump to allow clean water or some coolant to flow through the lines. The current setup using tap water will eventually destroy all the equipment. A pump and reservoir would circulate coolant in and out of the test section. The reservoir needs to be large enough to prevent the coolant temperature from rising unacceptably due to the recirculation of heated coolant.

The final recommendations for the existing setup covers the hardware used to regulate and measure the environment inside the FCR. The most significant change is adding a mass flow controller capable of regulating the burner airflow. The current setup using a flow meter, pneumatic valve, and control loop does not match the accuracy of the other equipment in the laboratory and fluctuations may affect test data at low flow rates. A larger volumetric calibration device should also be obtained to allow calibration of the airflow. The current bias error in the air flow rate is unknown. The propane flow was

calibrated but the precision of the mass flow control panel keeps the bias error at ± 0.05 SLPM. Currently, the random error in the propane mass flow rates is unknown because the actual mass flow rate of the propane is not collected. The MKS type 247 control panel has the capability to output the signal to LabVIEW®, but is not currently configured. This configuration should be accomplished before any more work is accomplished in the COAL laboratory.

5.3 Future Research

The end result of accomplishing each recommendation for modifying the existing FCR is a near total rebuild of the existing hardware. If all the hardware needs to be rebuilt, then a redesign should be considered at the same time. Any redesign should focus on correcting the flow velocity issue along the test section wall that hindered the first FCR. The redesign should also focus on simplifying and validating the design before any hardware is produced.

The new FCR design (Figure 72) has three sections: the burner section, the test section, and the nozzle section.

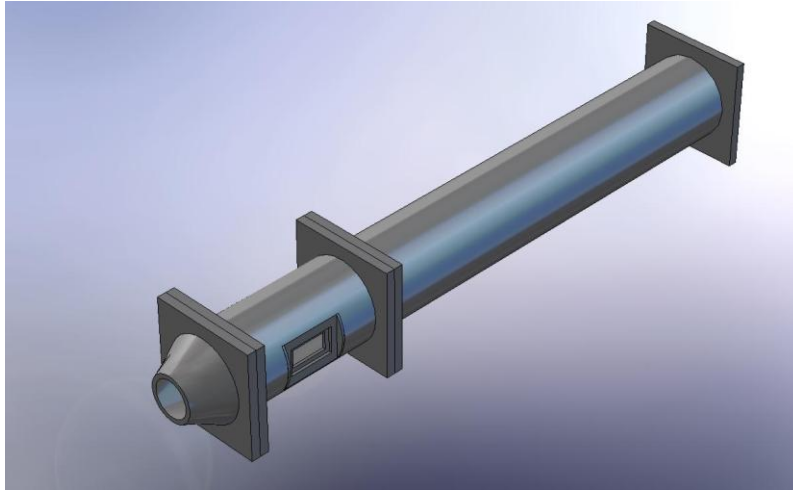


Figure 72: New FCR concept

The burner section is designed so the flame occupies a majority of the rig volume. No cooling is necessary as proven by the current design. Figure 73 shows a 2'' burner inlet for a 4'' cylindrical FCR body.

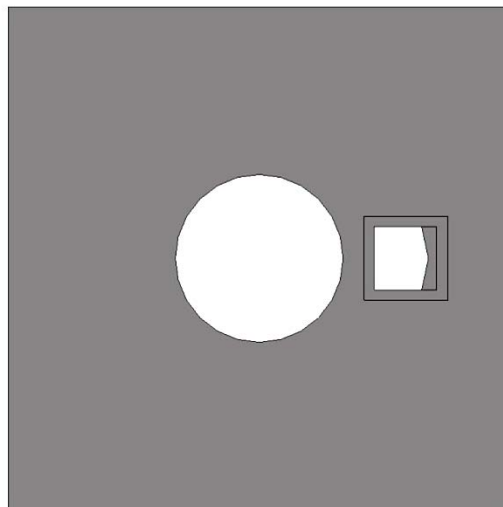


Figure 73: End view of new FCR burner

A custom glass window allows laser access from the test section wall out 3/4" in the radial direction. The burner section is long enough to allow complete combustion of the fuel/air mixture. A one-piece design using 4" schedule 40 pipe minimizes the cost, complexity, and number of seams where undesired air can enter. The square end caps are welded to the circular body, again preventing air from entering the body.

The test section (Figure 74) is modular, allowing different coolant hole configurations, but not different curvature radii.

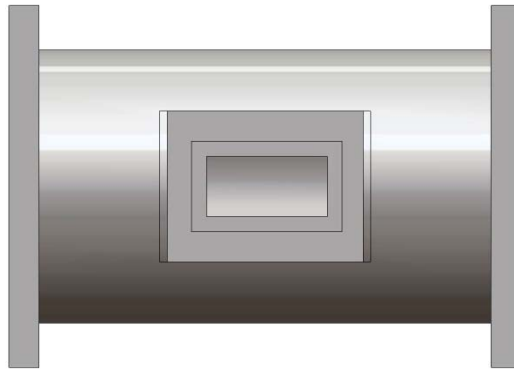


Figure 74: New test section concept

The simplicity of design makes up for this shortfall by allowing completely new FCR assemblies for a fraction of the cost and effort of the previous design. At each end of the test section is a mounting plate designed to attach the test section to the other sections, while preventing air from entering the body of the rig. A high temperature gasket should be in place between each section. The coolant hole is drilled directly into the single wall of the test section and coolant enters a plenum attached to the outside of

the test section (not shown). The observation window is directly opposite the cooling hole; its smaller size (2'' X 1'') minimizes the effect on the combustion product flow, although the section should be modeled using CFD to test for recirculation or separation near the coolant hole. The coolant hole should be drilled in a position to allow the coolant to enter on the upstream side of the window, at the center of the window for 0° injection and at the top of the window for compound injection. The test section need only be long enough to accommodate the cooling plenum and window.

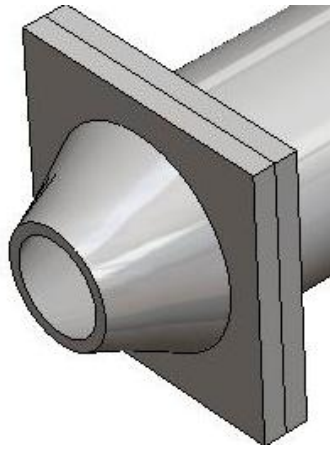


Figure 75: New nozzle concept

A nozzle section prevents room air from combusting with the fuel rich main flow. The converging nozzle design minimizes eddies in the air flow caused by the flat exit wall of the first FCR. The near constant velocity across the diameter of the FCR should not require much contraction to prevent upstream flow

The new FCR design is simpler and more effective than the current design. It allows collection of the infrared and laser diagnostics, although it does not allow collection of heat flux data.

Appendix A. MKS Type 247 Mass Flow Controller Control Panel Settings

The MKS Type 247D Four-Channel Readout instructions contain all the necessary information to setup and operate the panel(30). This appendix is included to show the settings used for the MFCs and gasses used by the FCR. The type 247 was operated using manual flow control, although the panel is capable of being controlled via LabVIEW®.

$$SCF = GF * GCF$$

where *SCF* is the *Scaling Control Factor*, *GF* is the *Gauge Factor*, and *GCF* is the *Gas Correction Factor*.

Table 6: MFC control panel settings

| MFC Size | Cal Gas | GF | Gas | GCF | SCF |
|----------|---------|-----|----------|-------|-----|
| 50 SLPM | N2 | 50 | C3H8 | 0.36 | 18 |
| 50 SLPM | air | 50 | zero air | 1.00 | 50 |
| 20 SLPM | N2 | 200 | C2H4 | 0.50 | 100 |
| 5 SLPM | H2 | 50 | C3H8 | 0.36 | 18 |
| 100 sccm | Xe | 100 | C3H8 | 0.27* | 27 |

*The GCF for the Xenon cal gas is 1.32, so the GCF for this MFC is $\frac{GCF_{C3H8}}{GCF_{Xe}} = \frac{0.36}{1.32}$.

For the other MFCs, the GCF of the cal gas is 1.0, so the GCF of the test gas is the GCF.

Appendix B. LabVIEW® Procedures

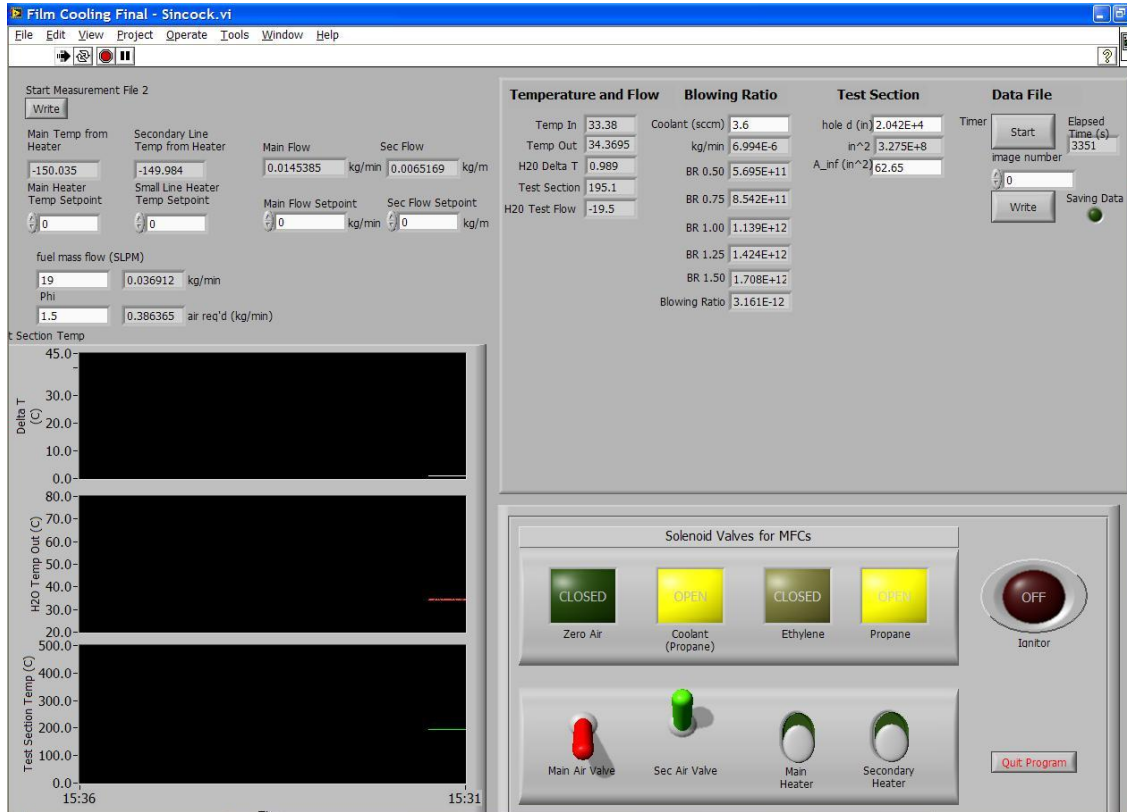


Figure 76: LabVIEW® VI for FCR

- Open *Film Cooling Final_1.VI* in the film cooling folder on the control computer desktop.
- Start the interface using the “run” button at the top of the program.
- Select the file location and name
- Set the *Fuel Mass Flow* to the max mass flow rate for the burner propane and Φ to 1.5. Observe the *air req'd* value for test conditions using the max fuel flow and $\phi=1.5$.
- Set the *hole diameter* and *test section area*.

- f. Open *Sec Air Valve*. Adjust the *Secondary Flow Setpoint* to the starting condition (0.25 kg/min). Confirm *Secondary Flow* has reached the setpoint and settled.
- g. After adjusting MFC panel settings to starting conditions, open *Zero Air, Coolant, Ethylene, and Propane Solenoid Valves*.
- h. After starting gas flow on MFC panel, press the igniter to start wait briefly and press again to stop the igniter. If the burner fails to start verify gas flows and settings then attempt again.
- i. Once the burner has started and the ethylene and zero air flow is shut off on the MFC, close the *Zero Air and Ethylene Solenoid Valves*.
- j. Increase the main burner Propane flow to 15 SLPM and then increase the *Sec Flow Setpoint* to 0.33 kg/m in 0.02 kg/m increments. Increase the main burner propane again to the max flow, and then increase the *Sec Flow Setpoint to the air req'd* value in 0.02 kg/min increments.
- k. Change the coolant flow rate on the MFC panel to the desired blowing ratio setting and input the value into the *Coolant* box. Observe the *Blowing Ratio* display at the desired value.
- l. After the water temperature has stopped increasing (less than 2°C increase over 10 minutes), start IR camera data collection and press the *Start Measurement File 2 Write* button.
- m. Adjust the *Phi* value to calculate new air flow settings as required. Input new air flow values into the *Sec Flow Setpoint box*. Allow to settle.

- n. Test blowing ratios (0.5, 0.75, 1.00, 1.25, and 1.50) are constantly displayed.
Change the MFC panel and update the *Coolant* box as required. Other blowing ratio settings must be hard coded into the program.
- o. When the test is complete, turn off gas flow on the MFC panel. Close the *Propane and Coolant Solenoid valves*. Burner air flow may be used to cool the FCR.
- p. When airflow is no longer required, change the *Sec Flow Setpoint* to 0.00 and close the *Sec Air Valve*.
- q. When all testing is complete, or when a new data file is desired, press the *Quit Program* button and close the program.

Appendix C. IR Camera Operation

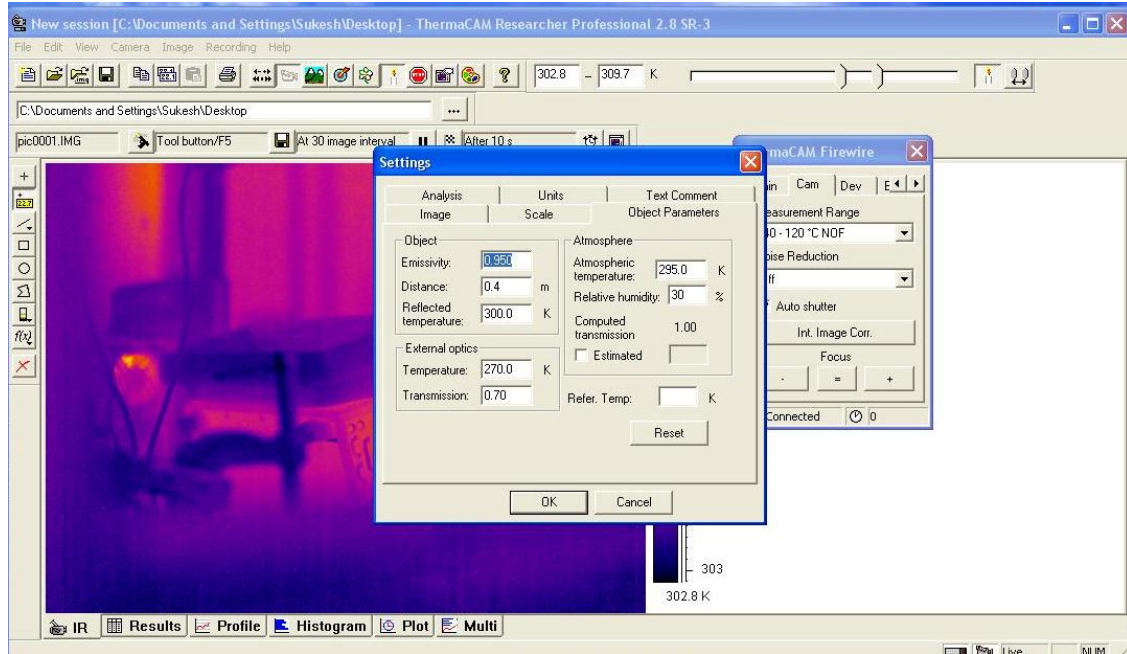


Figure 77: ThermoCam Researcher interface

This appendix is intended to describe the specific setting and procedures used to operate the IR camera for the FCR. More detailed information for the camera and software is given in the camera and software user manuals(31)(32).

- a. Place the camera opposite the FCR window and record the distance between the camera and the test section wall at the coolant hole. Ensure the ZnSe window is installed on the FCR.
- b. Connect the AC power cord and firewire cable to the camera. The firewire cable should be connected to the computer with the Thermacam Researcher software and the power cord to an AC power outlet.
- c. Turn the camera and computer on. Remove the lens cap.

- d. Start the Thermacam Researcher software. Connect to the camera by selecting *Camera* → *Connect*. View the camera image in the main window.
- e. If no image is observed press the *auto adjust scale* button. If no image is observed select the *Cam* tab in the Thermacam Firewire window. Verify the measurement range is set to (-40-120°C) or (0-500°C). If necessary troubleshoot further using the camera manual.
- f. Adjust the image focus in the Cam tab of the Thermacam Firewire window. Further refinement of the focus is possible using the focus ring on the camera.
- g. Remove camera while heating the FCR.
- h. Once the FCR has reached steady-state conditions, place the camera opposite the FCR.
- i. In the Cam tab of the Thermacam Firewire window change the measurement range to (300-2000°C).
- j. Select Image → Settings to bring up the camera settings. In the Object Parameter tab input the desired settings. The settings used for this research are shown below:

Table 7: ThermaCam Researcher settings

| <u>Object</u> | |
|-------------------------------|--------|
| emissivity | 0.95 |
| distance | 0.4 m |
| reflected temperature | 350 °K |
| <u>External Optics</u> | |

| | |
|--------------------------|--------|
| temperature | 350 °K |
| transmissivity | 0.70 |
| <u>Atmosphere</u> | |
| temperature | 350°K |
| humidity | 0.20 |

**These settings were used to get a rough absolute temperature. A thermocouple at the surface should be used to calibrate the temperature measurements.

- k. Select Recording→Conditions to set the test data collection parameters. Press the Image Directory button to set the image location. Create a new folder for each test. Set the recording parameters in the table below.

Table 8: Data collection settings

| | |
|----------------------|------------------------------|
| <i>Start</i> | <i>Tool Button/F5</i> |
| Record | At highest speed |
| Stop | After time duration (0,0,10) |
| External trig source | none |
| File Format | Images in multiple files |
| auto name base | set to test name |

- l. When ready to start data collection press F5 or the Start button.
- m. Output the image files to MATLAB® by selecting Recording→Copy Selection.
output directory: choose, Output name: same as source, Output format:
MATLAB.

The result of this operation is 300 MATLAB® files each with a 640 by 480 array of temperature data. The code in Appendix D processes the image files.

Appendix D. MATLAB® Code

```
% Curved Image Expansion Tool
%%%%%%%%%%%%%%%%%%%%%%%%%%%%%%%%%%%%%%%%%%%%%%%%%%%%%%%%%%%%%%%%%%%%%%%%
%%%
%       Created by Mike Miller - miller.462@wright.edu - (937)450-0488
%
%%%%%%%%%%%%%%%%%%%%%%%%%%%%%%%%%%%%%%%%%%%%%%%%%%%%%%%%%%%%%%%%%%%%%%%%
%%%
% This program opens multiple images saved as .mat files, averages the
% images together, "unfolds" the curved portion of the new image, and
% crops
% the new image to a user-defined size.
%
% The variable inputs are:
%   - The radius of the curve (r)
%   - The height of each pixel (h)
%   - The multiplication factor for the arc ratios (q)
%   - The coolant hole diameter (chd)
% The prompted user inputs are:
%   - The location of the bottom of the curved test section
%   - 2 corner points of the area to be cropped
%
% NOTE: When selecting the bottom of the test section, you MUST CLICK
% ABOVE
%       100 pixels from the bottom of the image for a 4-inch curve.
%%%%%%%%%%%%%%%%%%%%%%%%%%%%%%%%%%%%%%%%%%%%%%%%%%%%%%%%%%%%%%%%%%%%%%%%
%%%

%% Close & Clear all
close all
clear all
clc

%% Variable Inputs
%Radius of test section
r=4;
%The physical height(y-dimension) of each pixel (inches/pixel)
h=(1/95);
%q is the multiplication factor of the arcratios(higher q means the
%arcratio is more accurate)
q=10;
%Coolant hole diameter(inches)
chd=.07;
%% Open File
dir1=pwd;
[A,pathname]=uigetfile('*.mat','Select .mat Files to
Evaluate','MultiSelect','on');
cd(pathname);
list=strvcat(A); %#ok<VCAT>
[t,u]=size(list);
for i=1:t
    uiopen(list(i,:),1);
drawnow;
```

```

commandwindow;
%Find and Remove the file extension from the filename
n=length(list(1,:));
    for j=1:n
        X=uint8(list(i,j));
        periodlocation=0;
        if (X==46)
            periodlocation=j;
            break
        end
    end
m=periodlocation-1;
Alist=list(1:t,1:m);
end
%Create variable names for each matrix and put them in a column vector
B=0;B1=0;B2=0;B3=0;B4=0;B5=0;B6=0;B7=0;B8=0;B9=0;
B10=0;B11=0;B12=0;B13=0;B14=0;B15=0;B16=0;B17=0;B18=0;B19=0;
B20=0;B21=0;B22=0;B23=0;B24=0;B25=0;B26=0;B27=0;B28=0;B29=0;
B30=0;B31=0;B32=0;B33=0;B34=0;B35=0;B36=0;B37=0;B38=0;B39=0;
B40=0;B41=0;B42=0;B43=0;B44=0;B45=0;B46=0;B47=0;B48=0;B49=0;
B50=0;B51=0;B52=0;B53=0;B54=0;B55=0;B56=0;B57=0;B58=0;B59=0;
B60=0;B61=0;B62=0;B63=0;B64=0;B65=0;B66=0;B67=0;B68=0;B69=0;
B70=0;B71=0;B72=0;B73=0;B74=0;B75=0;B76=0;B77=0;B78=0;B79=0;
B80=0;B81=0;B82=0;B83=0;B84=0;B85=0;B86=0;B87=0;B88=0;B89=0;
B90=0;B91=0;B92=0;B93=0;B94=0;B95=0;B96=0;B97=0;B98=0;B99=0;
B100=0;
Blist=zeros(t,4);
    for i=1:t
        newB= genvarname('B',who);
        eval([newB ' = eval(Alist(i,:))']);
        Blist(i,:)=newB(:,:);
        Clist=char(Blist);
    end
%Concatenate all matrices into a 3D array and average them together
P=eval(Clist(1,:));
for i=2:t
    Pnew=cat(3,P,eval(Clist(i,:)));
    P=Pnew;
end
E=mean(P,3);
%Flip matrix E and create contour plot
C=flipud(E);
figure('Name','Average','NumberTitle','off');
contourf(C,'linestyle','none');
colormap(jet), colorbar;
%% User Input
disp('Click on the bottom of the test section');
[x,y]=ginput(1);
close
disp('Please Wait...');
%% Calculations
%Total pixels in y-direction for entire test section
ypixels=480-round(y);

```

```

%Calculate the arc length and arc ratio of each section
count=0;
D=[ypixels,1];
for i=0:ypixels-1
%The distance(inches) from the bottom of the curve to the bottom of the
current pixel
ybot=i*h;
%The distance(inches) from the bottom of the curve to the top of the
current pixel
ytop=ybot+h;
%"b" is the distance from the top of the curve to the bottom of the
current pixel
b=r-ybot;
%"a" is the distance from the top of the curve to the top of the
current pixel
a=r-ytop;
%x-dimension of the top of the pixel with respect to "a" and "r"
xtop=inline('sqrt((2*r*a)-(a^2))');
%x-dimension of the bottom of the pixel with respect to "b" and "r"
xbot=inline('sqrt((2*r*b)-(b^2))');
%x-dimension of the arclength
xarc=inline('xbot-xtop');
%Arc length of the pixel
arclength=inline('(pi*r*asin(sqrt(xarc^2+h^2)/(2*r)))/(pi/2)');
%Ratio of arclength to y-dimension of the pixel
arcratio=arclength(h,r,xarc(xbot(b,r),xtop(a,r)))/h;
arcratio10=round(q*arcratio);
count=count+arcratio10;
%Column vector of the arcratios of each pixel in the selected section
D(1+i,:)=arcratio10;
end
%% Build New Matrix
newrows=count+round(y)*q;
%Build the bottom section of the new matrix up to the input y-value
M=ones(newrows,640);
newcount=0;
j=1;
for i=1:round(y)
    qstart=newcount+1;
    for l=1:640
        M(qstart:newcount+q,l)=C(j,l);
    end
    j=j+1;
    newcount=newcount+q;
end
%Build the rest of the matrix using the adjusted values
newcount=round(y)*q;
p=0;
for i=round(y)+1:480
    p=p+1;
    k=D(p);
    kstart=newcount+1;
    for l=1:640

```

```

        M(kstart:newcount+k,1)=C(i,1);
    end
    newcount=newcount+k;
end
%PLOT THE ADJUSTED FIGURE
figure('Name','Adjusted Average','NumberTitle','off');
contourf(M,'linestyle','none');
colormap(jet), colorbar;
xlabel('Coolant Hole Diameters','fontsize',9,'fontweight','b');
ylabel('Coolant Hole Diameters','fontsize',9,'fontweight','b');
%SET FIGURE AXES TO HOLE DIAMETERS
%Coolant hole diameter in inches/(pixel height)
xdiam=chd/h;
xlimit=640/xdiam;
set(gca, 'XTick', 0:xdiam:640);
set(gca, 'XTickLabel', (0:1:xlimit),'fontsize',7);
ydiam=xdiam*q;
ylimit=newrows/ydiam;
set(gca, 'YTick', 0:ydiam:newrows);
set(gca, 'YTickLabel', (0:1:ylimit),'fontsize',7);
%% Crop Image
%Input corner points of area to be cropped
disp('Click on top left corner of crop area');
[x1,y2]=ginput(1);
disp('Click on bottom right corner of crop area');
[x2,y1]=ginput(1);
Y1=round(y1);
Y2=round(y2);
X1=round(x1);
X2=round(x2);
dx=X2-X1;
dy=Y2-Y1;
Mcrop=ones(dy,dx);
j=Y1;
for i=1:dy
    k=X1;
    for l=1:dx
        Mcrop(i,l)=M(j,k);
        k=k+1;
    end
    j=j+1;
end
%Plot the cropped image
figure('Name','Cropped Average','NumberTitle','off');
contourf(Mcrop,'linestyle','none');
colormap(jet), colorbar;
xlabel('Coolant Hole Diameters','fontsize',9,'fontweight','b');
ylabel('Coolant Hole Diameters','fontsize',9,'fontweight','b');
%SET FIGURE AXES TO HOLE DIAMETERS
%Coolant hole diameter in inches/(pixel height)
xdiam2=chd/h;
xlimit2=dx/xdiam2;
set(gca, 'XTick', 0:xdiam2:dx);

```

```

set(gca, 'XTickLabel', (0:1:xlimit2), 'fontsize', 7);
ydiam2=xdiam2*q;
ylimit2=dy/ydiam2;
set(gca, 'YTick', 0:ydiam2:dy);
set(gca, 'YTickLabel', (0:1:ylimit2), 'fontsize', 7);
%% Return to Original Directory
cd(dir1);
%% Re-Run Program?
restart=input('Press 1 to restart program, 2 to quit. ');
if restart==1
    CIET_multiple_images.m
else
    break
end

```

Bibliography

1. Holt, James B and Monk, Timothy S. Propellant mass Fraction Calculation Methodology For Launch Vehicles and Application to Ares Vehicles. Huntsville, AL : s.n.
2. McCall, Jonathan Floyd. *Discrete Film Cooling in a Rocket with Curved Walls*. ENY, Air Force Institute of Technology. 2009.
3. Humble, Ronald W., Henry, Gary N. and Larson, Wiley J. *Space Propulsion Analysis and Design*. First Edition-Revised. New York : The McGraw-Hill Companies, Inc., 1995. p. 524. ISBN 0-07-031320-2.
4. Wertz, James R. and Larson, Wiley J., [ed.]. *Space Mission Analysis and Design*. 3rd. Hawthorne : Microcosm Press, 2008.
5. Rutledge, James L. *Pulsed Film Cooling on a Turbine Edge Leading Edge*. Air Force Institute of Technology. 2009. Doctoral Dissertation.
6. Rannie, W. D. *A Simplified Theory of Porous Wall Cooling*. Jet Propulsion Laboratory, California Institute of Technology. 1947. ORDCIT Progress Report No. 4-50.
7. May, Lee and Burkehardt, W.M. *Transpiration Cooled Throat for Hydrogen Cooled Rocket Engines*. Aerojet Propulsion Division. Sacramento, CA : s.n., 1991. NASA Contract NAS 8-36952.
8. Chen, Fu-Jung. *Effects of Blowing Ratios on Heat Transfer to the Throat Region of a Porous-Walled Nozzle*. Air Force Institute of Technology. 1995. Masters Thesis.
9. Lenertz, Joseph L. *Effects of Blowing Ratio on Heat Transfer to the Throat Region of a Porous-Walled Nozzle*. Air Force Institute of Technology. 1994.
10. Landis, Jay A. *Numerical Study of a Transpiration Cooled Rocket Nozzle*. Air Force Institute of Technology. 1995. Masters Thesis.
11. Huzel, Dieter K and Huang, David H. *Modern Engineering for Design of Liquid-Propellant Rocket Engines*. 3rd. Washington D.C. : The American Institute of Aeronautics and Astronautics, Inc., 1992. p. 101.

12. Spalding, D. B. *Convective Mass Transfer*. New York : McGraw-Hill Book Company, Inc, 1963. p. 38.
13. *The Turbulent Boundary Layer on a Porous Plate: Experimental Skin Friction With Variable Injection and Suction*. Simpson, Roger L., Moffat, R. J. and Kays, W. M. London : s.n., 1969, International Journal of Heat and Mass Transfer, Vol. 12, pp. 771-789.
14. Kays, W. M. and Crawford, M. E. *Convective Heat and Mass Transfer*. New York : McGraw-Hill Book Company, 1980.
15. Hartnett, James P. and Irvine, Thomas F., [ed.]. *Advances in Heat Transfer*. New York : Academic Press, 1965. Vol. 2.
16. Keener, David N. *Investigation of Boundary Layer and Performance Effects of Transpiration Cooling Through a Porous Plate in a Rocket Nozzle*. Air Force Institute of Technology. 1994. Masters Thesis.
17. Anderson, Wesly S. *Design, Construction, and Validation of the AFIT Small-Scale Combustion Facility and Sectional Model of the Ultra-Compact Combustor*. AFIT. 2007. Masters Thesis.
18. Koether, Stephen J. *Validation of the AFIT Small-Scale Combustion Facility and OH Laser-Induced Florescence of an Atmospheric Laminar Premixed Flame*. AFIT. 2007. Masters Thesis.
19. Hankins, Terry B. *Laser Diagnostic System Validation and Ultra-Compact Combustor Characterization*. AFIT. 2008. Masters Thesis.
20. Lakusta, Patrick J. *Laser-Induced Fluorescence and Performance Analysis of the Ultra-Compact Combustor*. AFIT. 2008. Masters Thesis.
21. Drenth, Aaron C. *Laser-Induced Fluorescence and Synthetic Jet Fuel Analysis in the Ultra Compact Combustor*. AFIT. 2009. Masters Thesis.
22. Thomas, Levi M. *Flow Measurements Using Particle Image Velocimetry in the Ultra Compact Combustor*. AFIT. 2009. Masters Thesis.
23. Bohnert, Alex M. *Thermal Characterization of a Hall Effect Thruster*. AFIT. 2008. Masters Thesis.

24. Kim, Ted T. *Thermo-Mechanical Characterization of Silicon Carbide-Silicon Carbide Composites at Elevated Temperatures Using a Unique Combustion Facility*. AFIT. 2009. Doctoral Dissertation.
25. Dittman, Eric R. *Design, Build, and Construction of a Small Scale Combustion Chamber Testing Facility*. AFIT. 2006. Masters Thesis.
26. Turns, Stephen R. *An Introduction to Combustion*. 2nd. Boston : McGraw Hill, 2000.
27. Sutton, George P. and Biblarz, Oscar. *Rocket Propulsion Elements*. New York : John Wiley and Sons, Inc., 2001.
28. General Thermocouple Specifications. *Omega.com*. [Online] Omega. [Cited: 02 15, 2010.]
http://www.omega.com/toc_asp/frameset.html?book=Temperature&file=TC_GEN_SPECS_REF.
29. FLIR P640 Infrared Camera Datasheet. Portland, OR : FLIR Systems Co. LTD.
30. Approximate Temperature of Steel by Color. *Muggy Weld*. [Online] [Cited: January 29, 2010.] <http://www.muggyweld.com/color.html>.
31. MKS Type 247D Four-Channel Readout User Manual. Andover, MA : MKS Instruments, 07 1997. Rev A.
32. ThermaCAM Researcher User's Manual. s.l. : FLIR Systems, 2006.
33. FLIR 600 Series User's Manual. s.l. : FLIR Systems, 2009.
34. Von Karman, Theodore and Edson, Lee. *The Wind and Beyond*. Boston : Little, Brown, and Company, 1967. .

Vita

Major Sincock is a 1999 graduate of the United States Air Force Academy where he studied Engineering Mechanics. His first assignment was to Malmstrom AFB, Montana, where he was an operational ICBM crew commander and instructor. Major Sincock was a member of the best ICBM operations team in Air Force Space Command during the 2002 Guardian Challenge competition.

As an Air Force engineer, Major Sincock led the ground station development for the Space Radar Integrated Program Office, working closely with the National Reconnaissance Office and the National Geo-spatial Intelligence Agency. He was then selected to join the Navy Mobile User Object System Program Office (PMW-146) as the lead for EELV launch integration. During this time he worked closely with the Air Force EELV team, the Navy, and the satellite and launch vehicle contractors to coordinate the first ever launch of a major Navy satellite using an Air Force launch vehicle.

After graduation in March 2010, Major Sincock reports to the Space and Missile Propulsion Division of the Air Force Research Laboratory at Edwards AFB, California, continuing his career-long focus on space and missile operations and development for the Air Force.

| REPORT DOCUMENTATION PAGE | | | | Form Approved OMB No. 074-0188 | |
|--|-------------|-----------------------------------|--|---|--|
| <p>The public reporting burden for this collection of information is estimated to average 1 hour per response, including the time for reviewing instructions, searching existing data sources, gathering and maintaining the data needed, and completing and reviewing the collection of information. Send comments regarding this burden estimate or any other aspect of the collection of information, including suggestions for reducing this burden to Department of Defense, Washington Headquarters Services, Directorate for Information Operations and Reports (0704-0188), 1215 Jefferson Davis Highway, Suite 1204, Arlington, VA 22202-4302. Respondents should be aware that notwithstanding any other provision of law, no person shall be subject to a penalty for failing to comply with a collection of information if it does not display a currently valid OMB control number.</p> <p>PLEASE DO NOT RETURN YOUR FORM TO THE ABOVE ADDRESS.</p> | | | | | |
| 1. REPORT DATE (DD-MM-YYYY) 25-03-2010 | | 2. REPORT TYPE Master's Thesis | | 3. DATES COVERED (From – To) Sep 2008 – Mar 2010 | |
| 4. TITLE AND SUBTITLE Design Of A Film Cooling Experiment For Rocket Engines | | | 5a. CONTRACT NUMBER | | |
| | | | 5b. GRANT NUMBER | | |
| | | | 5c. PROGRAM ELEMENT NUMBER | | |
| 6. AUTHOR(S) Sincock, Andrew, L., Major, USAF | | | 5d. PROJECT NUMBER | | |
| | | | 5e. TASK NUMBER | | |
| | | | 5f. WORK UNIT NUMBER | | |
| 7. PERFORMING ORGANIZATION NAMES(S) AND ADDRESS(S) Air Force Institute of Technology Graduate School of Engineering and Management (AFIT/ENY) 2950 Hobson Way, Building 640 WPAFB OH 45433-8865 | | | 8. PERFORMING ORGANIZATION REPORT NUMBER AFIT/GAE/ENY/10-M23 | | |
| 9. SPONSORING/MONITORING AGENCY NAME(S) AND ADDRESS(ES) Michael Huggins Air Force Research Laboratory Propulsion Directorate 4 Draco Drive Edwards AFB, CA 93524 | | | 10. SPONSOR/MONITOR'S ACRONYM(S) AFRL | | |
| | | | 11. SPONSOR/MONITOR'S REPORT NUMBER(S) | | |
| 12. DISTRIBUTION/AVAILABILITY STATEMENT APPROVED FOR PUBLIC RELEASE; DISTRIBUTION UNLIMITED. | | | | | |
| 13. SUPPLEMENTARY NOTES | | | | | |
| 14. ABSTRACT <p>The Film Cooling Rig (FCR) is a new test rig at the Air Force Institute of Technology (AFIT) to study film cooling for rocket engine applications. The original researcher designed, built, and then utilized the FCR to study radial curvature effects on film cooling for a non-combustion environment. This effort modified the FCR by adding propane-air combustion. Modular stainless steel test sections were produced to allow study of various curvatures and coolant injection angles. A pre-mixed burner was designed and built to deliver main flow mass flow rates necessary to produce blowing ratios as low as 0.5. A water cooling system was designed for the entire FCR, but only implemented for the curved test sections. Instrumentation in this system allows calculation of the average heat flux to the test section. Once the necessary FCR and lab modifications were accomplished, the operating range of the FCR was developed and tested using infrared thermography. Surface temperature measurements near the cooling hole showed no cooling effect for 13 major test configurations, and many more minor variations. The lack of cooling was caused by inadequate spreading of the burner flow to the test section wall. Without the necessary main flow momentum across the test section wall, the coolant flow did not turn and adhere to the wall. Instead, it jetted into the main flow without cooling the wall as expected. Recommendations included modifications to the existing rig to correct the main flow issue, along with a completely new FCR design incorporating the lessons learned from this research to produce a simpler, more effective rig. The new design allows the laser and infrared diagnostics of the first rig without the manufacturing complications that hindered testing in the first FCR.</p> | | | | | |
| 15. SUBJECT TERMS Combustion, Rocket, Film, Cooling, Transpiration, Infrared | | | | | |
| 16. SECURITY CLASSIFICATION OF: | | | 17. LIMITATION OF ABSTRACT | 18. NUMBER OF PAGES | 19a. NAME OF RESPONSIBLE PERSON |
| a. REPORT | b. ABSTRACT | c. THIS PAGE | | | Richard Branam, Lt Col, USAF |
| U | U | U | UU | 154 | 19b. TELEPHONE NUMBER (Include area code) (937)255-6565, ext 6485 |